Advances in Hollow Core Fibres and Application to Mid-Infrared Fibre Gas Lasers

Xu, Mengrong

Award date:
2018

Awarding institution:
University of Bath

Advances in Hollow Core Fibres and Application to Mid-Infrared Fibre Gas Lasers

submitted by

Mengrong Xu

for the degree of Doctor of Philosophy

of the

University of Bath

Department of Physics

December 2017

Abstract

Anti-resonant hollow core fibre is a new kind of optical fibre waveguide in which light is trapped in a hollow core surrounded by the capillary formed microstructured cladding. This fibre exhibits high damage threshold, low dispersion and ultra-low nonlinearity with relatively low loss of a few tens of dB/km. Its intrinsic feature of multimode delivery limits the applications with high requirements of single mode transmission.

In my thesis, I demonstrate how the design of hollow core fibre can be improved with single mode guidance. S^2 imaging measurement was used to analyse the mode content of the solid core fibres. In my research, I established S^2 measurement to measure the mode contents in hollow core fibres for the first time. Two hollow core fibres with 8 capillaries and 7 capillaries in their claddings were fabricated in same fashion and showed differences in low attenuations. By comparing the mode contents in both of the fibres via S^2 imaging measurement, 7-capillary HCF was demonstrated to give better performance on single mode guidance.

Among the applications of the HCF, the property of delivering high power in HCF makes the gas filled HCF laser possible. In my research, a continuous-wave mid-infrared acetylene filled hollow core laser was built with a slope efficiency of 33% and an output power of over 1 watt at the wavelength region of 3.1~3.2 μm. The pump source is an Erbium-doped fibre amplified tunable laser diode which works at C-band wavelength. The fibre without the gain medium has two transmission bands with low attenuation of 0.037 dB/m and 0.063 dB/m at pumping and lasing wavelengths respectively. This laser system works in either cavity-based configuration or single pass ASE configuration. The latter configuration shows a better performance in high output power and high slope efficiency. The optimized laser system was studied experimentally with the proper fibre length and gas pressure. This laser system could be extended to be filled with other molecules to longer wavelengths and has potential for high power output.

Acknowledgement

First and foremost, I would like to express my deep sense of gratitude to my parents for encouraging and supporting me in the pursuit of my dream. I hope you are proud of what I have achieved with your support.

It has been a great honour to be part of the Centre for Photonics and Photonic Materials (CPPM) and to work with such professional, friendly and dynamic colleagues. I am extremely grateful to my supervisor, Jonathan Knight. Your incredible scientific perception and patient teaching always inspires me. Dr. Fei Yu, who I shall say thanks to a thousand times, helped me hugely in all aspects of my PhD life.

William and Tim: you are amazing in that you know everything and have always been able to solve my problems immediately. Thanks for your generous help! Also, I would like to thank to my past and present colleagues in CPPM: Kerri, Harry, Maria, Stephonos, Clarissa, Rosdi, Jamie and Rowan. I am so delighted to have shared an office with you and very much appreciate your help with my English writing and with my research.

I have had great fortune to live with my dearest housemates: Qian Yang, Zichen Liu, He Huang, Lu Tong and Yang Liu. I will always remember the days we shared our happiness and how we encouraged each other. The highlight of my free time has been to spend every Friday evening at ‘Friday werewolf board game night’ with Da Chen, Hui Tang, Yadong Li, Yang Yao, Chen Qian, ‘No.11’, and many other friends in Bath.

My thanks also need to go to LuHan and Beibei, my favourite singers. Your songs light up my life and revive me every day.

Finally, thanks to Mr Wang, my boyfriend. I truly appreciate your understanding, support, trust and cherish in our long distance love. You are my lobster today and all of tomorrows.

List of publication

Journals:

1. **Mengrong Xu**, Fei Yu, M. R. A. Hassan and Jonathan C. Knight, "Continuous-Wave Mid-Infrared Gas Fiber Lasers," *IEEE Journal of Selected Topics in Quantum Electronics* 24, 3, 1-8 (2018)

2. **Mengrong Xu**, Fei Yu, and Jonathan Knight, "Mid-infrared 1 W hollow-core fiber gas laser source," *Opt. Lett*. 42, 4055-4058 (2017)

3. Fei Yu, **Mengrong Xu**, and Jonathan C. Knight, "Experimental study of low-loss single-mode performance in anti-resonant hollow-core fibers," *Opt. Express* 24, 12969-12975 (2016)

Conferences:

1. **Mengrong Xu**, Fei Yu, and Jonathan Knight, "Low-Loss Anti-Resonant Hollow-Core Fibers with Single-Mode Performance," in *Advanced Photonics 2016 (IPR, NOMA, Sensors, Networks, SPPCom, SOF)*, OSA Technical Digest (online) (Optical Society of America, 2016), paper SoM3F.5.

2. **Mengrong Xu**, Fei Yu, Muhammad Rosdi Abu Hassan, and Jonathan C. Knight, "Continuous-Wave 3.1 μm Gas Fiber Laser with 0.47 W Output Power," in *Conference on Lasers and Electro-Optics*, OSA Technical Digest (online) (Optical Society of America, 2017), paper SF2K.4.

3. William J. Wadsworth, Adrian L. Love, Fei Yu, Muhammad Rosdi Abu Hassan, **Mengrong Xu**, and Jonathan C. Knight, "Gas filled hollow core mid-IR fibre lasers," in *2017 European Conference on Lasers and Electro-Optics and European Quantum Electronics Conference*, (Optical Society of America, 2017), paper CJ_8_1.

Contents

CHAPTER 1 INTRODUCTION

1.1 Hollow core fibres

1.1.1 Overviews of hollow core fibres

In 1966, C. K. Kao, who was awarded the Nobel Prize in Physics in 2009, theoretically proved that optical fibres could be a new medium for long distance telecommunication if the loss was as low as 20 dB/km [1]. In this paper, a fibre of glassy material, with the core of higher refractive index, operated in a single mode, even though the fibre transmission and bending loss was high. In the 1970s, with the improvement of fabrication and measurement techniques [2], a very low loss single-mode fibre with a minimum loss of 0.20 dB/km at a wavelength of 1.55 μm was attained [3]. Since then, optical fibres have witnessed an explosive growth.

In fact, the history of the optical fibres can be dated back to the first discovery of total internal reflection (TIR) by Tyndall in 1870 [4]. This guiding principle made fibre optics possible. Modern optical fibres appeared later, and use TIR by having a silica core surrounded by a cladding with a lower refractive index [5]. The theory is easy to implement as fabrication techniques have improved rapidly. Optical fibres are not only investigated in the lab research but also commercialised and applied to the industry in the aspect of the long distance telecommunication, lasers and sensing [6-9].

However, a new class of optical fibres with a variety of microstructures have been developed over the last twenty years, which offer advantages over the very successful conventional fibre designs. This kind of fibre is no longer based on the TIR because the microstructured core is vacuumed or filled with air or other gases. These core materials will have a lower refractive index than the cladding solid material.

The first hollow waveguide was traced back to 1936, when a straight hollow conducting cylinder of circular cross-section was studied in theory in *Bell Telephone Laboratories*. They found the metal waveguide provided lower attenuation with an increase in frequency [10]. To meet the increasing demand of radar systems, a transmission medium for the millimetre wave system was demonstrated as a waveguide with a circular cross-section that had an inside diameter of 60 mm in 1977. Outside the hollow core was steel tube with absorbing materials attached on the inner surface. This combination of waveguide types provide a total loss below 1 dB/km from 40-100 GHz [11].

The first dielectric hollow core waveguide was theoretically studied at the optical frequency by Marcatili and Schmeltzer in 1964 [12]. In this paper, the field configuration, the propagation constants of the normal modes and the attenuation due to curvature of the axis were determined for a hollow circular waveguide made of dielectric material or metal for application as an optical waveguide. They also predicted that the hollow metallic circular waveguide appeared to be very attractive as a transmission medium for long distance optical communication. The telecommunication limit for the dielectric hollow core waveguide is due to the trade-off between the transmission loss and the bending loss.

Later in 1974, single- and multi- mode optical waveguide were fabricated solely from pure fused silica with the transmission loss of 3 dB/km at 1.1 μm [13]. Due to the challenges of fabrication techniques, especially on a scale of micrometres, the dielectric hollow core waveguide had slow progress.

As for optical wavelengths, the metal hollow core fibre was first fabricated in 1980 [14]. From then on, hollow core waveguides made from glass and metal were developed rapidly [15]. Hollow core waveguide designed for CO_2 laser transmission at a wavelength of 10.6 μm was first fabricated with sapphire in 1990 [16]. Later in 1992, a Ge-coated Ag hollow core waveguide achieved 2.6 kW output power for CO_2 laser delivery [17].

The metal hollow core waveguides have better performances for transmission at microwave and far infrared wavelengths than the dielectric hollow core waveguides. This is because the dielectric materials usually have extremely high

absorption at longer wavelengths. However, at shorter wavelength such as optical wavelengths, the dielectric materials exhibit great transparency. Since the mechanisms of confining the light in hollow waveguides is not same as the TIR, the leaky loss happens all the time leading to a fundamentally higher loss than the solid core waveguide.

In the 1980s, another guiding mechanism, Photonic Bandgap (PBG) effect, was demonstrated in 1987 when it was proposed that light can be trapped in the photonic bandgap within photonic crystals [18, 19]. The dielectric hollow core waveguide, named as hollow core Photonic Bandgap Fibres (HC-PBFs), which consisted of pure silica core surrounded by a silica-air photonic crystal material, were first reported in 1996 [20, 21]. Since then, a variety of fibres with different microstructures have appeared.

In 2002 a new type of optical fibres with a 'Kagome' lattice cladding was reported by Benabid [22]. Light was guided over a broad wavelength range in discrete transmission bands while there was no photonic band gap found either experimentally or through simulations. Thus, the loss was higher than in conventional step index fibres or in photonic bandgap fibres. The advances of the fabrication technique have triggered spectacular progress in their transmission performance, bringing the attenuation down from ~ 1 dB/m [22] to ~ 1 dB/km [23] within only three years. However, drawbacks such as narrow transmission bandwidth and the overlap between the fundamental mode and interface modes limits a large number of applications like broadband light sources. The advent of the large-pitch Kagome-structure hollow core fibre and a square-lattice hollow core fibre further decreased the attenuation and broad the transmission bandwidth [24, 25].

A low loss Kagome fibre with negative curvature of the core boundaries was first reported in 2010 [26]. A series of experiments confirmed the importance of the curvature in reduction of the Kagome fibre attenuation [27]. In Vincetti and Setti's paper, numerical simulations predicted that the high loss transmission regions in the Kagome hollow core fibre were caused by the coupling between the core mode and cladding modes [28]. A simplified Kagome-lattice fibre reduced to one layer of air

holes was proved a new route to obtain low loss fibres [29]. Since then, new designs of cladding microstructures have become popular [30].

The mid-infrared (mid-IR) spectral region of 2~20 μm contains strong vibrational transitions of many important molecules and two atmospheric transmission windows of 3~5 μm and 8~13 μm, which is crucial in silica fibre transmission and draws much attention. In 2011, hollow core negative curvature fibres (HC-NCF or simply NCF) with only one row of silica capillaries, which allowed light guidance from near to mid-IR region despite of the high loss of silica material, was first reported [31] (shown in Fig. 1-1 (a)). Later on the transmission window was extended to a longer wavelength of 10.6 μm for the CO_2 laser delivery in a similar shape HC-NCF made of chalcogenide glass instead of silica [32]. Until now, the minimum attenuation in mid-IR region of the hollow core negative curvature fibre (shown in Fig. 1-1 (b)) was reported as low as 24.4 dB/km at a wavelength of 2.4 μm [33].

Low loss NC-HCFs were also demonstrated for shorter wavelength transmission in the visible and near-infrared region. A NCF with attenuation of 0.15 dB/m and 0.18 dB/m at 532 nm and 515 nm achieved single mode nanosecond and picosecond pulses at 1064nm respectively [34]. An fibre attenuation of 40 dB/km was measured at 1064 nm in NCF which acted as a part of ring cavity in a mode-locked fibre laser [35]. At mid-infrared wavelength of 3050 nm, NCF had an attenuation of 34 dB/km [36]. Another NCF designed and fabricated by myself for acetylene filled fibre laser has a low attenuation of 68 dB/km at 3.1 μm and 37 dB/km at 1.53 μm in these two specific transmission bands.

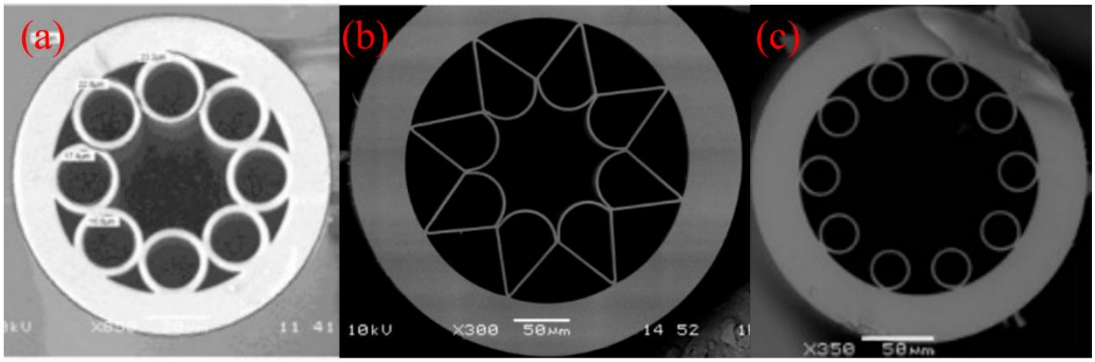

Fig. 1-1 Cross sections of Hollow core negative curvature fibres (a) First HCF designed and fabricated by [31] (b) Ice-cream shaped HCF[33] (c) Open boundary NCF [37].

Another design of NCF with open boundary capillary cladding was reported to be able to achieve low loss in mid-infrared spectrum range from 2.5 μm to 7.9 μm in 2013 [37]. Bending loss can be greatly reduced in a similar NCF reported by Belardi in 2014 [38] (shown in Fig. 1-1 (c)). Further simulations of the design by adding extra anti-resonant elements in the cladding predicted that the leaky and bending loss can be further decreased [39-41] . Different shapes of elements are built into the cladding rings such as positive and negative curvatures which decreases the attenuation dramatically [42]. Simulations also proved the loss performance and higher-order mode suppression is significantly improved by using symmetrically distributed anisotropic anti-resonant tubes in the cladding, elongated in the radial direction, when compared to using isotropic, i.e. circular, anti-resonant tubes [43]. However, these HCFs with low loss are difficult to draw with the current fabrication techniques.

1.1.2 Guiding mechanism

The anti-resonant hollow core fibre is intrinsically leaky as the light cannot be totally reflected inside the core with low refractive index. The guiding mechanism for hollow core waveguides originated from Marcatili and Schmeltzer's theory [12]. Later, the 'ARROW' model was proposed to systematically explain how the light is confined and transmitted in the fibre [120].

1) Marcatili and Schmeltzer's theory

In Marcatili and Schmeltzer's paper, they presented an analysis of the field configuration and propagation constants of the modes in the hollow core waveguide for the first time. They assumed the core was circular due to its simplicity and low loss. Both metallic and dielectric guides were discussed. The metallic waveguide is more suitable for microwave frequency rather than the optical wavelengths, as the metal is not a good conductor for this range. With a large dielectric constant, the dielectric materials such as glass is good at transmitting in the optical wavelengths. However, they revealed that the dielectric circular waveguide was not a promising contender for long distance transmission of light.

In their work, they considered the waveguide consisting of a circular cylinder of radius a. The cylinder was infinite and uniform with a higher refractive index than the hollow core. They derived the formulas for the mode attenuation and the corresponding propagation constant after some mathematical approximations.

In a dielectric waveguide, the expressions are as follows [12]:

$$\alpha = \left(\frac{u_{nm}}{2\pi}\right)^2 \frac{\lambda^2}{a^3} \begin{cases} \frac{1}{\sqrt{n^2-1}}\ ,\ TE_{0m}\ modes\ (n=0) \\ \frac{n^2}{\sqrt{n^2-1}}\ ,\ TM_{0m}\ modes\ (n=0) \\ \frac{\frac{1}{2}(n^2+1)}{\sqrt{n^2-1}}\ ,\ EH_{nm}\ modes\ (n\neq 0) \end{cases} \quad \text{Equ. 1-1}$$

$$\beta_{nm} = \frac{2\pi}{\lambda}\left\{1 - \frac{1}{2}\left(\frac{u_{nm}\lambda}{2\pi a}\right)^2\right\} \quad \text{Equ. 1-2}$$

In the expressions, *n* stands for the refractive index and u_{nm} is the m^{th} root of Bessel function $J_{n-1}=0$. The attenuation α are proportional to $\frac{\lambda^2}{a^3}$. It implies the attenuation can be suppressed by choosing the core radius relatively larger than the wavelength λ. Additionally, different modes affect the attenuation in different types of loss. The fundamental mode in a relatively large core has a lowest attenuation from this formula. However, the attenuation constants were calculated for a straight waveguide only. Bending loss was predicted to be considerably high with a large core. This theory can only be applied in a simple circular model. In terms of the complex structures in the HCF cladding, multiple reflections affect the attenuation of the leaky modes in the core by the interference between boundaries of different materials.

Thus this theory provides a method to calculate the mode loss of the hollow core waveguide with a limitation in a more complex and bending HCF.

2) Anti-resonance reflecting optical waveguide model

The anti-resonance reflecting optical waveguide (ARROW) model was first proposed in 1986 to explain how a layer of poly-Si with higher refractive index confined light waves in SiO_2 with lower refractive index [121]. Later in 2002, this concept is applied to low-index core photonic bandgap optical waveguides [120]. The

thickness of the high refractive index layers and the refractive index contrast were found to determine the transmitted wavelengths and the attenuation [120]. Soon it became the most widely used model to explain the microstructured hollow core fibres.

Typically, the photonic bandgap fibres rely on the guidance mechanism of TIR or PBG guidance. The former is similar to the step index fibre; the latter one guides light in a low-index core through Bragg reflections off high- and low-index periodic layers in the cladding. However, if the lattice constant of the photonic bandgap waveguide is larger than the transmitted wavelength and the refractive index contrast is high, the spectral characteristic is mainly governed by the first layer of the high refractive index cladding.

This anti-resonance behaviour is explained as follows: the higher index cladding structure acts as a waveguide, in which certain cladding modes with specific wavelengths can be supported. At these wavelengths, the number of modes, *n*, supported in the cladding switches from *n+1* to *n* [122], which means the minima transmission occurs here. It is reasonable that the lower index core modes couple with the higher index cladding modes allowing light to escape from the core to create resonance. Between these resonances, the anti-resonances cannot be coupled to the cladding and instead reflects back into the core.

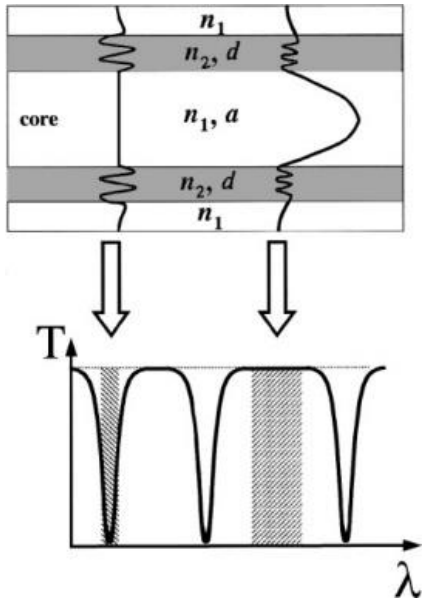

Fig. 1-2 Schematic of (top) the ARROW structure and (bottom) its transmission spectrum [120].

To make it more clear and intuitive, a 2D model is shown in Fig. 1-2. The fibre microstructure consists of an array of rings with thickness *d*. The rings have a refractive index n_2 higher than air index n_1 in hollow core. Each layer in the cladding is considered as a Fabry-Perot resonator which transmit certain wavelengths and reflect the light at the anti-resonant wavelengths back into the lower index core. Mathematically, the resonances are given by the condition [120]

$$\lambda_m = \frac{2n_1 d}{m}\sqrt{n_2^2 - n_1^2} \qquad \text{Equ. 1-3}$$

in which *m* is a positive integer, representing the order of resonance. The high loss occurs at the wavelengths of λ_m.

At the resonant wavelengths, large attenuation of the core mode can leak through the high index layer. On the other hand, at the anti-resonance wavelengths, the reflectivity of the high index layer increases and the light is confined in the low index core. Therefore, the transmission spectrum is multiband as Fig. 1-2.

From this ARROW model, the resonance bands are simply calculated with the thickness and refractive index of the higher index layer. However, the model is not perfect because other important parameters of the HCF are still unknown such as the mode attenuations.

3) Leaky mode coupling

The leaky mode coupling model is another approach to discuss how the core modes leak out by coupling into the dielectric in the hollow core waveguide. The guidance mechanism is inhibited coupling between the modes that propagate in the core and modes that propagate in the dielectric, in the cladding tubes or in the interstices between two cladding tubes [30]. In 2010, Vicetti and Setti demonstrated a useful and numerically valid model to describe the coupling between air and dielectric modes in a single tube waveguide [28].

In their simulations by finite element method, they first investigated the mode property in a tube waveguide made of dielectric material with higher refractive index. The material inside and outside of the tube is air with refractive index of 1. Two

different kinds of confined modes are presented: the ‘airy’ modes are in the air core with an effective index lower than 1; the ‘dielectric’ modes are mainly located inside the dielectric. The leaky ‘airy’ modes are coupled into the ‘dielectric’ modes and causes anti-crossing and high leakage loss when the ‘dielectric’ modes are at their cut-off frequency, which is similar to the phenomenon observed in hollow core PBG fibres between core and surface modes [123]. The cut-off frequency mainly depends on the ratio between inner and outer tube diameters, i.e. the wall thickness. Effective index of the ‘airy’ modes is another parameter of importance. It is explained with the so called mode matching method [124], that the coupling happens when the ‘airy’ mode index is similar to the dielectric mode index. Thus the model in the single tube waveguide is able to simply predict the dispersion and the loss properties by designing the tube thickness, diameter and refractive index.

To investigate a fibre closer to a real case with complex design, the model is applied to a fibre with several tubes surrounding the core. The core geometrical parameters and the number of the tubes in the cladding are optimized for low attenuations. This resulted in showing that fibres with 7 tubes arranged in the cladding exhibit a tradeoff between high order modes loss and low fundamental mode loss.

During the period of my research, we first got the results and published papers on single mode performance in 7 capillary HCF in 2016 [50, 51]. Soon later, similar results were reported from other groups.

A recent systematic study on the mode coupling between core modes and cladding modes was proposed by Chengli Wei et al. in 2017 [30], in which negative curvature is found to be the key component to decrease the transmission attenuations the same as in Kagome fibre [125]. In the transmission band, the coupling should be inhibited. By having a small mode overlap and a mismatch of their effective indices, the coupling between the core and the cladding is reduced. The cladding wall thickness decides the transmission wavelengths and the effective indices in the core and the cladding. The gap between two neighbour tubes in the cladding also affects the leakage loss. It means the mode intensity inside the gap increases when the gap increases. But the increased leakage through the gap leads to an increased leakage

loss from a certain gap distance value. In other words, the gap changes as well as the cladding tube diameter. Different numbers of the tube in the cladding are also considered. When core mode area is similar to the tube area, the effective indices are similar. In this case, the coupling is much easier. This paves a way for single mode transmission performance in 7 capillary HCFs in the next chapter.

1.1.3 Mode properties of hollow core fibres

Hollow core fibres are different from common solid optical fibres because hollow core fibres intrinsically transmit all spatial modes but with different attenuations. High order modes have higher attenuations than the fundamental mode and are easily eliminated during long distance transmission. In short length transmissions of laser powers, hollow core fibres usually suffer from poor beam quality because higher modes cannot dissipate clearly. As a result, it is vital to achieve low loss single mode guidance for applying hollow core fibres for delivery of powerful short pulses for industrial and other applications.

Previous investigations of single-mode guidance of hollow-core fibres have included the theoretical study and numerical simulations of photonic bandgap hollow-core fibre [44]. The coupling between higher-order modes of the core and fundamental modes of ancillary shunt cores embedded in the cladding is optimized by phase matching [45].

In terms of the HCFs, single mode properties were numerically achieved by tuning the thickness of the cladding by Wei et al in 2015 [46]. Günendi et al theoretically and experimentally demonstrated broad-band single-mode guidance in HCF with 6-capilllary cladding design. The attenuation was around 0.18 dB/m at 1.6 μm which was a lot higher than the state of the art [47]. Another HCF with a hexagonally shaped core surrounded by 6 capillaries was demonstrated and exhibited three transmission windows spanning over a spectrum from the near infrared down to deep ultraviolet wavelengths with about 3 dB/m for all transmission windows [48]. Later in 2016, Michieletto et al numerically demonstrated the advantage of 7 capillary cladding design of HCF in higher-order mode suppression [49].

Our group reported low loss single mode performance in HCF by introducing the 7 ice-cream shaped capillary cladding design [50, 51]. S^2 imaging measurement was used to analyse the spatial modes [50, 52]. By comparing the mode properties in 7-capillary and 8-capillary HCF, high order modes are significantly suppressed in 8-capillary HCF.

1.1.4 Applications of hollow core fibres

Hollow core fibres are newly developed optical fibre waveguides with unique properties which can be used in many applications such as defence, security, atmosphere monitoring, and medicine [53-56]. My research on HCFs mainly focuses on the high power delivery especially in mid-infrared and gas and light interaction in the HCFs.

1) High power delivery in mid-infrared

One of the advantages is the low transmission loss in mid-infrared (mid-IR) region [36]. Compared to conventional solid core fibres, the material absorption of the cores are the main limit of the fibre performance in mid-IR. The most common material, the silica glasses, tend to contain some impurities such as water content. The infrared transmission is limited by the strong water absorption peaks [57]. Besides, since the fabrication technique of HCFs matures, the attenuation is as low as mentioned in the previous section.

As for laser transmission, hollow core fibres have a better performance than the conventional index guiding fibres because the small overlap between air core and the cladding can reduce the nonlinearities and material absorption. Guidance of the 10.6 μm CO_2 laser radiation through $As_{30}Se_{50}Te_{30}$-glass hollow core fibres was demonstrated [32]. The loss at 10.6 μm was estimated about 11 dB/m [32]. In the mid-infrared spectrum, the delivery of high energy microsecond pulses through a HC-NCF at 2.94 μm was found [32]. The NCF attenuation was measured to be as low as 0.183 dB/m at 2.94 μm by cut back measurement [32]. The maximum output energy delivered through NCF was achieved of 195 mJ which was limited by laser power [58]. My research on gas fibre laser is pumped by a high power continuous wave (CW) Erbium-Doped Fibre Amplifier (EDFA) with a maximum of 9.6 W [59].

2) Light and gas interaction platform

The materials of the solid cores in conventional fibres are the main cause of the sometimes unwanted nonlinear properties. However, fibre cores with air have

reduced nonlinear properties. HCFs is also capable of confining different media such as gases and liquid in the hollow core, which allows the interaction between light and said media across a relative long effective interaction length and high intensities. This property can also be applied in investigating the nonlinear properties of gas, leading to the making of optical sensors and gas fibre lasers.

Kagome fibre was first filled with hydrogen gas to produce stimulated Raman scattering (SRS) in 2002 [22]. Since then, a series of studies on SRS in gas filled HCF was reported. A gas filled fibre laser was reported as a Raman NCF laser in 2014 [60]. The SRS at 1.9 μm was generated in a 6.5 m long C_2H_2-filled HC-NCF at 23 bars, pumped by a 1064 nm microchip laser [60]. SRS was also observed in an ethane-filled HCF pumped with a high peak power pulsed 1064 nm laser [61]. A maximum peak power of about 400 kW and laser slope efficiency of 61.5% were achieved in a 6 m HCF at 2 bars pressure at1552.7 nm Stokes wavelength [61].

Population inversion of acetylene gas was also observed in Kagome fibre in 2011 [62]. Other gases such as HCN, CO and CO_2 were then used as active gas gain medium to demonstrate in HCFs at their own emission wavelengths [63-65]. In the mid-IR spectrum, 3.16 μm mid-infrared emission was achieved in the single pass of silica NCF filled with Acetylene gas pumped by a 1.5 μm tunable diode laser [66]. A ring cavity based acetylene filled fibre laser was demonstrated in 2016 [67]. Due to the guidance mechanism of anti-resonance, broadband transmission spectra and a large mode area can be achieved to make a high power laser system possible.

The study of nonlinear optics in the gas filled HCF is of interest recently [68]. With different gases filled into the HCF, several dramatic results are demonstrated including soliton compression to few-cycle pulses [69], widely tunable deep-ultraviolet light sources [70], novel soliton-plasma interactions [71] and multi-octave Raman frequency combs [72]. These light and gas interactions provide many applications in nonlinear optics.

1.1.5 Summary of projects reported in this thesis on hollow core fibres

My contribution to this topic described in this thesis is briefly shown as follows. S^2 imaging measurement was set up to measure the mode properties in the hollow core fibres. The mode contents in two different HCFs were measured and analysed. A new design of 7 capillary HCF showed a better performance to supress the high order modes and transmit only single mode in a relative long distance. From this discovery, we published two papers on the single mode performance of the HCF [50, 51]. Details are provided in Chapter 4.

1.2 Lasers

Laser is one of the most influential technological achievements of the 20th century, because it is widely used in all aspects of our daily lives today from laser pointers to surgery, from telecommunications to 3D printing. Based on the stimulated emission of radiation, a laser is a device that emits light through an optical amplification process. The term ‘laser’ originated as an acronym for ‘light amplification by stimulated emission of radiation’ which was first introduced to the public in Gould's 1959 conference paper [73]. Later in 1960, the first working laser was made by Maiman who used a solid-state flashlamp-pumped synthetic ruby crystal to produce red laser light at 694 nm wavelength. This laser was only operated as a pulsed laser due to its three-level pumping scheme [74].

Unlike other light sources, laser light fundamentally has its unique properties which makes it applicable in many areas. Firstly, laser light is concentrated in a narrow range of wavelengths, i.e. they are monochromatic. Lasers often have single frequency while other sources emit a broadband continuous light at a wide range of wavelengths. Secondly, lasers emit light coherently, which means all the emitted photons have a constant phase relationship with each other in both time and phase. Highly directionality is another property of lasers. Other light sources emit light in all directions while laser light is usually low in divergence, leading to a low radiation incident per unit area.

Typically a laser consists of three important components: a gain medium, an excitation mechanism and an optical resonator. The gain medium is a material containing atoms which are able to amplify the incident light by stimulated emission. The light at a specific wavelength is amplified when passing through the gain medium. Currently popular gain media can be gases, liquids, semiconductors and crystals.

The excitation mechanism is a source of energy to excite the atoms to specific energy states. This process is called pumping, with energy supplied optically like a laser diode or electrically like high voltage discharge.

The optical resonator reflects the laser beam through the gain medium for amplification. The most common setup is a cavity consist of a high reflectance mirror and an output coupler (usually partly transparent at the lasing wavelength) on either end of the gain medium. Light bounces back and forth between two mirrors and is amplified each time when passing through the gain medium.

1.2.1 How lasers work

To describe how the laser works, it is important to understand the stimulated emission and absorption first.

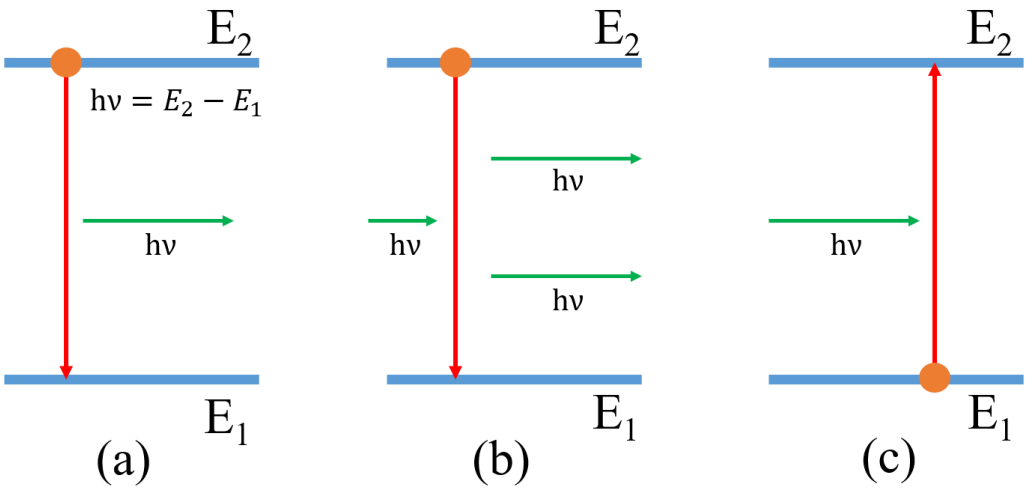

Fig. 1-3 Schematic illustration of the three processes: (a) spontaneous emission; (b) stimulated emission; (c) absorption.

Two energy levels (1 and 2), of some molecule or atom of a certain material, with their energies being E_1 and E_2, are given as Fig. 1-3. These two levels could be any two out of all the atom's energy levels. E_1 can usually be considered as the ground state. Assuming that the atom is initially at E_2 energy level, since $E_2 > E_1$, the atom will tend to decay to E_1 energy level with an energy release as E_2-E_1 by the atom. Spontaneous (or radiative) emission is the process when this energy is delivered in the form of electromagnetic wave. The frequency ν_0 of the radiative wave is given by a well-known equation:

$$\nu_0 = \frac{E_2 - E_1}{h} \qquad \text{Equ. 1-4}$$

Where *h* is Planck's constant. The emission of a photon energy is $h\nu_0 = E_2 - E_1$ when the spontaneous emission occurs and the atom decays from E_2 energy level to E_1 energy level (shown in Fig. 1-3 (a)).

In terms of stimulated emission (shown in Fig. 1-3 (b)), assuming that the atom is still initially at the E_2 energy level, when an electromagnetic wave with a frequency $\nu = \nu_0$ is incident on the material, there is a finite probability that the wave will force the atom transit from E_2 energy level to E_1 energy level. In this case, the energy difference $E_2 - E_1$ is delivered in a form of an electromagnetic wave which adds to the incident wave.

There are some fundamental differences between spontaneous emission and stimulated emission. In spontaneous emission, the emitted waves don't have any defined phase relationship with each other, i.e. the wave can be emitted in any direction. As for stimulated emission, since the emission process is forced by a wave with specific frequency, the emission atom adds in phase to the incoming wave and along the same direction.

Absorption is another important process for lasers which is shown in Fig. 1-3 (c). Assuming that the atom is initially lying in E_1 energy level, an incident wave with a frequency $\nu = \nu_0$ comes into the material, there is a finite probability to raise the atom to E_2 energy level. The energy difference $E_2 - E_1$ is required for the atom to transit from E_1 to E_2 energy level.

Briefly, in the spontaneous emission process, an atom decays from E_2 to E_1 with an emission of one photon. In the simulated emission process, an incident photon stimulates the transition from E_2 to E_1 and we have two photons. In the absorption process, the atom only transit from E_1 to E_2 by absorbing the incident photon. These processes provide basic idea for the lasing mechanism.

The gain medium usually contains a population of atoms. By using an external source of energy optically or electrically, the atoms can be excited to an upper energy level during the absorption process. The stimulated emission process amplifies the incident beam in the gain medium at the same time. In practice, the

atoms can interact with light by either absorption or emission. Emission can be either spontaneous or stimulated. In the case of stimulated emission, the output photons are in the same direction with the incident photons. When the number of atoms in one excited state is greater than the atoms in some lower energy state, population inversion is achieved. In this case, when the incident light passes through the gain medium, the amount of the stimulated emission is larger than the amount of absorption. Light is then amplified. When the incident light only passes through the gain medium once, this device which amplifies the light is called optical amplifier. When an optical amplifier is placed inside an optical resonator as I mentioned above, an optical oscillator is obtained.

In an optical resonator, multiple reflections of light pass through the gain medium to excite the atoms or stimulate the emission, which makes the stimulated emission dominate the spontaneous emission. So the incident light is amplified and results in a coherent output as laser beam. Since the resonator is typically a cavity consisting of two mirrors, the coherent beam travels bi-direction back and forth in the gain medium. Some of these coherent photons go out through the output coupler. Some are lost due to absorption or diffraction. If the amplification in the medium is larger than the resonator losses, the power of the recirculating light can exponentially rise. Every stimulated emission returns one atom from the excited states to a lower state which decreases the gain. The gain saturation occurs when the net gain (gain minus loss) reduces with an increasing beam power. In a continuous wave laser, the balance of the gain saturation and the cavity loss decides the equilibrium value of the laser power inside the cavity. The equilibrium status decides how the laser operates. If the pump power is too small, the gain will never be sufficient to overcome the cavity losses. A laser beam will never be produced. The lasing threshold is the minimum pump power needed to start the lasing process [75].

Due to different materials for gain media, lasers have a variety of types. The gain medium is selected for the desired lasing wavelength. As previously mentioned, the gain medium can be gas, solid, liquid or semiconductor. To fully understand discussion throughout my thesis, I introduce fibre lasers and gas lasers briefly.

In terms of the gas lasers, they are extremely common in not only lab research but also industry with their relatively low cost. The gas laser is usually pumped electrically or optically. The spectral region of the electrical discharged gas laser is ranging from deep ultraviolet wavelength (e.g. 224 nm in Helium-Silver laser [76]) to far infrared wavelength (e.g.10.6 μm in CO_2 laser [77]).

Optically-pumped molecular gas laser has a spectral region ranging from 1 μm to 1 mm. The laser configuration is much more simplified than the electrical-discharged one. However, since the gas absorption has to depend on the emission lines of other gases as the pump source, the development of the optically pumped laser is limited.

A traditional fibre laser is a laser in which the gain medium is an optical fibre doped with rare-earth elements. Optical nonlinearity is another way to generate laser like Stimulated Raman Scattering (SRS) in such lasers. Fibre lasers offer numerous advantages over traditional bulk lasers in terms of efficiency, compactness, robustness, beam quality and other characteristics.

Hollow Core Optical Fibre Gas Lasers (HOFGLAS) are developing rapidly due to their compactness, high damage thresholds and a wide coverage of the wavelengths [63]. These kinds of lasers combine the advantages of both gas lasers and fibre lasers. In terms of the traditional gas lasers, they offer high output powers but with short effective interaction lengths in bulky gas cells. Traditional solid core fibres have low damage thresholds. The nonlinear effects in solid glass materials limits the narrow linewidth of the generated light especially at high powers.

1.2.2 Mid-Infrared fibre lasers at 3 μm

Mid-IR lasers are of interest because of their wide applications in defense, remote sensing and medicine at the eye-safe wavelength of 3 μm. Mid-IR fibre lasers have developed rapidly in recent years due to the mature fabrication of soft glass and soft-glass fibre, as well as the advanced fibre laser technologies proven in the development of near-infrared fibre lasers [78-80]. The high loss of the silica, and the limit of the rare earth materials at mid-infrared wavelengths above 3 μm, means that rare-earth-doped silica and silicate fibres fail to provide the efficient laser operation [57]. Although inferior to silica/silicate glasses as laser host glasses in terms of mechanical strength, chemical durability, thermal conductivity, and optical nonlinearity, the soft glasses, e.g. Chalcogenide, Telluride and Fluoride glasses, offer advantages as host materials because of their much lower density of phonon states [79, 81].

Among many soft-glass fibre lasers, Ho-doped and Er-doped ZBLAN fibre lasers are capable to generate power at around 3 μm [82]. For high-power mid-infrared fibre lasers, Er-doped ZBLAN fibre laser was demonstrated as a successful candidate which generates 30 Watt mid-infrared laser output at wavelengths near 3 μm [83-86], with a predicted potential exceeding the 100 W power level [86]. By using a monolithic erbium-doped fluorozirconate fibre, lasers with an output of 5.6 W and longer wavelengths up to 3.55 μm can be achieved [87]. The high achievable doping level and low material loss make the high power performance outstanding in ZBLAN fibre lasers [78]. However, the host materials influence the high power output in numerous ways including the typically high quantum defect, thermal management and fibre failure [79].

As an alternative technology, novel gas-filled hollow core fibre lasers were invented [63]. They make full use of the advantage of low-loss hollow core fibres which can easily transmit the mid-infrared light in their multiple transmission bands. Also the filled gas can be changed and the pressures adjusted conveniently. The gas-filled hollow core fibre lasers have demonstrated an alternative potential route for high-power mid-infrared laser emission [88].

Acetylene is a gain medium which can emit in mid-infrared region [63]. It was first used in the optically-pumped gas fibre laser in 2011[62]. In their single-pass amplified spontaneous emission (ASE) configuration, they used nanosecond pulses from an Optical Parametric Oscillator to pump at 1.52 μm wavelength and generated two mid-infrared emissions at 3.12 and 3.16 μm. The gain fibre was a 'Kagome' type of anti-resonant HCF filled with acetylene [62]. The output power was low because of the high fibre loss (20 dB/m) at the laser wavelengths.

In 2013, a single pass pulsed laser was demonstrated with an output of over 0.7 μJ around 3 μm and 30 % power conversion efficiency pumped by a diode laser system at 1.53 μm. The fibre they used is a 11 m long anti-resonant HCF with losses reduced to less than 0.2 dB/m at both pump and laser wavelengths [66]. They also revealed that the gas pressure played a decisive role in efficient laser operation [66], as in the earlier studies of traditionally optically pumped gas lasers [89]. Later, 1.4 μJ pulse energy at 3 μm was obtained by pumping with a narrow-bandwidth OPA at 1.53 μm wavelength in single-pass configuration with a 10 m long acetylene-filled anti-resonant HCF [88]. The slope efficiency stayed at 20 % which was unaffected by the acetylene pressure [88]. It may be a feature of lasing in the transient regime. The laser output beam quality M^2 was measured as 1.2 , which indicates a good beam quality [88].

By using a synchronous diode-pumping scheme, the first cavity-based mid-infrared laser oscillation in acetylene-filled hollow fibre was realized in a ring cavity [67]. In the pulsed laser setup, a low-loss anti-resonant HCF with 101m in length was employed as a feedback fibre with 25 dB/km fibre loss at 3.1 μm [67]. A maximum power of over 4 mW average output power was achieved at a repetition rate of 2.5 MHz. In the CW laser setup in the same paper, the feedback fibre was changed to 3m in length and the lasing of acetylene molecule at 3 μm was also observed with CW diode laser pumping in the cavity configuration as the first time [67]. Later, we compared lasing in the cavity and single-pass configurations under high-power pump [59]. We demonstrated that the single-pass configuration was preferred for high-power operation. Recently, over 1 Watt mid-infrared laser output at 3.1 μm was achieved in our CW laser system by using a diode laser pump. Over 33 % conversion

efficiency was measured in a 15 m anti-resonant HCF of single-pass configuration, relative to the absorbed pump power.

1.2.3 Summary of projects reported in this thesis on mid-IR lasers

In Chapter 5, an optically pumped acetylene filled HCF laser was demonstrated in both cavity and single pass ASE configurations. With the high pump power, the single pass ASE configuration has a robust performance with the output power of over 1 W and the slope efficiency of 33%. Considering the pump absorption of the laser, we demonstrate that the dynamics of the gain molecules constrains the laser performance under high-power CW pump.

1.3 Conclusion

Chapter 1 briefly introduces the development, guiding mechanism and mode property of the hollow core fibre and their applications. It also introduces how the laser works and the development of the gas fibre lasers.

HCF is a novel and simple design after the appearance of the photonic bandgap fibre. It has low loss transmissions in multiple wavelength bands, which makes it interesting in fibre optics field. The guiding mechanism is generally explained by "ARROW" model. It intrinsically has all the modes but with different attenuations. Single mode guidance is achieved based on the design of the HCF. HCF has a wide range of the applications due to its unique optical characteristics. High power delivery in mid-infrared region and gas-light interaction platform are its two main ways for applications especially in my research.

How the laser works is briefly introduced in the second part of this chapter. Lasers are divided by different gain materials. Gas lasers and fibre lasers are two main categories of the laser. Gas fibre lasers appeared after the advent of the HCF. They combine the advantages of the gas lasers and the fibre lasers. In my thesis, a gas fibre lasers is demonstrated in mid-infrared region.

CHAPTER 2 GAS FILLED FIBRE LASER MECHANISM

In this chapter, the development of the gas lasers is introduced briefly in section 2.1. In section 2.2, gas molecules especially C_2H_2 molecule is discussed as a gain medium for a laser.

2.1 Introduction of gas lasers

The first gas laser was invented with He-Ne gas as gain media by Javan *et al* in 1960 [90]. Since then, gas lasers were designed and developed with different gases and used for many purposes. A variety of active gas media used are either single atoms or molecules and even metal vapour. The gas laser develops from the earliest CH_3F [91], CO_2 [92], and OCS [93], to CO [94, 95], HBr [96], HCN and C_2H_2 [65]. All of these gases can be pumped optically.

In fact, the most common pumping method of gas lasers is an electrical discharge. The gas laser was first operated on converting electronic energy to a laser light output in continuous wave operation. CO_2 laser achieves a high continuous wave output power of 150 kW at 10.6 μm with fairly high beam quality. However, the wall-plug efficiency is only above 10% for CO_2 laser. As for He-Ne laser and Argon ion laser, the efficiency is as low as 0.1%. In this case, more efficient lasers like solid-state and diode are being used [97].

Optically pumped gas molecule lasers (OPML) have a lot of advantages to guarantee its increasing attention and development. For example, a gas medium is easy to cool down by convection and has a relatively high damage threshold. Since lots of gases are used, the laser spectra covers from the ultra violet (UV) to the millimetre wave region, which results into a broad range of applications especially in the specific wavelengths that are not valid for other types of lasers [98]. The

disadvantages are obvious. First, it is hard to find a suitable laser source to pump the specific wavelengths of these gas media. Then, due to the order of hundreds of MHz of the linewidth in a molecular gas, it is necessary to have a narrow band pump source to transfer the pump energy into the gas.

Semiconductor laser diode source is a good choice to use for pumping gas medium because of the available laser diodes with the wavelength ranging from visible to above 2 μm laser transitions [99]. The quantum cascade diode laser was demonstrated to be ideal for pumping the triatomic molecule based laser (like CO_2 and N_2O) with output in the wavelength range of 3~15 μm [99]. HBr lasers pumped by a Nd: YAG laser [100] and a single frequency Ho:YLF laser [101] respectively were demonstrated in 4 μm. Near infrared emitting diode lasers are used for pumping diatomic molecules including HF, DF, HCl, HBr, and CO [99]. Diode pumped gas lasers have a great potential to achieve high output power with good beam quality [102-104].

The first optically pumped alkali atom laser was demonstrated in 2003 [105]. High quantum efficiency was achieved up to 98% [104] in optically pumped Rb vapour lasers with the slope efficiency of 81% at a wavelength of 795 nm [105]. Another alkali vapour, Cs, was also used as gain media in the laser and achieved the efficiency of over 63% at a wavelength of 894 nm [106]. Multiple laser diode array pumped Cs laser was demonstrated with a maximum output power of 48 W [107].

The main problem of the optically pumped gas laser is that the conventional gas cells cannot provide a long enough interaction length between pump and media, leading to a limitation of their applications with such bulky systems. In fact, the conventional gas laser can only contain around 1meter gas tube as a resonator while the new gas fibre laser has much longer length like 40 meters in my experiment. A new generation of the gas laser has been developed, which is the gas-filled hollow core fibre laser (reviewed in chapter 1).

2.2 C_2H_2 molecule as active media

To fully understand the OPMLs, a review of molecular physics related OPMLs is presented in section 2.2.1 and 2.2.2. In section 2.2.3 and 2.2.4, the basic principles of the operation of a C_2H_2 molecule as a gain medium is described.

2.2.1 Energy levels of molecules

Typically electrical energy levels of molecules have the largest separation of a few eV, which implies that their allowed absorption transitions are in the visible or ultraviolet regions of the spectrum [108]. In fact, the molecules are capable of storing energy in two extra forms: vibrations and rotations.

At each electronic state of the molecule, there are several possible vibrational levels. They are spaced equally in ladder-like levels. At around each vibrational level, a series of rotational energy levels stay even more closely but not with equal spaces. In this case, transitions between vibrational states are generally in the mid-infrared region of spectrum. Pure rotational transitions are observed in the far-infrared and microwave regions. The possible transitions are determined by certain selection rules.

A molecule with N atoms has 3N degrees of freedom. Three of these are motion directions. Three are rotational motions around three axes, or two for linear molecules. The rest are vibrational motions. C_2H_2 is a kind of linear molecule which contains 2 degrees of rotational motions and 5 degrees of vibrational motions.

1) Rotational energy levels of linear molecules

The linear molecules have the rotational kinetic energy which is expressed as:

$$E_{rot} = \frac{1}{2} I\omega^2 = \frac{L^2}{2I} \qquad \text{Equ. 2-1}$$

where I is the moment of inertia of rotation and ω is the angular velocity of rotation. L is the angular momentum $I\omega$ which is expressed as:

$$L^2 = J(J+1)\hbar^2 \qquad \text{Equ. 2-2}$$

where *J* is the angular momentum quantum number with values of *J*=0, 1, 2,….

In terms of radiations with changes in rotational levels, the selection rules for rotational transitions in linear molecules can be expressed as follows:

$$\Delta \mathrm{J} = 0, \pm 1$$

The possible transitions occur between rotational levels with either same *J* value or different *J* values by a separation value of ± 1.

2) Vibrational energy levels

The model of the vibration levels of a molecule can be compared to a simple harmonic oscillator with two atoms attached to a vibrating spring. In the harmonic oscillator model, the potential energy is calculated by $\sum_i \frac{1}{2} k_i \, x_i^2$, in which k_i is the effective spring constant of the ith vibration mode and x_i is the displacement from the equilibrium position. Then the vibrational energies are solved as this:

$$E_{vib} = \left(\upsilon_1 + \tfrac{1}{2}\right) h\nu_1 + \left(\upsilon_2 + \tfrac{1}{2}\right) h\nu_2 + \cdots; \quad \text{Equ. 2-3}$$

where ν_1, ν_2, … are the resonant frequencies of the oscillator and υ_1, υ_2 are the vibrational quantum numbers for each vibrational mode. This value can only be integral values from 0 upwards.

The selection rule for vibration transitions with one vibration mode is $\Delta\upsilon = \pm 1$ for pure harmonic motion. However, molecules sometimes do not behave as independent simple harmonic oscillators. An additional transition, named overtones, is allowed as well.

3) Rotational-Vibrational transitions

A molecule can vibrate and rotate at the same time. As mentioned before, a series of rotational energy levels lie on each vibrational energy level, with spaces between two neighbouring rotational energy levels smaller than the spaces between vibrational energy levels. In such rotational-vibrational levels, transitions from a rotational sublevel of one vibrational level to another rotational sublevel of another vibrational level are called rotational-vibrational transitions.

When this transition occurs between two sublevels, the J selection rule for rotational-vibrational transitions is

$$\Delta J = 0, \pm 1.$$

The rule dictates that there are three branches (P-, Q-, R-branches) to the band which are lines connecting rotational sublevels in one upper vibrational level to the rotational sublevels in the lower vibrational levels as:

$$\Delta J = +1, \quad P - branch,$$

$$\Delta J = 0, \quad Q - branch,$$

$$\Delta J = -1, \quad R - branch.$$

The energy diagram of the transitions between two rotational sublevels in two different vibrational levels of a molecule is shown in Fig. 2-1.

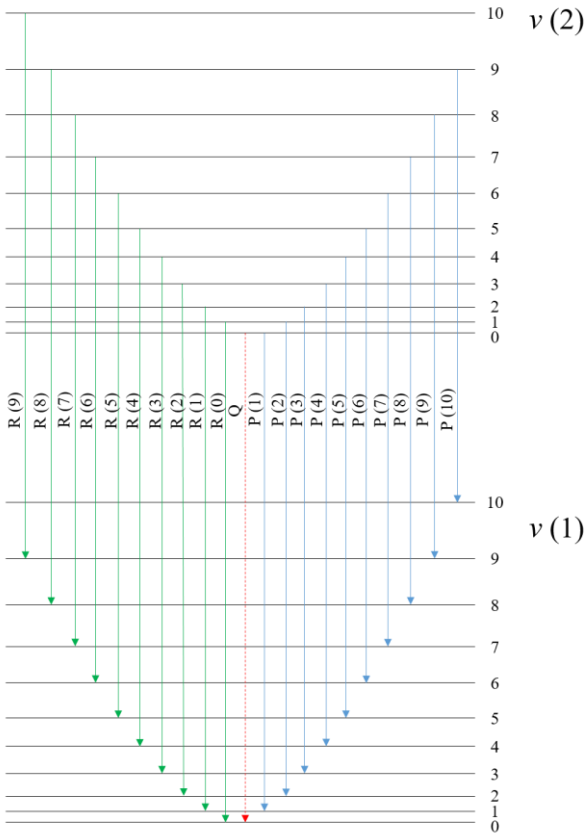

Fig. 2-1 Energy level diagram of two vibrational levels containing a series of rotational sublevels. P-, Q-, R-branch transitions are presented.

In Fig. 2-1, the dash line presents the Q-branch transition when ΔJ equals 0. For all stable diatomic molecules (except NO) and some other linear molecules, transitions with Q-branch are not allowed because the orbital angular momentum is zero in upper and lower vibrational states.

Note that the lower states can be either the initial levels or the final levels [109]. They depend on the direction of the transitions, i.e. the transitions for absorption or emission. For example:

R (1) is a transition from $J = 1$ to $J = 2$ in absorption

$J = 2$ to $J = 1$ in emission.

2.2.2 Optically pumped molecule lasers (OPMLs)

Optically pumping is a process to inject light to raise not only the electrons from a lower energy level of an atom or molecule to a higher energy level, but also the low vibrational and rotational energy level of an atom or molecule to a higher energy level. In lasers or laser amplifiers, optically pumping is to achieve a population inversion in the gain medium and then obtain the optical amplifications via stimulated emissions.

Various lasers can be optically pumped including all the doped-insulator solid state lasers, some of the semiconductor lasers and gas lasers. Some common optical pump sources are discharge lamps and laser diode.

The mid-infrared molecular gas lasers are based on vibrational-rotational transitions. There are three transition methods of pumping and lasing for mid-infrared OPMLs including fundamental band transitions, difference band transitions, overtones and combination bands transitions. The transition into the first excited vibrational levels are called fundamental bands, such as the transition (000) → (010) for CO_2. The fundamental bands lasers have same vibrational band but different rotational bands for both pumping and lasing. The second laser scheme is to excite the fundamental vibrational band to an upper level. Then lasing occurs on the different band with the transition from one vibrational mode to another (e.g. (100) → (010)). It is also possible to excite from ground state to a combination level with

several different vibrational modes at same time (e.g. (000) → (011)) or to an overtone level (e.g. (000) → (020) or (003)). Then lasing takes place on the transition to another vibrational state. Hot band lasers are either based on combination and overtone bands [110].

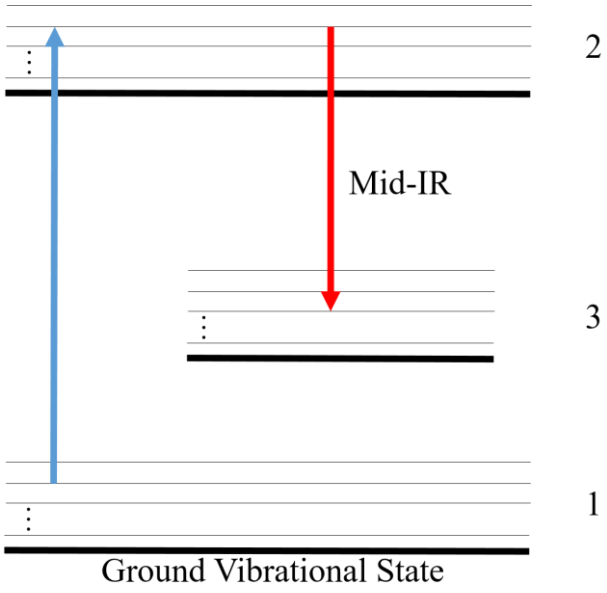

Fig. 2-2 Simplified energy level diagram of a molecule with three energy levels.

Fig. 2-2 shows a simplified energy diagram of a molecule for understanding the basic operation of OPMLs. State 1 is the ground vibrational state. State 2 represents the excited state while state 3 is the laser terminal state. The pumping process is to excite the molecules from the ground vibrational state to the excited state via rotational-vibrational transition. Then the excited molecules lase on transitions from the pumped state to another rotational-vibrational state. Since each vibrational state has a series of rotational states, with the resonant or near-resonant excitation of the vibrational-rotational transitions, coherent emission occur either on a pure rotational transition (leading to far-infrared emission) or on a vibrational-rotational transition (leading to mid-infrared emission).

Collision is a channel for the transfer of energy which affects the population numbers of molecule states. The rotational relaxation and the vibrational relaxation are two processes of the collision induced energy transfer. The molecule population in the excited state transfer energy either by stimulated emission (lasing) or collisions. Therefore the laser gain depends on not only the strength of pumping and

lasing transitions but the competition between lasing and relaxation processes. So the performance of the laser is the balance of the pump transition, the laser transition and the collisions induced population transfer process.

In terms of infrared gas molecule lasers, some common gas molecules are investigated as active gain medium including CO, CO_2, C_2H_2 and HCN. The pumping and lasing parameters are listed in Table 1. Among them, both C_2H_2 and HCN are attractive because of the strong absorptions in the 1.5 μm region [111, 112] which is suitable for the optical communication C-band wavelength range. The lasing wavelengths are at 3.1 μm in the mid-infrared region. My research focuses on the C_2H_2 molecule as a gain media in the optically pumped laser system.

Table 1 Some common gas media with pumping and lasing parameters.

Gas	Pumping			lasing		
	λ (μm)	Vibrational state	Cross-section (cm^2)	Vibrational transition	Cross-section (cm^2)	λ (μm)
C_2H_2	1.52	v_1+v_3	8.7e-18	$\rightarrow v_3$	2.8e-16	3.1
HCN	1.53	$2v_3$	4.1e-18	$\rightarrow v_3$	4e-16	3.1
CO	1.57	v=3	1.5e-20	$\rightarrow 1$	1.1e-17	2.36
CO_2	2.00	$2v_1+v_3$	1.8e-18	$\rightarrow 2v_1$	9.4e-15	4.3

The C_2H_2 molecule has been used as gain media since 1975 in both discharge [113] and optical pumping scheme [114]. Later a group at Kansas reported that C_2H_2 gas was applied in a fibre gas laser with the emission at mid-infrared region of 3.1-3.2 μm [115]. Based on population inversion, the optically pumped fibre gas laser achieved a slope efficiency of only a few percent mainly due to the high loss of the fibre.

Recently, the Kansas group reported an OPA-pumped acetylene-filled Kagome-shaped hollow core fibre laser that achieved a highest energy of 1.4 μJ and the slope efficiency of 20% with a good beam quality of $M^2 = 1.15$ [88].

2.2.3 C_2H_2 molecules

An acetylene molecule has 4 atoms and 12 degrees of freedom. Since the molecule is linear and symmetric, it has 5 vibrational states shown in Fig. 2-3. The energy levels of acetylene vibrational normal modes are named C_2H_2 ($v_1v_2v_3v_4v_5$). Fig. 2-3 shows five vibrational normal modes including three stretching modes $v_1v_2v_3$ and two bending modes v_4v_5. Two bending modes are doubly degenerated as they could be simply created by rotating the molecule ninety degrees around the innernuclear axis.

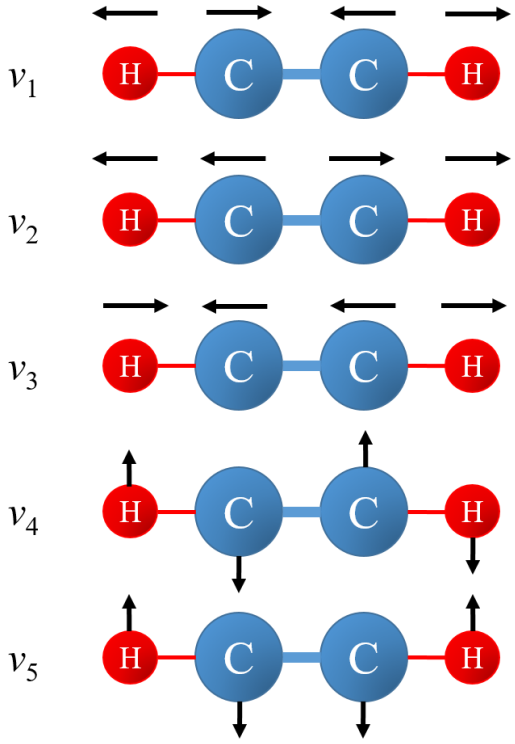

Fig. 2-3 C_2H_2 vibrational normal modes.

Among these vibrational modes, a vibrational C-H symmetric stretch mode (v_1) and a vibrational C-H antisymmetric stretch mode (v_3) are of interest. The pump transition at 1.5 μm is the (00000) → (10100) transition which is one of the main topics in this thesis. It indicates the transition from the ground vibrational state to the overtone vibrational state of v_1+v_3. The potential lasing wavelength of 3.1 μm is obtained from (10100) → (10000) transition. There are several other possible dipole-allowed transitions with the expected emission wavelengths presented in Table 1.

Table 2 Several possible dipole allowed transitions of acetylene originating from the pumped state (10100).

Dipole allowed transitions	Transition wavelength (μm)
(10100) → (00000)	1.5
(10100) → (00010)	1.6
(10100) → (01000)	2.1
(10100) → (00100)	3
(10100) → (10010)	3.7
(10100) → (11000)	7
(10100) → (11010)	14

An example of the energy level diagram is presented in Fig. 2-4 with the specific pumping wavelength of 1.5 μm and lasing wavelength of 3.1 μm. The blue P (9) arrow is pump transition from ground vibrational state (00000) to an upper vibrational state (10100) with a wavelength of 1.53 μm. The selection rules allow the rotational energy level with J=8. At the excited vibrational state, the non-radiative transition possibly occurs and returns to the ground state as the grey dash arrow shows. The potential lasing transition at 3.1 μm of acetylene can be obtained from (10100) to (10000). According to the rotational selected rules, the R branch and P branch transitions, corresponded to ΔJ=+1 and ΔJ=-1, make two possible lasing transitions of R (7) and P (9) at wavelengths of 3.12 μm and 3.16 μm [116].

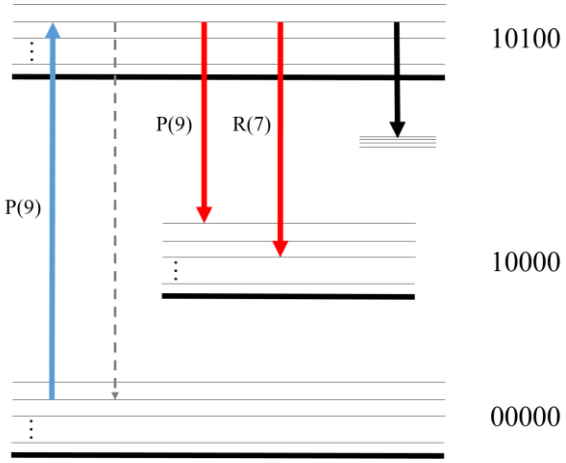

Fig. 2-4 A simplified energy level diagram of certain transitions of acetylene molecules: a P branch pump transition P (9) (blue arrow) from J=9 to J=8 (vibrational state (00000)→(10100)); two lasing transitions (red arrows) at R branch and P branch from J=8 to ΔJ=±1 (vibrational state (10100)→(10000)) [116]; the dash arrow indicates the non-radiative

transition back to the ground state; the black arrow stands for any other possible transitions of acetylene.

At room temperature, on the basis of the Boltzmann distribution, maximum population occurs in the rotational state with J=9 for acetylene. R branch transitions with ΔJ=+1 occur at higher energies than P branch transitions, which means the R branch transitions have shorter wavelengths. It is intuitively seen from the absorption spectrum of acetylene with $\nu_1+\nu_3$ (10100) rotational-vibrational state shown in Fig. 2-5. Q branch does not exist as explained in last section as there is no angular momentum associated with the vibrational modes in this linear molecule.

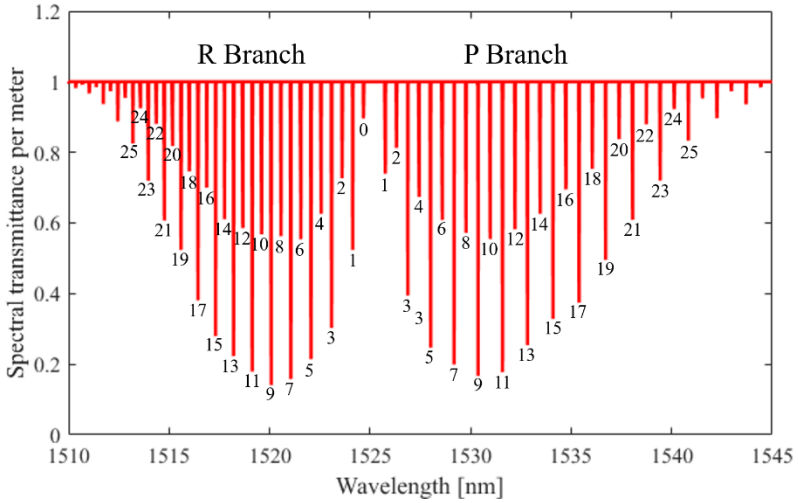

Fig. 2-5 Normalized acetylene absorption spectrum ranging from 1510 nm to 1545 nm at room temperature, within R branch and P branch marked [117].

The HITRAN database [117] provides some parameters from the transition (00000) to (10100) to calculate that the absorption cross section is between $8.8 \times 10^{-22}\ m^2$ to $7.2 \times 10^{-22}\ m^2$ for pressures from 1 torr to 10 torr (1.33 mbar to 13.33 mbar) at room temperature [97]. In the same way, the emission cross section for the transition (10100) to (10000) is estimated to be between $2 \times 10^{-20}\ m^2$ to $1.4 \times 10^{-20}\ m^2$ for the pressure from 1 torr to 10 torr. The lifetime due to the spontaneous emission of the transition (10100) to (00000) is about 0.1 s and (10100) to (10000) is about 0.017 s.

Collision induced energy transfer are also worth considering. The state to state rotational relaxation rate of acetylene molecules by a buffer gas of Ar is about

$1 \times 10^{-16}\ m^3 molecules^{-1} s^{-1}$ [118]. The vibrational relaxation rate for (00100) state has been reported to be the order of $10^{-19}\ m^3 molecules^{-1} s^{-1}$ without identified energy pathway of the collision [119].

2.3 Conclusion

Chapter 2 presents the development of gas lasers especially the optical pumped molecular lasers. Acetylene gas molecule properties are introduced as a gain medium.

Gas lasers has two pumping methods including electrical discharge and optically pumped. Laser diode source is a good choice as a pump source which provides a wide range of wavelength. It also has a high slope efficiency and quantum efficiency. The disadvantages of the gas lasers are the short length of the gas-light interaction and the bulky system.

Molecules have rotational and vibrational energy levels. Molecule gas lasers are based on vibrational-rotational transitions. Acetylene gas molecule has 5 vibrational states ($v_1v_2v_3v_4v_5$). In the mid-infrared laser, pump transition at 1.5 μm is (00000) → (10100) transition and the lasing wavelength of 3.1 μm is obtained from (10100) → (10000) transition.

CHAPTER 3 FABRICATION OF ANTI-RESONANT HOLLOW CORE FIBRES

Unlike the traditional solid core fibres, hollow core fibre has a unique fabrication method called “stack and draw”. The fabrication process is presented in section 3.1. In 3.2, the transmission attenuation of the hollow core fibre is demonstrated in different wavelengths.

3.1 Fabrication process of hollow core fibres

3.1.1 Introduction of the fibre fabrication

The manufacture of step index fibres starts with a doping process called modified chemical vapour deposition (MCVD) [126]. A traversing oxy-hydrogen torch heats a rotating tube of silica which is pumped through by high-purity gas mixtures. The amorphous particles caused by the hot zone deposit on the silica and form a pure layer. This procedure is typically repeated 30-100 times to build the cladding and the core from outside in layer by layer. After building up enough layers, the tube is heated again and collapses into a rod.

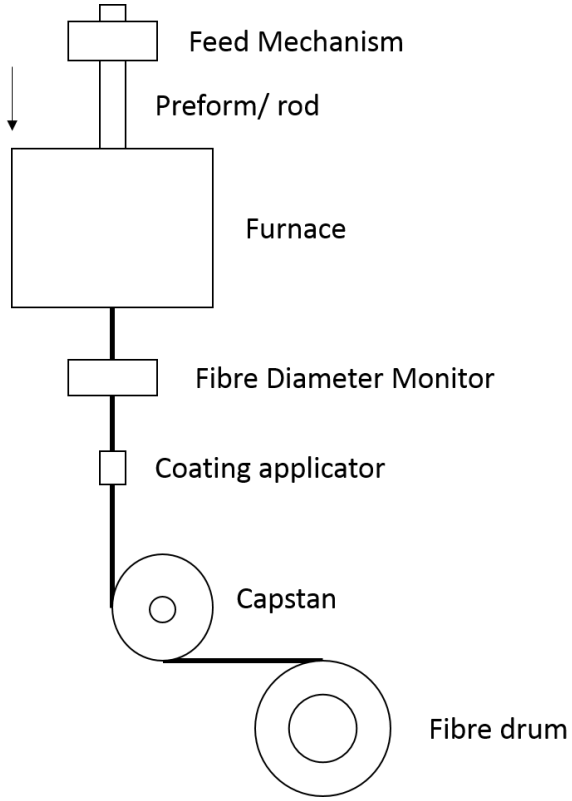

Fig. 3-1 Schematic diagram of a fibre draw tower.

The fibre draw tower, as shown in Fig. 3-1, is used to turn the resulting rod into the fibre. The preform, or the rod, is held vertically over a furnace operating at approximately 2000°C softening the silica and allowing it to be pulled. The rod is fed into the furnace slowly by the feed machine, the silica becomes softened and is drawn down to a fibre, and the fibre size is regulated by a monitor. The fibre then goes through a coating applicator and is coated with polymer, which makes the fibre more flexible and durable. Finally, the fibre winds onto a rotating fibre drum after a series of capstan wheels.

As photonic crystal fibres (PCFs) were developed, the manufacturing techniques have changed. The method for this kind of fibre is normally the stack and draw method. This technique was first used for fabricating speciality optical fibres in 1974 [13]. Later in 1996, the first all silica single mode PCF was reported by fabricating with stack and draw technique [20]. This method offers high flexibility in fibre design, speed of fabrication and repeatability in either industry or laboratory.

Like the fabrication of PCF, HCF is also produced by stack and draw technique. The basic idea is to build a stack of a desired structure first and then draw it to a fibre with a smaller diameter. There are four steps to this fabrication method.

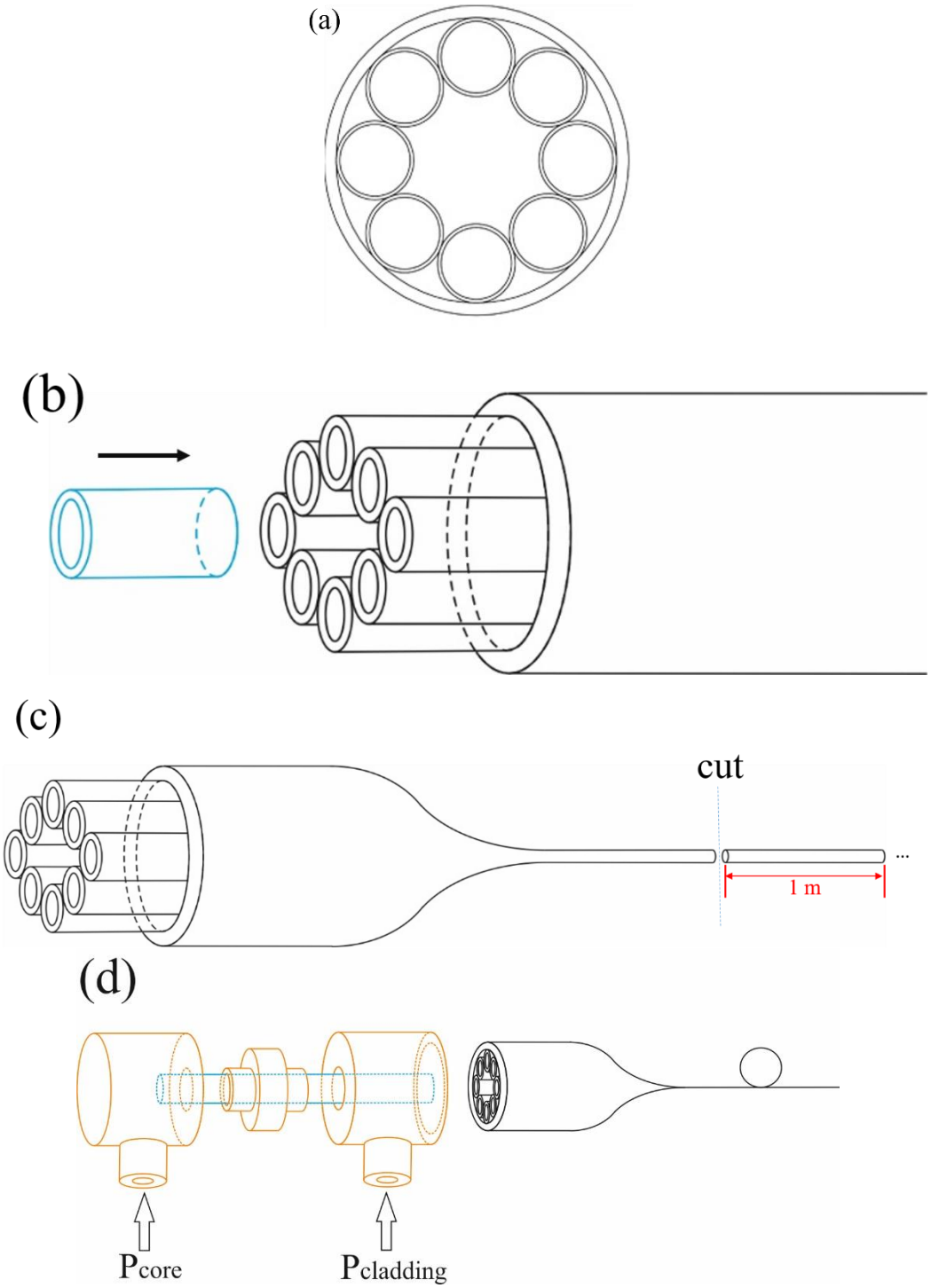

Fig. 3-2 (a) Cross section of the designed stack. (b) Schematic of the stack process at one end, the other end is same. (c) Schematic of cane drawing process: the preform is drawn to

canes. (d) The process of cane to fibre: brass fitting for applying pressure is applied onto the top of the cane. The core and cladding are pressurized with different routes.

1) **Designing**

Firstly, the structure of the fibre is precisely designed. Take one of HCFs with 8 capillaries as an example. All material used in my fabrication were from the F300 fused silica from *Heraeus* with low concentration of OH-group [127]. The ideal cross section of the cane is that 8 capillaries touch their two neighbours and also the inner surface of the outer big tube as shown in

Fig. 3-2 (a). All the capillaries are drawn from a commercial silica cylinder to the identical ones with smaller diameter.

2) **Stacking**

According to the designed pattern in the previous procedure, 8 capillaries are inserted into another commercial silica tube which is called a jacket (shown in

Fig. 3-2 (b)). To ensure the stack with eight capillaries does not collapse, another two short capillaries are inserted into the centre of the stack at each end to keep the capillaries separate. Usually the stack is 20 or 25 mm in outer diameter in practice.

3) **Drawing of cane**

Under a high temperature conditions, the amorphous material with fine structures is sensitive to collapse due to a large drawdown ratio. Since the stack diameter is much larger than the diameter of the fibre, there is an intermediate preform which is called cane. The stack is drawn to many canes with diameter and length of approximately 1mm and 1m respectively (shown in

Fig. 3-2 (c)). Sometimes the outer tube of the cane is too thin and can break. It is usually inserted to another tube with thick wall.

4) Drawing of fibre

In this process, the cane is assembled with a metal holder at one end. The metal holder set consists of three parts as shown in

Fig. 3-2 (d). A very thin tube is fixed in the middle part of the metal holder set which sealed with glue. There is no air path between the core and cladding. Gases with different pressures fill the core and the cladding tubes respectively through the brass fitting. The homogeneous pressurized tubes ensure the fibre has a good structure. The furnace temperature, the gas pressures and the feed and draw speed need to be finely adjusted to make sure the fibre is uniform from the beginning to the end. The fibre outer diameter and the fibre tension are monitored during the drawing process. The bare fibre should be coated with a layer of polymer material immediately to prevent from breaking and enhance its strength. The drawing and coating part is completed in the same stage, the same as is used in fabricating step index fibres like Fig. 3-1.

During the drawing process, the parameters of the core size and core wall thickness need to be calculated and controlled precisely to result in the desired transmission band. Moreover, the pressure should be controlled properly to avoid the capillaries inside from collapsing or being broken when drawing the cane to fibre.

3.1.2 Challenges of hollow core fibre fabrication

Even though the negative curvature fibre is the simplest design of hollow core fibre, to fabricate a uniform one is challenging. Failures happen easily in any process and any aspect such as deformation of structure and collapsed holes. Making good canes are the foundation of the good quality of the HCF. Fusion between capillaries or the jacket tube and capillaries are important for good fibre fabrication. Some parameters should be mentioned during the process.

1) Design of the capillary size

Before we draw a real fibre, we need to design the fibre structure. The size of the capillary in the cane is calculated. In my experience, the diameter of the capillary less than 0.5% in variation is helpful for stacking. The uniformity of the capillaries is necessary as well. Oversized capillaries cannot be inserted into the tube while the undersized ones easily cause failure of forming negative curvature core wall. If the capillary is not uniform along the length, it means at some points it is oversized and at some other points it is undersized. It is easy to break when the capillary is inserted into the tube one after another.

2) Low temperature

In the fabrication process with a higher temperature, the silica glass has a less viscosity and a greater surface tension which may cause capillary collapse in the cladding. Lower temperature is a preference. In my fabrication of the cane, the furnace temperature is usually set between 1880℃ to 1920℃ which is a low temperature in silica glass fabrication. In the fabrication of the fibre, the temperature is set between 1900℃ to 1920℃.

3) Pressure control

In Fig. 3-2 (d), P_{core} and $P_{cladding}$ are the pressures in the core and the cladding separately. To make a fibre with good quality, $P_{cladding}$ should be higher than P_{core}. The core boundary is pushed from the capillaries to the core and forms the negative curvature shape. To make the pressurisation simple, P_{core} is kept connecting the atmosphere and $P_{cladding}$ is connected to nitrogen gas with higher pressure. The pressure difference is usually kept between 6 kPa and 60kPa from my experience.

During the fabrication process, these three points above are the keys to a good fibre. However, some other parameters and skills are still under investigating. Firstly, uniformity of the fibre is important for low loss transmission. Currently there is still no way to monitor the uniformity inside microstructure of the fibre. The only method is to monitor the outer diameter of the fibre during the drawing process. If the fibre outer diameter keeps in a stable value all the time, the fibre is assumed to be uniform. This method cannot detect the change of the microstructure of the fibre. When there are some defects inside the fibre, we have no idea to find out where it is. Secondly, the fibre with smaller size for short wavelength transmission is more difficult to fabricate. The degradation of the cladding structure usually happens during the fabrication. Too little silica material and too much surface tension may cause this problem. It is found that low furnace temperature and short time in the furnace are best ways to get rid of the degradation. However, it still need to be investigated in the future.

3.2 Fibre attenuation measurement

3.2.1 Fibre attenuation experimental setup

Cut-back measurements are usually employed to experimentally measure HCF attenuations. The schematics in Fig. 3-3 display the setups of the measurement. Usually HCF has multi transmission bands covering a wide range of wavelengths. The optical spectral analyser measures from 600 nm to 1700 nm while the monochromator (*Bentham TMc300*, with a 300 lines millimetre grating and a liquid nitrogen cooled InSb detector) measures longer wavelengths. That is the first difference between Fig. 3-3 (a) and Fig. 3-3 (b).

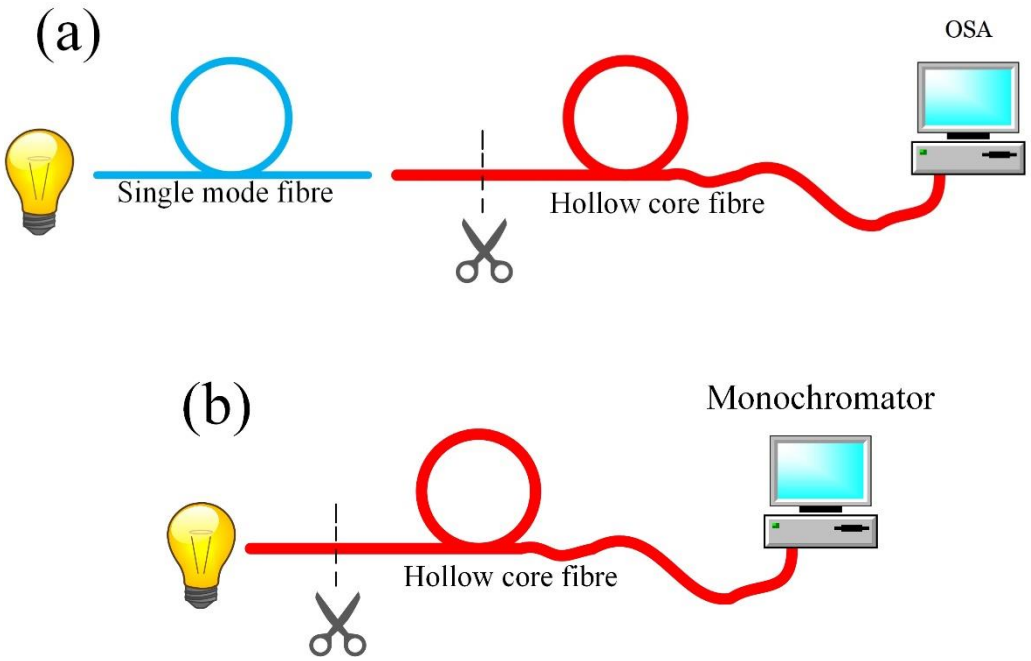

Fig. 3-3 (a) Schematic of cut-back measurement by OSA (wavelength range: 600 nm ~ 1700 nm); (b) Schematic of cut-back measurement by monochromator (wavelength range: 250 nm ~ 5400 nm)

The procedure of the cut-back measurement is simple: measure the output spectra before and after the cut-back. The input to the HCF should be kept the same at all times, and not disturbed. The fibre attenuation of the cut piece is expressed as:

$$\alpha\,(\lambda) = \frac{1}{\Delta L} \times 10 \times \log \frac{P_2(\lambda)}{P_1(\lambda)} \qquad \text{Equ. 3-1}$$

in which, ΔL is the cut fibre length. $P_1(\lambda)$ is the output power of original long fibre before cutback while $P_2(\lambda)$ is the power of the remaining fibre after cutback.

The light source is an important component of the measurement. Firstly, the emission spectrum of the light source should cover the transmission range of the HCF. Normally a stable tungsten halogen bulb with high brightness acts as a broadband light source in my experiment.

When the transmission bands of the fibre under test is below 1700 nm, a standard single mode fibre is used to transmit and butt-couple light into the HCF (shown as Fig. 3-3 (a)). When the transmission bands are above 1700 nm, the monochromator is employed to record the spectrum as Fig. 3-3 (b). In this case, the light source is directly coupled light into the HCF because the solid core fibre has an extremely high loss at longer wavelengths above 2000 nm. If the fibre under test is long enough and has multi transmission band covering from visible to mid-infrared region, two cut-back measurements with different setups (Fig. 3-3 (a) and (b)) are needed.

There are some difficulties that we have to consider that may influence the results. Firstly, the cut fibre length is important. When the incoherent light with multimode is coupled into the HCF, several modes are transmitted in the first few meters and most high order modes leak out. Then the mode condition keeps stable in the rest of the HCF. Thus the cut point should be somewhere with stable transmission, which means it cannot be too close to the fibre input end. In addition, if the cut length is too short, the two spectra before and after cut-back have no significant difference, leading to inaccurate results. Secondly, bending loss is another factor which may affect the measurement accuracy. Keeping the fibre in a large loop diameter on the bench is an easy and effective way to prevent bending loss. In my experiment, the loop diameter is always larger than 1 m.

3.2.2 Fibre attenuation experiment results

Take one of my measurements as an example.

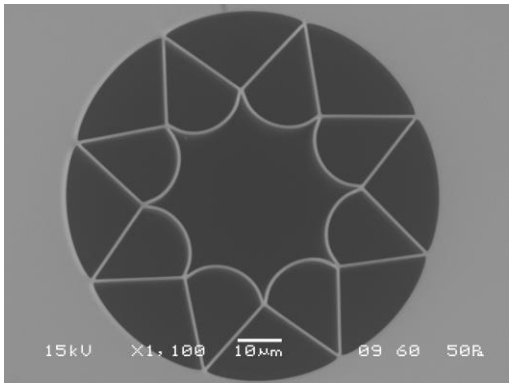

Fig. 3-4 Scanning electron microscope image of AR-HCF of 8 capillary cladding design with low loss transmission bands centred at 1 µm. The inscribed diameter of core region is about 36 µm.

Fig. 3-4 is a hollow core fibre fabricated for spatial modes investigation in Chapter 4. It is 57 m long with a 36 µm core diameter. According to Equ. 3-3 in 3.1.2 related to the resonant (high loss) wavelengths, the calculated high loss wavelengths are 0.85 µm and 0.57 µm (*m* equals to 2 and 3 respectively) which are in agreement with the transmission spectra (shown in Fig. 3-5), with a refractive index of 1.419 and call wall thickness of 0.85 µm.

Since the first transmission band is around 1 µm. The spectral characteristics of this fibre are measured by an OSA (*Ando AQ-6315A*). The attenuation experiment set up is shown in Fig. 3-3 (a).

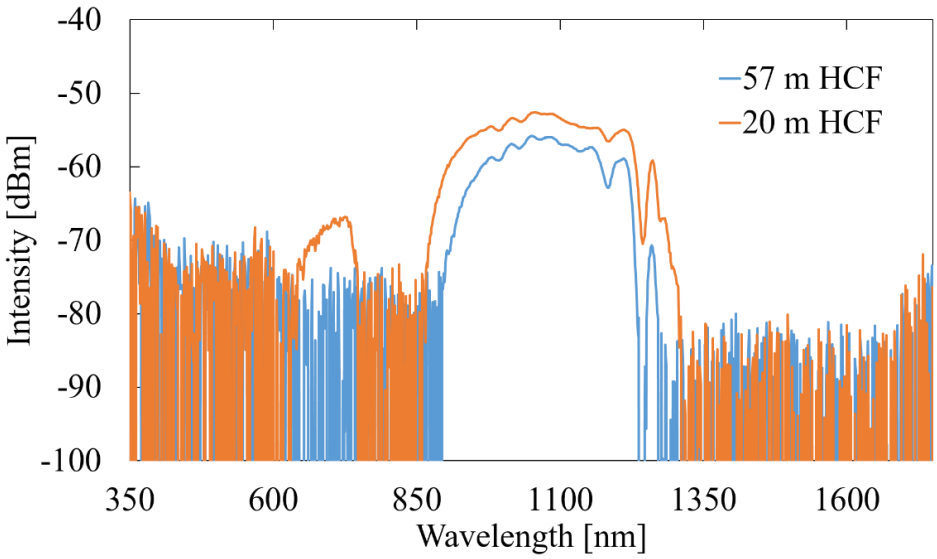

Fig. 3-5 transmission spectra of the 8-capillary HCF with 57 m and 20 m in length.

In this cut-back measurement, the original fibre with 57 m in length was cut to 20 m, keeping the coupling condition still. As shown in Fig. 3-5, the transmission bands span from 650 nm to 750 nm and 870 nm to 1300 nm.

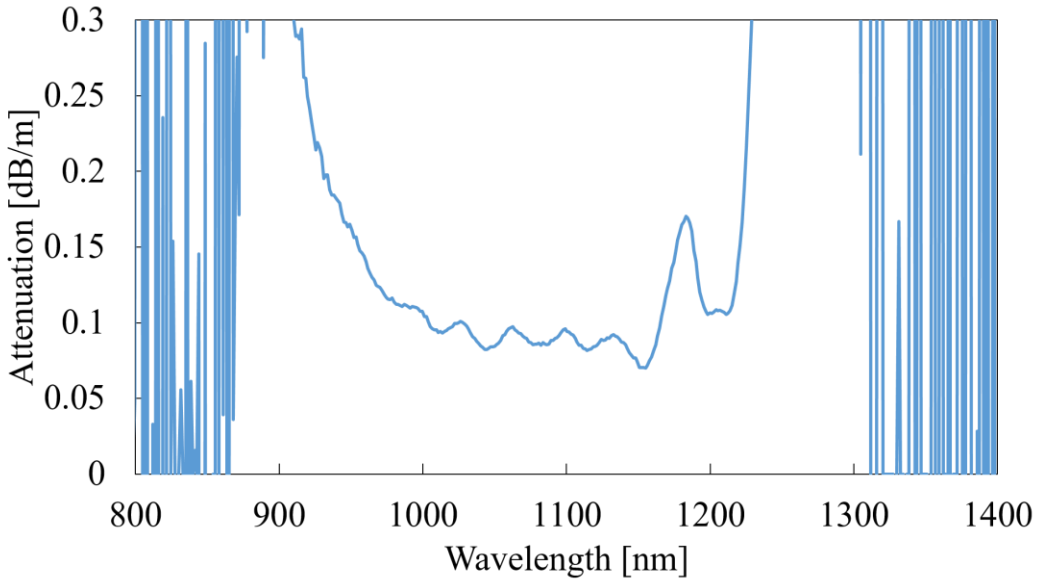

Fig. 3-6 Attenuation of the 8-capillary HCF.

In Fig. 3-6, the lowest attenuation is measured to be 0.07 dB/m at 1155 nm. The attenuation spectrum is calculated as Loss=10×log ($P_{20\ m}$ / $P_{57\ m}$)/37 m. Below 900 nm, there is a high loss band which is due to the structural loss feature which is a resonance of the core wall.

This is the simple example of cut-back measurement with a transmission band using only OSA. In chapter 5, a HCF with two transmission bands covering both 1.5 μm and 3.1 μm wavelengths needs two cut-back measurements including Fig. 3-3 (a) and (b). Details are given in chapter 5. Here are the transmission spectra measured by monochromator before and after the cut back (148 m and 30 m).

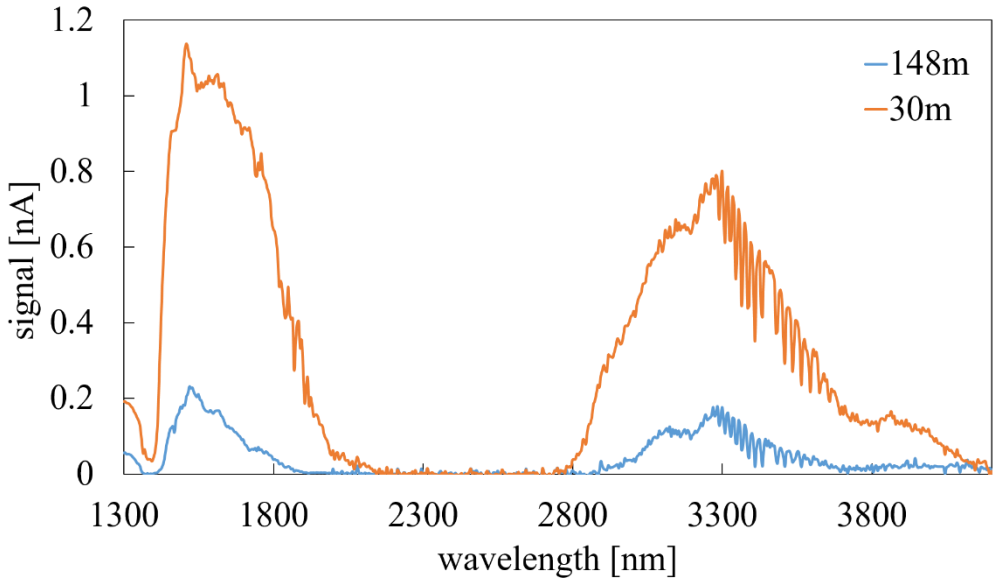

Fig. 3-7 Transmission spectra from 1300 nm to 4000 nm of a 10-capillary HCF used as gain fibre in Chapter 5.

The absorption peaks can be obviously seen in the transmission band from 3300 nm to 3700 nm in Fig. 3-7. This is consistent with the HCl gas absorption spectra both in wavelength and relative strengths according to the HITRAN database [128]. It is reasonable to assume that the HCl absorption peaks are from the initial material F300 which contains some Chlorine. A good way to remove these absorption peaks is to purge the fibre with nitrogen and keep it desiccated.

In addition, other absorption materials in this HCF should be considered. CO_2 in the air core absorbs the light in the wavelength band between 4.2 μm and 4.3 μm [129]. At 2.69 μm and 2.76 μm wavelengths, there are two CO_2 main absorption lines [129]. H_2O vapour is another material absorbing the light at the wavelength around 1.9 μm and 2.7 μm [127]. Silica has extremely high attenuation at wavelength above 2.6 μm. As a result, the attenuation in the HCF at above 2.6 μm is significantly high due to CO_2, H_2O and silica absorption. Besides the gas absorption lines at mid-IR wavelength, HCF has a much lower attenuation than the standard silica core fibre, which makes HCF unique and very useful for many applications in this wavelength region.

3.3 Conclusion

In this chapter, the process of the fibre fabrication is demonstrated in details. The transmission attenuation measurement of HCF is introduced.

The stack and draw technique is a general method for hollow core fibre fabrication. It usually has four steps including designing, stacking, draw of cane and draw of fibre. Three key skills and parameters are discussed to confirm a high quality fibre such as size design, low temperature and pressure control. Currently there are some fabrication problems unsolved including the uniformity monitoring and degradation in the HCF for short wavelength.

Cutback measurement is a general method for measuring the attenuation in the HCF. It is firstly introduced in theory. In the experiment, the hollow core fibre is made with the transmission window at 1μm which matches the theory. The attenuation is around 0.07 dB/m at a wavelength of 1155 nm. Other absorption materials in this HCF transmission are also introduced.

CHAPTER 4 SINGLE MODE PERFORMANCE IN HOLLOW CORE FIBRES

Hollow core fibres typically have no specific cutoff at all spatial modes. Different modes are lost with different attenuations along the fibre length during the light delivery. To achieve single mode operation, as required by the applications, a 7-capillary negative curvature hollow core fibre is investigated and proved to guide light in a single mode over a short length of transmission. To fully understand the modes in the fibre, an S^2 imaging measurement is used to detect the mode shape. In section 4.1, the background, principle and experimental setup of the S^2 imaging measurement are described. In section 4.2, the modes in 7- and 8-capillary HCFs are compared by adopting the S^2 imaging measurement.

4.1 S^2 imaging measurement

4.1.1 Background of S^2 imaging measurement

Today, specific attention has been paid to the modal characteristics of the fibre laser beam. While single mode fibres are known for their excellent beam quality, multimode fibres, which enable containment of higher order modes and support a higher power, can decrease the beam quality.

M^2 is a typical parameter used to describe the quality of the beam. When M^2 has a very low value (close 1), the beam can be considered as an equivalent to a single mode operation with a stable beam. However, it is still possible to achieve a low value even when the fibre contains a large number of higher order modes. M^2 also varies when the phase of the modes change.

In the past few years, beam quality measurements have rapidly developed in terms of accuracy [130]. With the development of the optical devices technique, the optical correlation analysis relying on the correlation filter method can even be used in real time. Such optical correlation methods include computer-generated holograms [131] and spatial-light modulators [132]. However, this method is still limited by the speed, accuracy and price of the hardware.

There are also several numerical methods which can decompose the mode content. Numerical techniques can retrieve the phase of an optical field from one simple intensity profile [133]. There are different algorithms that can do this such as [134, 135]. The most promising one among them is the stochastic parallel gradient descent (SPGD) algorithm [136] which can perform an accurate mode decomposition in on-line real time [137]. However, it can only be applied in certain fibres in which their modes can be determined in advance and using that information it can then reconstruct the mode pattern. This technique cannot be applied to some novel fibres whose modes are unknown, such as hollow core fibres.

Certain traditional techniques are still widely used, including the use of ring-resonators [138], S^2 [52] and C^2 [139] imaging methods which are based on multimode interference. The last two methods can provide very accurate mode contents both in amplitude and phase without assuming any optical properties of the test waveguide. The principle of these two methods is similar, which is analysing the interference between each mode. The difference between them is that the S^2 uses the fundamental mode of the test fibre as its reference mode, while the C^2 employs an external reference beam propagated in a single mode fibre.

As it is shown in the following section, an S^2 imaging method is capable of simultaneously imaging multiple, coherent, higher-order modes propagating in hollow core fibres. Not only can different types of mode patterns be reconstructed, but the Multi-Path Interference (MPI) levels can be quantified as well. In addition, it will be demonstrated later how the modes change when the fibre bends.

4.1.2 Principle of S^2 imaging measurement

Spatially and spectrally resolved imaging, or simply the S^2 imaging method, can be used to decompose the mode content [52, 140]. When the light propagates in optical fibres, different modes can be identified by the group delay difference. This can lead to both a spectral interference pattern with a broadband source and an apparent spatial interference fringe visibility between the high order modes and the fundamental mode.

The setup of the method can be described as follows: light from a broadband source is launched into the fibre under test. At the exit of the fibre, the beam is imaged onto the end of a single mode fibre (SMF) which is coupled into an optical spectrum analyser (OSA). The SMF which acts as a probe is placed on an automated translation stage that moves the fibre end in x and y direction. At each (x, y) point, the optical spectrum can be measured by the OSA.

Assuming that two modes overlap spatially at one (x, y) point, they should have a spectral interference pattern due to the group delay difference between the two modes in the test fibre. The wavelength spectrum at that point should then be transformed to the frequency domain. After using the Fourier transform, the plot of this point can depict different mode beats at different group delay differences. The x axis of the Fourier transform needs to be normalized by the fibre length to obtain the group delay differences in unit of ps/m.

In theory, the group delay t is given as the reciprocal of the group velocity v_g [52]:

$$t = \frac{1}{v_g} = \frac{d\beta}{d\omega} = \frac{d\beta}{d\omega}\Big|_{\omega=\omega_0} + (\omega - \omega_0)\left[\frac{d^2\beta}{d\omega^2}\right]_{\omega=\omega_0} \quad \text{Equ. 4-1}$$

in which ω is the frequency and β is the phase constant for a wave. The first term in the equation is the modal group delay for a specific frequency and the second term is induced by the wavelength dispersion.

The group index of the material is defined as

$$N \equiv n - \lambda \frac{dn}{d\lambda} \quad \text{Equ. 4-2}$$

or

$$N \equiv n + k\frac{dn}{dk} = \frac{d(nk)}{dk} = \frac{d\beta}{dk} = c\frac{d\beta}{d\omega} \qquad \text{Equ. 4-3}$$

From the equations above, group delay differences between two modes can be expressed as

$$\Delta t = t_2 - t_1 = \frac{d\beta_2}{d\omega} - \frac{d\beta_1}{d\omega} \qquad \text{Equ. 4-4}$$

Using the group index equations, the group delay difference is derived as

$$\Delta t = \frac{1}{c}\left[(n_2 - n_1) + \lambda(\frac{dn_1}{d\lambda} - \frac{dn_2}{d\lambda})\right] \qquad \text{Equ. 4-5}$$

In this equation, the mode index can be calculated via the equation from chapter 3.

Multi-path interference (MPI) is a well-known impairment in optical communications systems that is caused by the beating of signals. It is defined as the ratio of powers of two modes, $MPI=10\times\log_{10}[P_{HOM}/P_{FM}]$ [141]. In this equation, P_{HOM} is the power of high order modes while P_{FM} is the power of fundamental mode. In order to calculate the relative power in each mode, Fourier transforms of the measured optical spectra are used. We assume two modes are present with spatially and frequency dependent amplitudes, $A_1(x, y, \omega)$ and $A_2(x, y, \omega)$, related by a constant $\alpha(x, y)$ which is assumed to be independent of the wavelength, such that

$$I_2(x, y, \omega) = \alpha^2(x, y)I_1(x, y, \omega) \qquad \text{Equ. 4-6}$$

If the group delay difference between two modes in assumed to be independent of frequency, the spectral intensity caused by interference between the two modes can be written as

$$I(x, y, \omega) = I_1(x, y, \omega)[1 + \alpha^2(x, y) + 2\alpha(x, y)\cos(\tau_b\omega)] \qquad \text{Equ. 4-7}$$

where the τ_b is the period difference of the frequency between the two modes caused by their relative group delay difference. The Fourier transform can be written as

$$B(x, y, \tau) = [1 + \alpha^2(x, y)]B_1(x, y, \tau) + \alpha(x, y)[B_1(x, y, \tau - \tau_b) + B_1(x, y, \tau + \tau_b)] \qquad \text{Equ. 4-8}$$

where $B_1(x, y, \tau) = \mathcal{F}\{I_1(x, y, \omega)\}$ is the Fourier transform of the optical spectrum of a single mode. At a certain *(x, y)* point, the ratio *f(x, y)* is defined as the amplitude of the Fourier transform of the spectral intensity at the group delay difference of interest divided by the amplitude at zero group delay. The ratio can be written as

$$f(x,y) = \frac{B(x,y,\tau=\tau_b)}{B(x,y,z=0)} = \frac{\alpha(x,y)}{1+\alpha^2(x,y)} \qquad \text{Equ. 4-9}$$

So $\alpha(x, y)$ can be expressed as

$$\alpha(x,y) = \frac{1-\sqrt{1-4f^2(x,y)}}{2f(x,y)} \qquad \text{Equ. 4-10}$$

The total intensity $I_T(x, y)$ of the two modes measured in the OSA at a given (x, y) point integrated over the measurement bandwidth is the sum of the individual mode intensities: $I_T(x, y) = I_1(x, y) + I_2(x, y)$. The intensity of each mode can be written as

$$I_1(x,y) = I_T(x,y)\frac{1}{1+\alpha^2(x,y)} \qquad \text{Equ. 4-11}$$

$$I_2(x,y) = I_T(x,y)\frac{\alpha^2(x,y)}{1+\alpha^2(x,y)} \qquad \text{Equ. 4-12}$$

Therefore, at each *(x, y)* point, $I_1(x, y)$ and $I_2(x, y)$ can be calculated and the total MPI calculated from

$$MPI = 10log[\frac{\iint I_2(x,y)dx\,dy}{\iint I_1(x,y)dx\,dy}] \qquad \text{Equ. 4-13}$$

4.1.3 S^2 imaging measurement setup

In order to set up an experiment to acquire the image of the transverse beam profile, the first experiment to measure intensity distribution should be done. It is used to find the position of the beam waist in the x-y plane. The experimental setup is shown in Fig. 4-1.

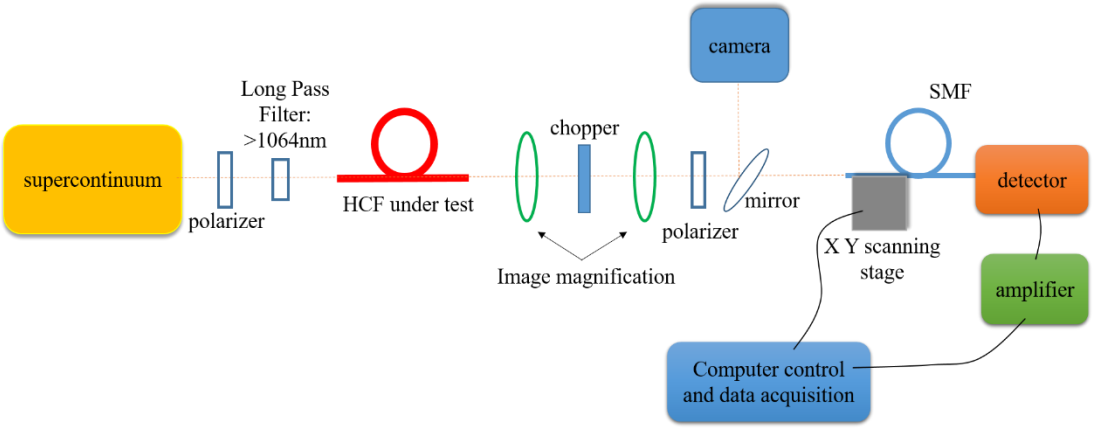

Fig. 4-1 Schematic of the intensity experiment setup.

In this experiment, the light source is a supercontinuum laser (Fianium SC400) which is stable and provides broadband light. After passing through a polarizer to make the light polarized and a long pass filter to eliminate the short wavelength light, the beam is coupled into the hollow core fibre under test.

The beam is then magnified using a set of lenses and is passed through another polarizer before arriving at the end of an SMF. The working lengths of two lenses are 9.01 mm and 160 mm. The magnification is 17.8. It means the beam spot diameter is 30 μm at the output of the fibre and it will be around 500 μm after the magnification. A mirror and a CCD camera are used to check whether the power of the light is almost in the core and how the beam profile looks like. Since the waist of the beam leads to the least error [140], the camera is also used to find the proper place of the beam waist. When the beam in the camera looks good enough, the light should pass directly into the SMF. The distance between both the SMF end and the camera with respect to the second magnification lens should be the same to ensure that the SMF captures the image of the beam waist. The SMF is connected to the detector to allow the power of each (x, y) point to be measured. The signal is amplified and the data is transmitted into the laptop. A LabView programme is

designed to automatically control the x and y scanning stage and acquire the data. The x and y scanning stage, consisting of a Newport controller and PI controller and it is set to scan a plane array of 20×20 points.

The scanning stage should be moved slightly along the beam axis to ensure the power that acquires it is all from the waist of the beam. The way to find the waist is simple: a whole image of intensity distribution for different z positions close to the waist should be scanned and the full width at half maximum (FWHM) of the beam needs to be measured. The waist is at the z position where the FWHM has the smallest value.

To test how the system works and the accuracy of the measurement, HCFs with 2 m and 19 m in length are used to analyse the mode property respectively. The beam intensity distribution of the 19 m HCF is shown in Fig. 4-2. The cross of the grid is each (x, y) point. The plot is made up of 400 points with their own power data.

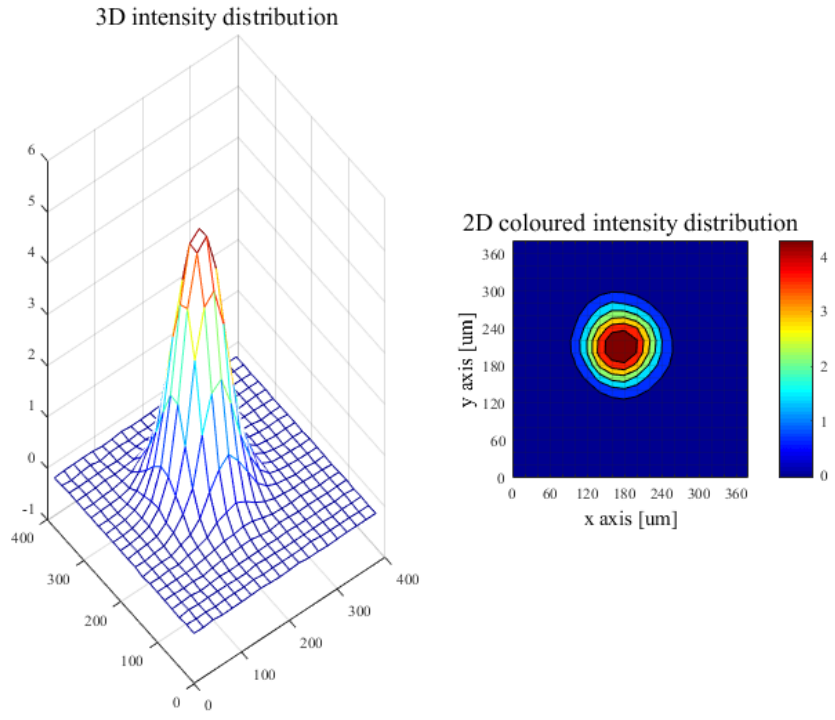

Fig. 4-2 the spatial pattern of the beam intensity distribution in 3D and 2D plot.

The S^2 imaging experiment setup Fig. 4-3 follows the one above. After acquiring the beam intensity distribution, the next step is to modify our experimental

setup for an S^2 imaging experiment. The setup is exactly the same as the one in Fig. 4-1 except that the detector is replaced by an optical spectrum analyser (OSA). The OSA can acquire spectrum information at each point and transmit it to the laptop. Another LabView programme is written to control both the stage and the OSA. The OSA is set as follows: Resolution: 0.02 nm; sensitivity: high 2; data: 501 points at each *(x, y)* position. The wavelength range is set 1075-1085 μm to obtain a group of data. Then it is set to 1040-1050 μm (without the long pass filter) to get another group of data for comparison. The whole measurement process lasts about 1.5 hours since there are 400 points to measure and each point takes 10 seconds.

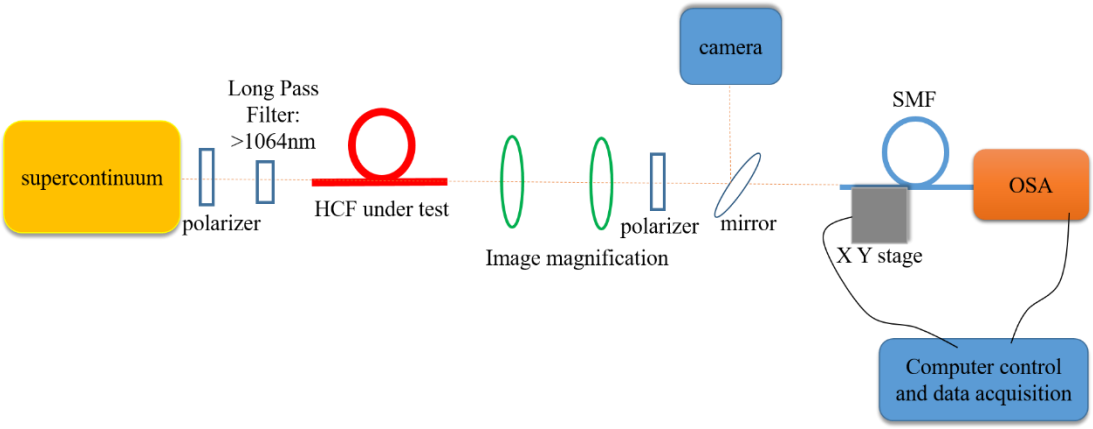

Fig. 4-3 Schematic of the S^2 imaging setup.

4.1.4 S^2 imaging measurement results

A typical optical spectrum measured at an arbitrary *(x, y)* point is plotted in Fig. 4-4. The wavelength range is 10nm between 1075-1085 μm. It is known that the fringes, shown in Fig. 4-4, are caused by the interferences between two different modes. The theory suggests [52], the longer the fibre is, more fringes the plot has.

By using two different lengths (2 m and 19 m) of the same fibre, the theory is confirmed (Fig. 4-4). More interference fringes result in more accurate figures after the Fourier transform. However, the fibre should not be too long because we are limited by the resolution of the OSA. For the 2 m long fibre, there are 13 cycles in the 10 nm wide spectrum, which means 0.77 nm/cycle. Assuming that only 4 points decide a cycle, the maximum resolution of the OSA is 0.02 nm. So a cycle should be

no shorter than 0.08 nm. Thus, the fibre length we prefer is 0.77×2/0.08=19.25 m at most. That is the reason of choosing the 19 m long fibre for the experiment.

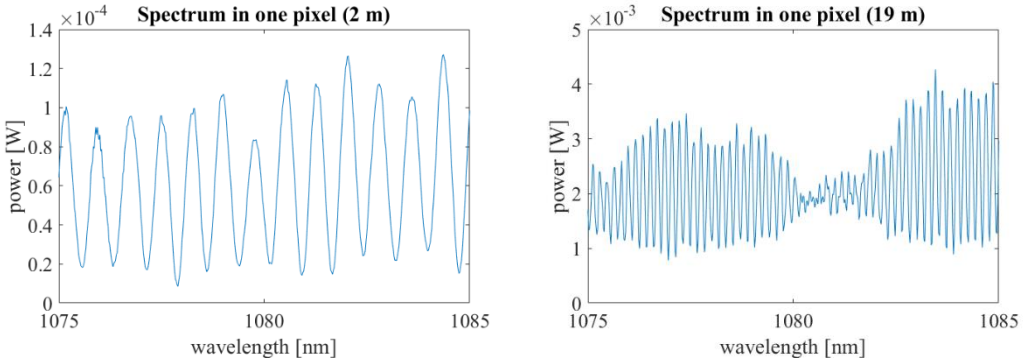

Fig. 4-4 Typical optical spectrum measured at an arbitrary (x, y) point.

Fig. 4-5 show the Fourier transforms of the optical spectra in Fig. 4-4 from the 2 m (left plot) and 19 m (right plot) fibres. Fourier filtering is used to pick out different peaks of interest. The horizontal axes are scaled by the fibre length to obtain the group delay difference in units of ps/m. As shown in Fig. 4-5, the plot obtained from the longer fibre piece provides better resolution (more points) than the shorter piece. This agrees with the theory in last paragraph, suggesting that having more interference between the modes, leads to a better resolution. The fibre used for these two measurements is the same (the only difference is the length) therefore we would expect that the peaks in the two plots should be at the same x positions. Fig. 4-5 indicates that this is the case which means the method used to discover the group delay is reliable.

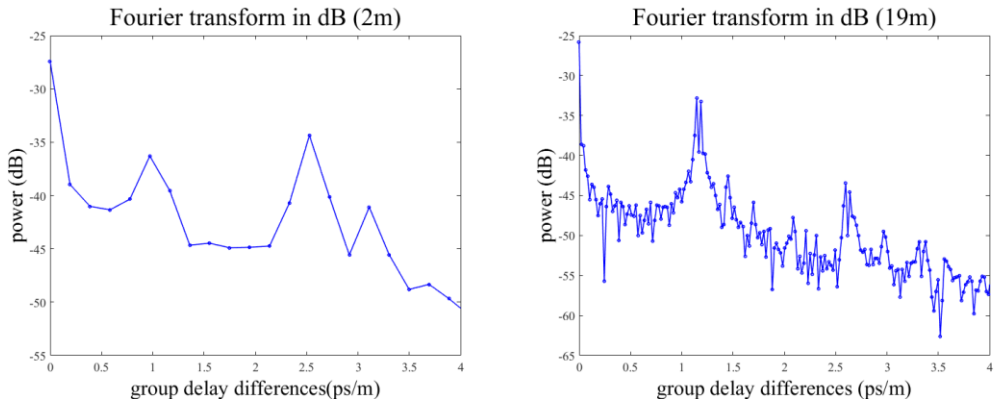

Fig. 4-5 the Fourier transform of the optical spectrum in Fig. 4-4

Each point in the array has its own Fourier transform like Fig. 4-5. By adding all the transforms from each point together, the plots shown in Fig. 4-6 are produced. Both plots show two peaks which may be related to some certain modes of interest.

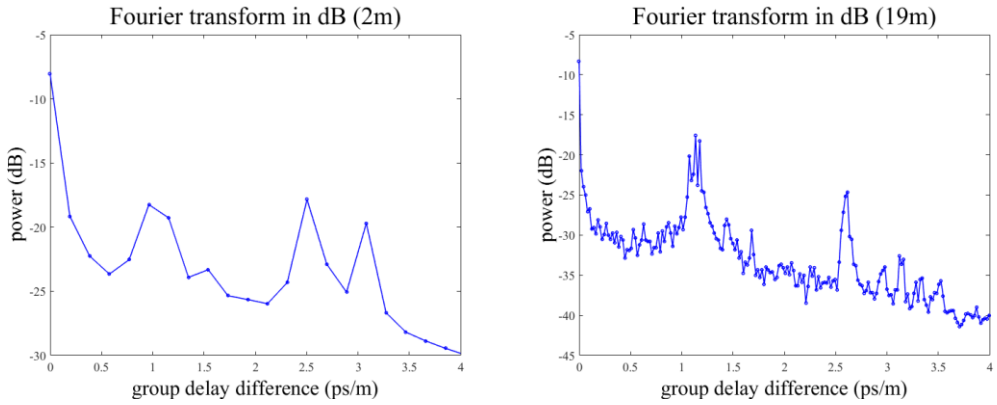

Fig. 4-6 the sum of the Fourier transform of each point.

To illustrate what the modes at each peak look like, Fig. 4-7 shows the patterns which consist of the power at each point in the array with a different group delay for the 19 m fibre piece. The upper pattern shows all the modes mixed together. Since the delay difference is zero at that peak, the modes can only beat with themselves. The reason that it seems to be a fundamental mode is that the power of fundamental mode has a large proportion of the total power. At the second peak, the pattern is like LP_{11} mode. It is the group delay difference between the fundamental mode and LP_{11} mode. Similarly, the LP_{21} mode pattern can be observed using the second peak. The results obtained from the 2 m fibre are the same.

In this way, it is easy to decompose the transverse modes in space as well as in spectrum. Unlike other methods, if there is sufficient time to acquire enough data, it is possible to discover all the modes which can be transmitted in the fibre.

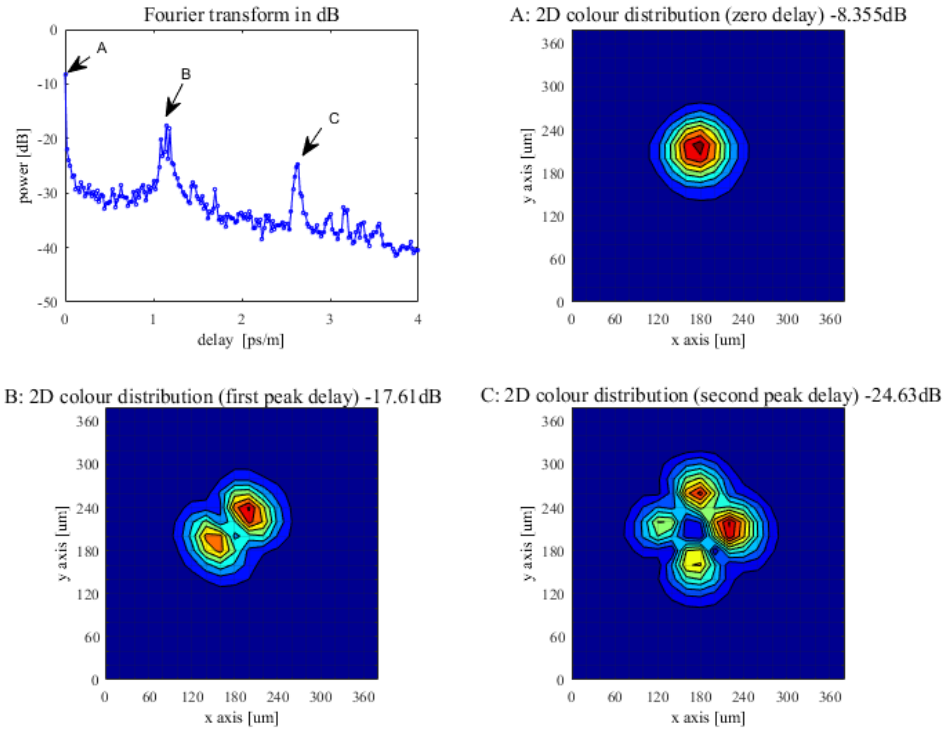

Fig. 4-7 The 19 m long fibre's Fourier transform sum at each point and the mode patterns at the zero delay position, first peak and second peak.

Comparing the previous results to a shorter wavelength in Fig. 4-8, the delay time at each peak is shorter when the measurement shifts to a shorter wavelength: 1040-1050 nm. It can be inferred that the dispersion is related to the wavelength.

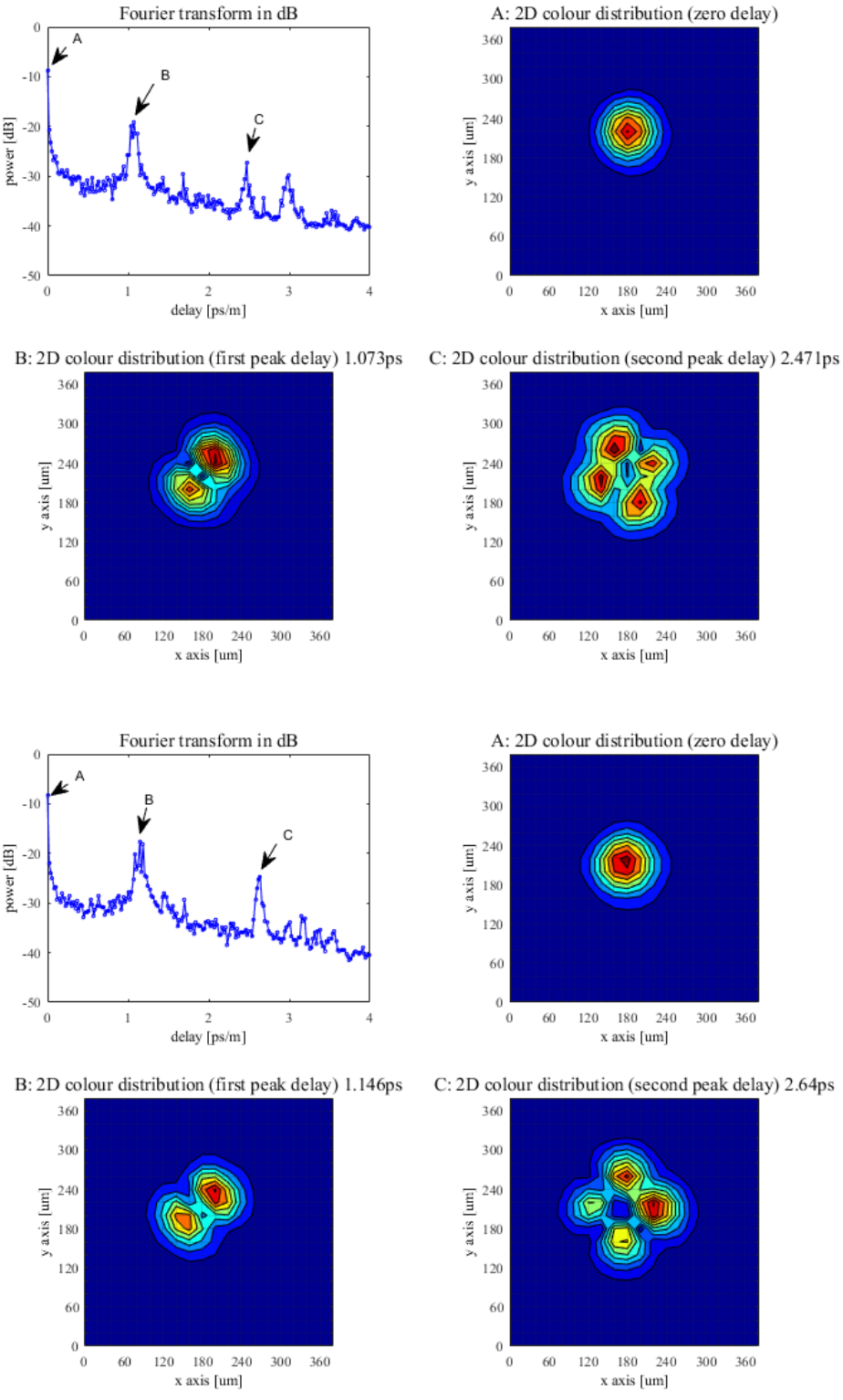

Fig. 4-8 the delay time of each peak measuring in two different wavelength ranges: 1040-1050 nm (above) and 1075-1085 nm (below).

Using this experimental setup, the mode properties of the fibre can be examined while it is bent. The results are shown in Fig. 4-9. It is obvious that there are two peaks in each plot. The changes of these peak represent changes in the power proportion of each mode. We have determined that the first peak is LP_{11} and the second one is LP_{21}. When the fibre is naturally straight, the two modes peaks are nearly at the same height. After bending at a diameter of 105 mm, the LP_{11} mode has more power than in the first plot. Interestingly, the power of the LP_{11} becomes even higher when the bending diameter is decreased. On the other hand, the LP_{21} mode starts to lose power and even at 56 mm the LP_{21} power is low. However, at 32 mm bend diameter the power for both the LP_{11} and the LP_{21} is very low. Therefore, the mode properties can be described as follows: when the fibre starts to bend, the power in higher order modes is transferred to lower order modes. However, below a bending limit the power decreases for all higher order modes.

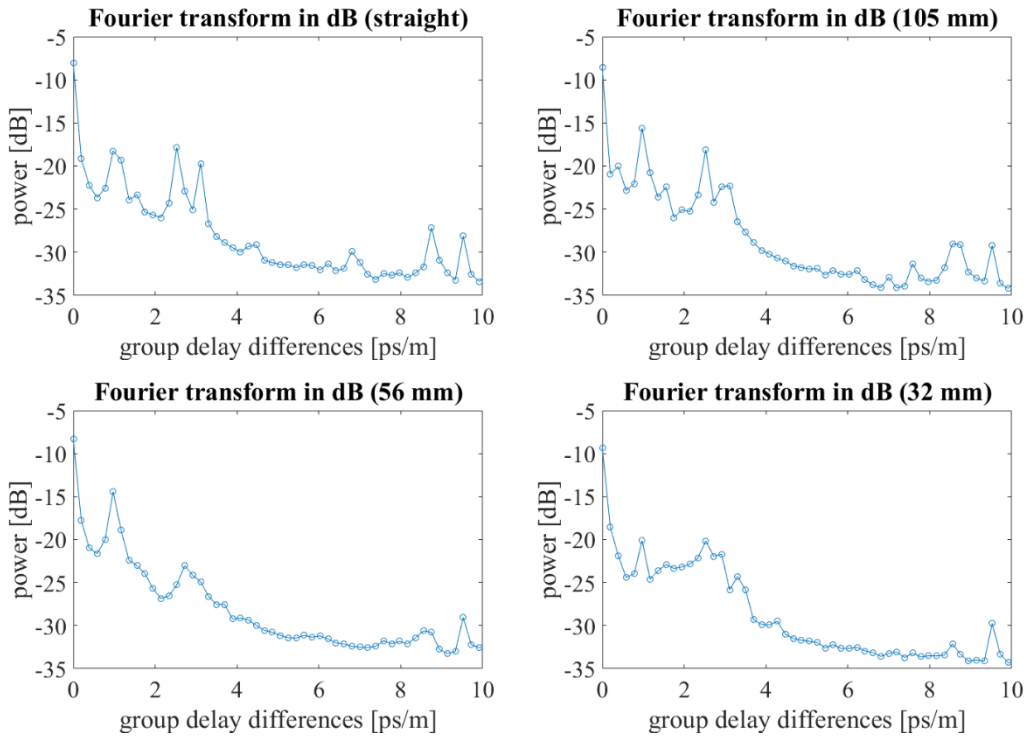

Fig. 4-9 The Fourier transform from 2 m fibre when bent in different diameters: naturally straight, 105 mm, 56 mm, 32 mm.

However, errors cannot be neglected when using this versatile method to calculate the MPI value [141].

Firstly, multiple reflections from optical elements should be taken into consideration. For instance, if a lens is inserted into the optical path, a fraction of the beam will undergo a weak double reflection on the dielectric surface and that will produce very weak multiple double reflections. These weak reflections can be ignored while the first double reflection cannot. The first double reflection, which acts as a "virtual HOM", propagates parallel to the original beam. However, since the induced error of the MPI can and should be subtracted, its power and delay can be easily calculated by Fresnel and Snell Equations. The angle of the incident light is relevant and the power is very sensitive to small angle deviations, making it difficult to measure in practice.

Secondly, errors can also be introduced by the S^2 algorithm sampling. Among all types of Fourier transform available, the most widely used is Fast Fourier Transform (FFT) which is easily calculated using MatLab. The samples should be equally spaced in frequency domain as required by the FFT. The OSA we use can only measure in equally spaced wavelength data points, rather than in frequency. Therefore, a conversion of equally spaced data in wavelength to equally spaced frequency is needed. A polynomial spline interpolation is used to resample it effectively, as it is easy to realize.

Besides this, Fourier transform based systems are known to suffer another effect named spectral leakage can introduce additional error. It occurs when the samples are not enough to cover an integer wave. When the parameters of the sampling in OSA are optimized as discussed in the previous paragraph, the error can be reduced.

In addition, in order to plot a clear and accurate figure of the modes' patterns, the probe array need to be refined. At present, the image we get is 380×380μm large containing 20×20 points. The distance between each point is 20 μm, while the core diameter of the probe is only 4 μm. If we insert more points into the array, more details can be seen and a more real image can be achieved. However, due to the limit on the OSA measuring time, 400 points takes 1.5 hours. If we increase the array to 30×30 points, it will take more than 3 hours to finish, which means the light source may become unstable.

4.2 Single mode performance in HCFs

4.2.1 Background of the Mode coupling in HCFs

Hollow core fibres trap the light in the core with the confinement mechanism called 'ARROW' guidance (details are given in section 3.1.2). In fact, unlike solid core fibre, no mode cut-off condition occurs in the hollow core fibres so all the modes can be transmitted in the hollow core with different attenuations. Suppression of high order mode transmission in short length of HCF is challenging. High order mode transmission in the HCF degrades the beam quality and limits the applications of the fibre.

The basic idea to get rid of higher order modes is based on coupling between the high order modes in the core and the fundamental mode of the cladding. The theory was firstly applied to explain the mode transmission in photonic bandgap hollow core fibres with one main core and two shunt cores embedded in the cladding [44, 142] and then phase matching to optimize the single mode guidance [45].

Anti-resonant hollow core fibres with negative curvature cladding have simple and flexible cladding designs for high order modes suppression. Some designs with a layer of cladding were systematically studied in theory and simulations [28]. Later, the higher order modes were simulated and found to be supressed by tuning the thickness of the cladding in negative curvature hollow core fibres [46]. Then the number of capillaries in the cladding was theoretically studied and 6-capillary HCF was predicted to be optimal for broad band single mode guidance [47]. They also experimentally demonstrated this kind of fibre with single mode transmission but the loss was 0.18 dB/m at 1.6 μm which was not low enough for many applications [47]. HCF with 7 non-touching capillaries was also numerically and experimentally demonstrated to have a minimum loss of 30 dB/km at 1090 nm which was suitable for beam delivery [49]. The suppression of the LP_{11} mode and other higher order modes was achieved only by bending the fibre because the core size of the fabricated fibre was different from the designed one and the LP_{11} mode was not coupled out into the cladding without bending [49]. Recently a similar hollow core fibre with 7 capillaries was reported with an octave spanning bandwidth and a minimum

attenuation of 25 dB/km at 1200 nm [143]. In this paper, a S^2 imaging measurement was applied to analyse the modes transmission in 3 m and 100 m fibres, indicating that a long piece of fibre had good single mode performance [143]. Our work also reported single mode transmission in a 7-capillary negative curvature HCF [50].

The challenge of fundamental mode confinement is in finely tuning the cladding structure for phase matching between the core high order modes and cladding modes not only in design but also in the fabrication process. In fact, higher order modes (except the LP_{11} mode) are intrinsically difficult to excite and have much higher attenuation rate. To strip the LP_{11} mode is of particular importance. In my thesis, two different fibre designs are demonstrated and compared in terms of their transmission loss and single mode performance. An S^2 imaging experiment is used to confirm good single mode transmission in 7-capillary negative curvature hollow core fibre.

4.2.2 Fibre design and fabrication

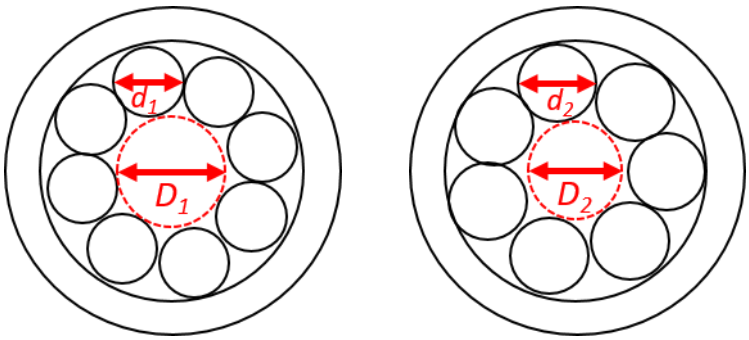

Fig. 4-10 Schematics of the 8-capillary (left) and 7-capillary (right) hollow core fibre design.

Fig. 4-10 is the generic models to explain the principle of single-mode design.

The basic idea behind the design is to achieve phase-matching only between unwanted higher-order modes and cladding modes without disrupting the fundamental core mode. Marcatili's formula [12] is used to calculate the effective refractive index of different modes:

$$n_{eff} = 1 - \frac{1}{2}\left(\frac{V_{vm}\lambda}{2\pi r}\right)^2 \qquad \text{Equ. 4-14}$$

in which λ is the wavelength, r is the radius of core, V_{vm} is the mth zero root of first kind of Bessel function of (v-1) order.

In a traditional design of AR-HCF, 8 capillaries form the cladding. Higher-order modes, especially the LP_{11} mode are commonly found even in a long length of fibre. When we change the number of the capillaries from 8 to 7, the core diameter becomes smaller while the capillary diameter becomes bigger as $\frac{d_1}{D_1} < \frac{d_2}{D_2}$. In this case, the cladding mode effective indices rise up closer to the core higher-modes. In this case, the higher-order modes would experience even higher loss by coupling to cladding modes. After a short distance of transmission, the power of higher-order modes quickly dissipates leaving only the fundamental mode in the core.

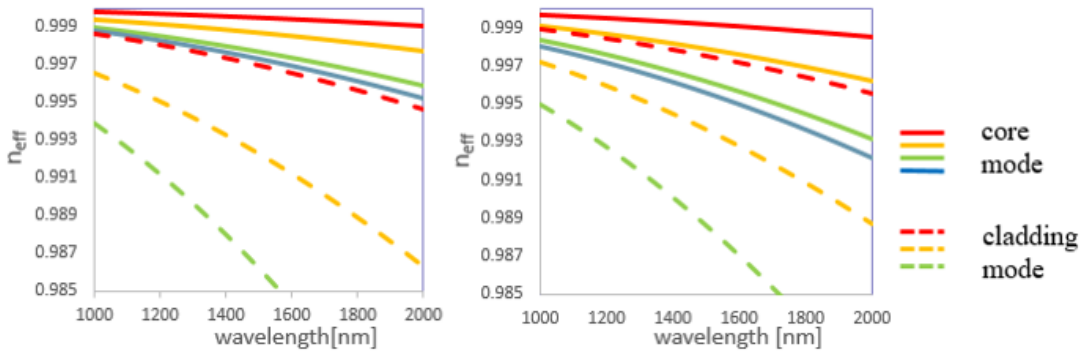

Fig. 4-11 Numerically simulated refractive indices of the core and cladding modes in HCFs with 8 capillaries (left) and 7 capillaries (right); the models are same as in Fig. 4-10.

Fig. 4-11 is the numerical simulation of the core and cladding modes in the HCFs with 8 capillaries and 7 capillaries at a wavelength range from 1000 nm to 2000 nm. The dashed lines are the cladding modes refractive indices which are intrinsically smaller than the core modes' solid lines according to Equ. 4-14. As the cladding area becomes larger (from 8 to 7 capillaries), the cladding effective indices increases. The first dashed line which presents the LP_{01} mode in the cladding becomes higher and gets close to the LP_{11} core mode's refractive index. In this case, the LP_{11} core mode becomes much easier to couple into the cladding and leaked away from the fibre. In this way, all the high order core modes in the 7-capillary HCF dissipate simply from the core.

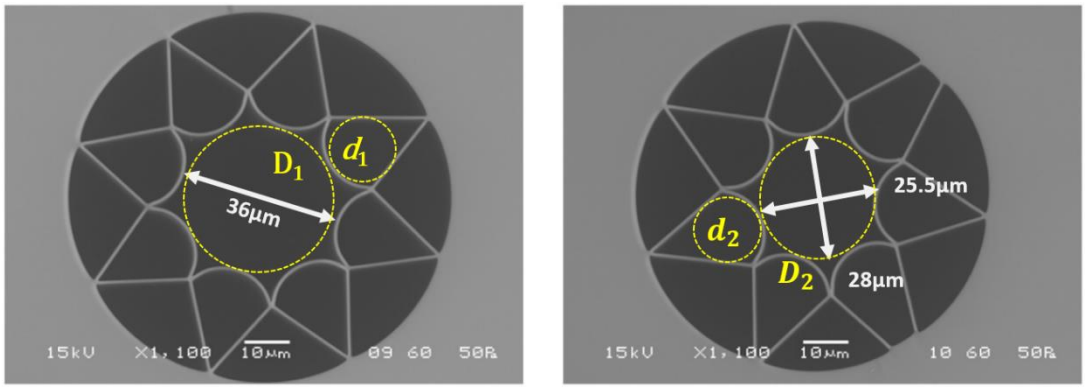

Fig. 4-12 SEM of fabricated hollow core fibres with 8 capillaries (left) and 7 capillaries (right). These two fibres transmit at 1 µm. Left: 8-capillary HCF design with an inscribed dimeter D_1 of 36 µm. Right: 7-capillary HCF design with long and short axes of 28 µm and 25.5 µm.

To demonstrate the single mode guidance design, we fabricated two AR-HCFs, one with 8 capillaries in cladding and the other with 7 (SEM pictures are shown in Fig. 4-12). Two fibres were drawn in a similar fashion to that described in chapter 2. The final fibres have the d/D ratio: 0.41 for the 8 capillary fibre and 0.58 for the 7-capillary fibre.

The transmission properties of the 8-capillary HCF are introduced in Chapter 2. The attenuation is 0.07 dB/m at a wavelength of 1155 nm, found using a cutback measurement. As for the 7-capillary HCF, the same cutback measurement was taken with the fibre cut from 45 m to 10 m. The fibre attenuation is as low as 0.025 dB/m at around 1064 nm which is similar to the previous report of lowest attenuation of 0.026 dB/m at 1041 nm in 8-capillary HCF [35]. The attenuations of two fibres used in the experiment are presented in Fig. 4-13.

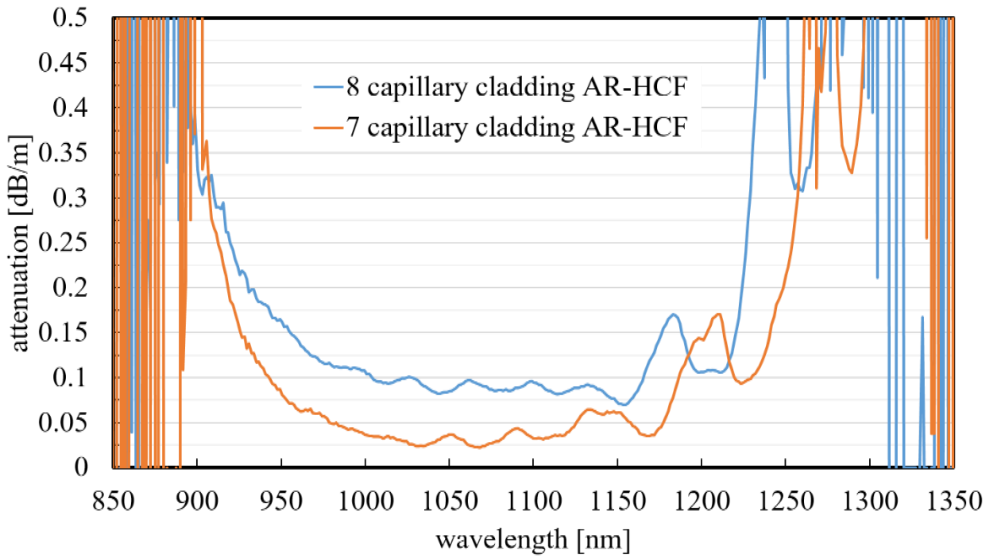

Fig. 4-13 Fibre attenuations measured by cutback measurement of 8-capillary HCF and 7-capillary HCF [50].

4.2.3 Near field images detected by CCD camera

To demonstrate the mode property in the HCF, near field images of two HCFs are obtained by a CCD camera. First, a supercontinuum is used as the light source. A single mode fibre with a cut-off wavelength of 630 nm is employed to butt-couple to the input end of the HCF under test. The transverse position of the single mode fibre is controlled by an X-Y stage and is scanned across the core diameter of the HCFs in steps of 5 μm. A 10 nm bandpass filter centred at 1050 nm is used before the CCD camera.

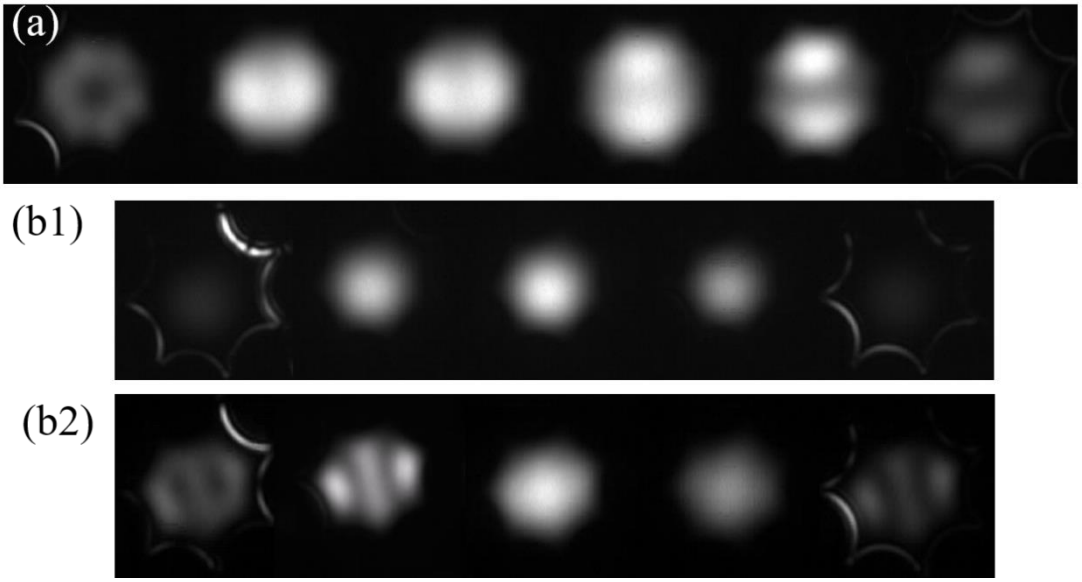

Fig. 4-14 Near filed images of the fibre output end under a 1D input scan with a spatial step of 5 μm: (a) 11.5 m 8-capillary HCF; (b1) 11.3 m 7-capillary HCF; (b2) 1.02 m 7-capillary HCF [50].

Fig. 4-14 (a) shows the mode transmission property of 8-capillary HCF. Firstly, the single mode fibre is butt coupled to the cladding of the HCF and higher order modes are excited. The first pattern is LP_{31}-like. As the single mode fibre output end moves from the cladding of the HCF to the centre of the core, higher order modes (LP_{31} mode) are eliminated and the LP_{11} mode is identified. When the single mode end is aligned to the centre of hollow core in HCF, the near field patterns are almost those of a LP_{11} mode with different polarizations. When the single mode fibre output end moves away from the centre of the hollow core, higher order modes are excited again.

Comparing 7-capillary HCF with a similar length of 11.3 m shown in Fig. 4-14 (b1), the misalignment of single mode fibre and HCF only causes a change in intensity of the LP_{01} mode rather than the different higher order modes excitation. The LP_{21} mode is observed in Fig. 4-14 (b2) with only a 1.02 m length of the 7-capillary HCF. In fact, 7-capillary HCFs with a length of less than 3 m transmit high order modes which can be detected by camera. By applying the offset butt-coupling, the LP_{21} mode with 2 dB/m attenuation at 1064 nm is confirmed by cutback measurement, which is nearly 100 times greater than the attenuation measured for the

LP_{01} mode. During the measurement of 7-capillary HCF, there is no evidence of LP_{11} mode even with a short piece of the HCF.

4.2.4 Demonstration of single mode guidance by S^2 measurement

S^2 imaging measurement for HCF is introduced in chapter 4.1 which will be adopted in this section to confirm the mode contents of HCFs. The experiment setup is exactly same as in Fig. 4-3. The fibres under test are 11.5 m of 8-capillary HCF and 11.3 m of 7-capillary HCF introduced in the previous section. The measured spectral window ranges from 1078 nm to 1082 nm.

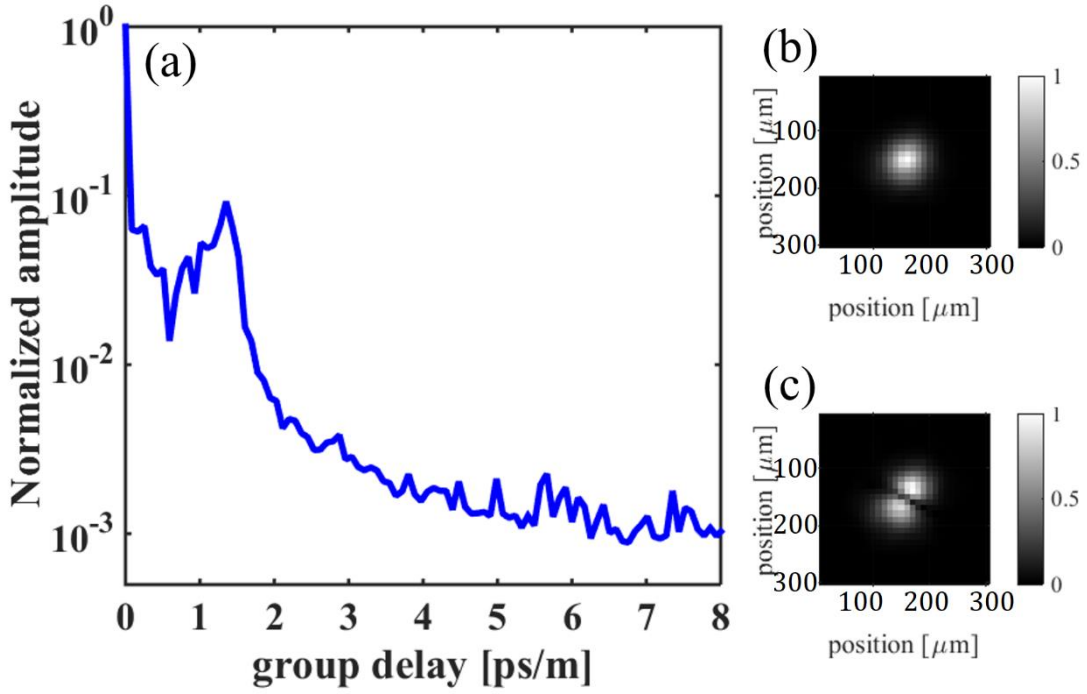

Fig. 4-15 (a) S^2 measurement result of 11.5 m 8-capillary HCF: different modes normalized amplitude as a ratio of their group delay; (b) the constructed mode profile at zero delay position; (c) the constructed mode profile at first group delay peak of 1.352 ps/m [50].

Fig. 4-15 shows the S^2 measurement results of 11.5 m 8-capillary HCF. The fibre under test is rewound in circles over 1 m in diameter on the optical bench to get rid of extra bending loss. At zero delay position, the reconstructed mode profile (shown in Fig. 4-15 (b)) is all the modes together. Since the fundamental mode has the largest proportion of the total power in the optimized excitation fashion, the mode profile looks like the LP_{01} mode. At 1.352 ps/m mode group delay, a significant peak

indicates a high order mode that is found to be the LP_{11} mode in the reconstructed modal intensity pattern. This time delay is caused by the modal interference between LP_{01} mode and LP_{11} mode.

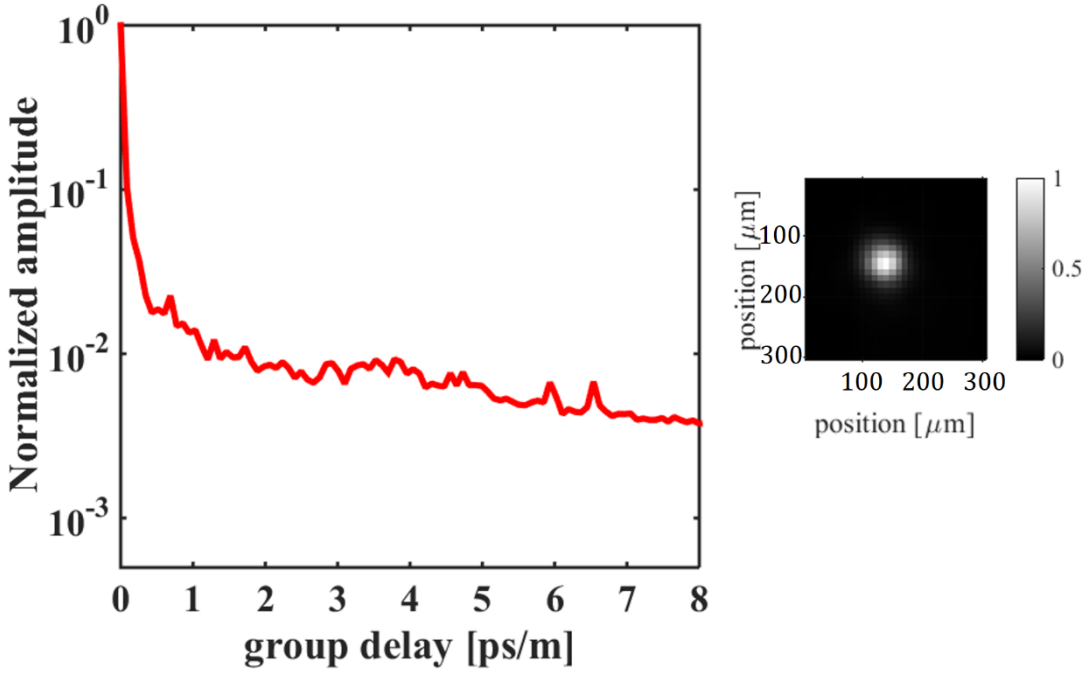

Fig. 4-16 S^2 measurement result of 11.3 m 7-capillary HCF with the constructed mode profile at zero group delay position [50].

7-capillary HCF with a similar length of 11.3 m and optimised excitation is measured in the same condition as the 8-capillary HCF. S^2 measurement results are shown in Fig. 4-16. The only reconstructed mode profile is found at zero group delay position. It looks like the LP_{01} mode as the beam contains a large portion of fundamental mode. However, there is no significant peak at all in the S^2 measurement. No modal interference between LP_{11} mode and LP_{01} mode is present. At a group delay of around 6 ps/m, there are two small peaks indicating the LP_{21} mode of two polarizations as predicted by Equ.4-14. The mode intensity is too weak to reconstruct the identified patterns. Single mode performance is confirmed at different wavelengths (990-994 nm, 1078-1082 nm and 1150-1154 nm). As mentioned in the previous section, S^2 measurements cannot be used with arbitrary fibre lengths: peak details with low resolution are easily lost in fibres of short length.

Based on the S^2 measurement results, similar 7-capillary HCF for other short wavelengths were drawn [50]. The minimum attenuations of these fibres are lower

than any previously reported in their spectral windows [56]. Near field patterns are collected to confirm single mode performance in all fibres.

4.3 Conclusion

In this chapter, S^2 imaging measurements are introduced in detail to present the modes in the HCF. Single mode transmission principles are investigated in theory and experimentally. In the experiment, HCFs with different lengths are measured. It is found that the fibre length cannot be either short or long. Fibres as short as 2 m will miss some information of the mode contents while fibres longer than 19 m will have some misleading information of the mode because of the resolution limitation in the OSA.

By comparing the mode guidance in 8-capillary and 7-capillary HCF, 7-capillary HCF demonstrates better performance in single mode transmission with lower attenuation. The LP_{21} mode in a short piece of fibre shows an attenuation of 2 dB/m through the fibre. The LP_{11} mode is free in this kind of HCF. Thus, 7-capillary HCF is an important improvement in HCF for mode control.

CHAPTER 5 MID-INFRARED GAS FILLED FIBRE LASERS

In this chapter, the development of the gas filled mid-infrared fibre lasers are introduced in details in section 5.1. In section 5.2, a ring cavity based gas filled fibre lasers is demonstrated and the output results are presented. Section 5.3 demonstrates the laser setup with single pass ASE configuration. An output spectrum and the output power along the increasing incident power is presented. Another experiment of pump absorption is shown in section 5.4 as a fibre side scattering measurement. Then the optimization of the laser with the highest output power is presented in section 5.5.

5.1 Introduction of acetylene filled fibre lasers

The advantages of the gas fibre lasers have been introduced in Chapter 1. The acetylene filled fibre lasers generate the emission in the mid-infrared region. They have been demonstrated in both pulsed regime [66, 67, 88] and the CW regime [59].

5.1.1 The pulsed lasers

In 2010, mid-IR laser emission from a C_2H_2 filled hollow core photonic crystal fibre was reported for the first time [144]. From then on, pulsed gas fibre laser has been studied based on population inversion [145]. Both C_2H_2 and HCN were studied as the gain media in the mid-IR gas fibre lasers. Since they have similar molecule structures and energy levels, their absorption region is at 1.53 μm and lasing region is at 3.1 μm [65]. Both of them are commonly demonstrated pumped by an OPA/OPO [88]. Recently, by pumping with a narrow-bandwidth OPA at 1.53 μm, 1.4 μJ pulse energy at 3 μm was obtained in a 10 m long acetylene-filled AR-HCF of single-pass configuration. A constant 20 % slope efficiency was observed unaffected

by the acetylene pressure which could be explained by the balance of increased molecule density and reduced lifetime of laser upper level when pulsed pump entering the transit regime. M^2 factor of the output beam was measured as low as 1.2.

Another efficient mid-IR acetylene filled fibre laser emission has been reported with a bespoke amplified, modulated, narrowband, tunable 1.5 μm diode laser in 2014 [66]. A maximum power conversion efficiency of 30 % was achieved with a 10.5 m gain fibre at 0.7 mbar. A pump laser energy threshold is below 50 nJ and the maximum efficiency is 20 % as a function of the total incident power.

In 2016 the acetylene filled fibre pulsed laser based on a ring cavity configuration was demonstrated [67]. A 100 m feedback fibre with low loss of 0.025 dB/m over the laser wavelength band was used to form the cavity. Using an average pump power of <100 mW and synchronous pumping at a repetition rate of 2.6 MHz, a maximum output power with a slope efficiency of 8.8 % was achieved at a 0.3 mbar pressure.

5.1.2 The continuous-wave lasers

The acetylene filled fibre lasers was difficult in working in the continuous-wave (CW) regime. First, the acetylene fibre laser was difficult to be self-terminated in CW operation because acetylene laser was not able to effectively depopulate the laser lower level due to its lack of rapid radiative relaxation routes. Another reason was that stimulated Brillouin scattering limits the high power fibre amplifier for narrow linewidth sources. However, the acetylene filled fibre lasers with continuous-wave (CW) operation was first demonstrated in the ring cavity [67]. With a 3 m feedback fibre, the output mid-infrared power reached more than 2.5 mW at a maximum incident pump power of 75 mW, corresponding to a slope efficiency of 6.7 %. This system provides a high beam quality of the laser output and the excellent stability of the laser over long time. There is no more paper reporting the CW gas filled hollow core fibre lasers.

My research is to build a CW gas filled fibre laser in both ring cavity and single pass ASE configuration [59]. To further increase the output power, I use a high

power pump source of 10 W output at 1530 nm. I achieve over 1 W of output laser power which is 400 times larger than the previous report. The slope efficiency is over 30% in single pass ASE configuration. Details are provided in the following sections.

5.2 Continuous-wave Laser in the Ring-Cavity Configuration

The research focuses on the high power continuous wave acetylene filled fibre lasers. By investigating and comparing ring cavity configuration and single pass ASE configuration, we find that the laser with high incident power favours the single pass ASE configuration.

5.2.1 Experimental setup

1) Experiment configuration

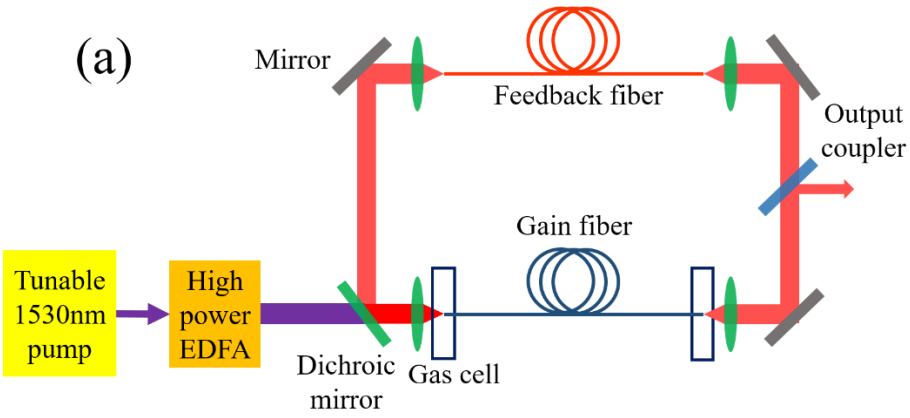

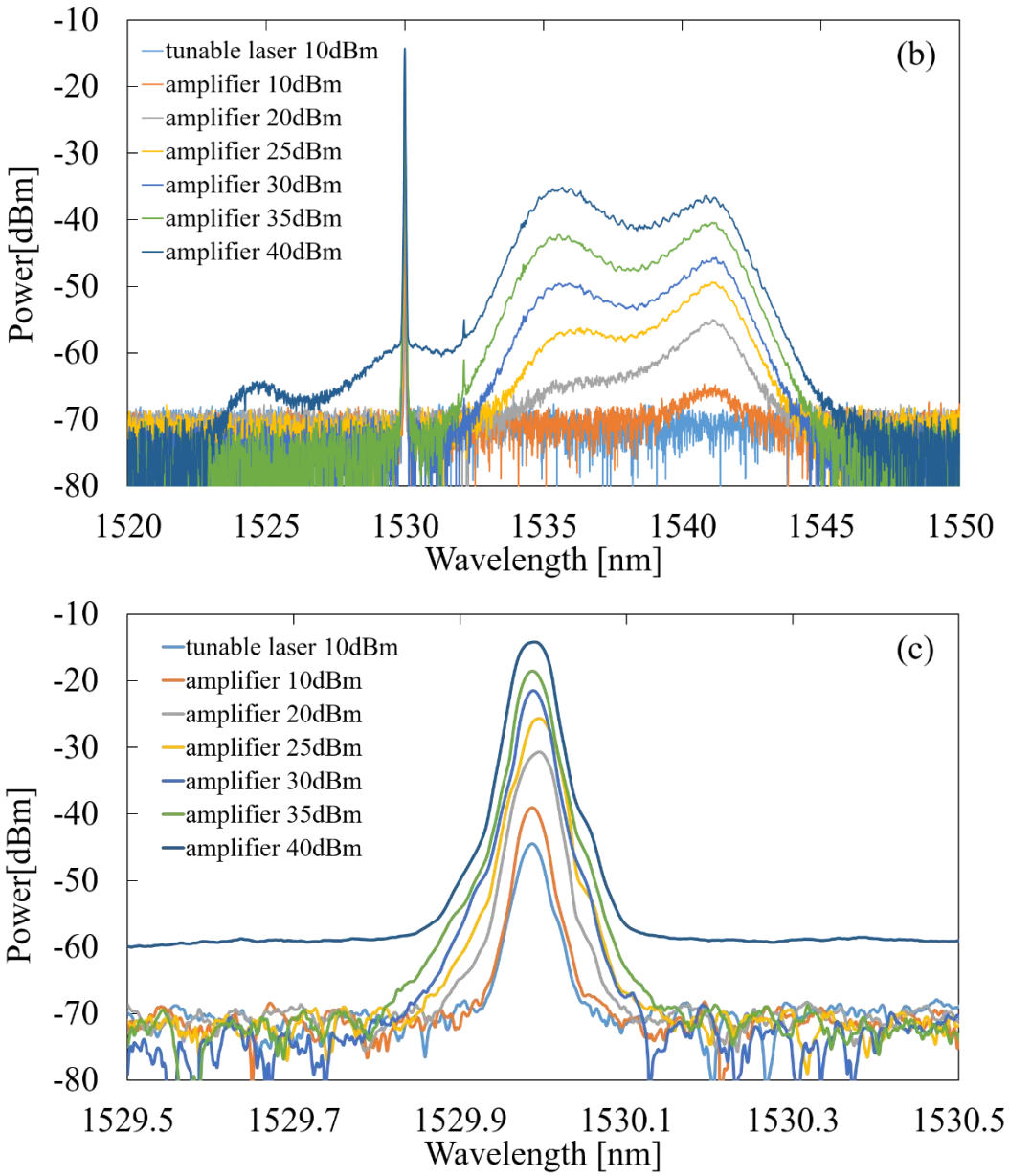

Fig. 5-1 (a) Experiment setup of the laser cavity. (b) Tunable laser and EDFA output spectrum with different output power on resonant wavelength (1530.385 nm). (c) Details at the on resonant wavelength.

We focus first on the CW lasers based on the ring cavity configuration formed by a feedback fibre (Fig. 5-1 (a)). Acetylene is pumped by a tunable distributed feedback diode laser (ID Photonics GMBH, CoBrite DX1, linewidth <100 kHz, maximum output power 16 dBm) seeded CW Erbium-doped fibre amplifier (EDFA, Bktel Photonics, HPOA-S370ac). An optical coupler (AC Photonics, SA15100202A1022, Splitting Ratio: 90: 10) and an isolator (Thorlabs, IO-H-

1550FC) are employed between the diode laser and the amplifier to monitor the input power and get rid of the backward power. Wavelength tuning is achieved with the standard temperature and current stabilisation of the build-in laser driver. Specific software is used to control the tunable laser and the EDFA. This customized EDFA has a maximum output of 40 dBm in specification and 9.6 W in practice. The pump is tuned to acetylene absorption line P (9) at 1530.385 nm. Fig. 5-1 (b) displays the spectra measured by a single mode fibre and analysed by an optical spectrum analyser (OSA, YOKOGAWA AQ6370) at the output of the tunable laser and EDFA with its different output power at on resonant wavelength. When raising the pump power, a strong and increasing ASE spectrum is observed. The peak details at on resonant wavelength are presented in Fig. 5-1 (c). The power of tunable laser with 10 dBm is lower than it of the amplifier with 10 dBm because of the different coupling by a single mode fibre. As for the amplifier, the line width increases to a maximum when the power is 40 dBm. At the same time, the ASE power increases as well and finally becomes nearly half of the total power as shown in Fig. 5-1 (b).

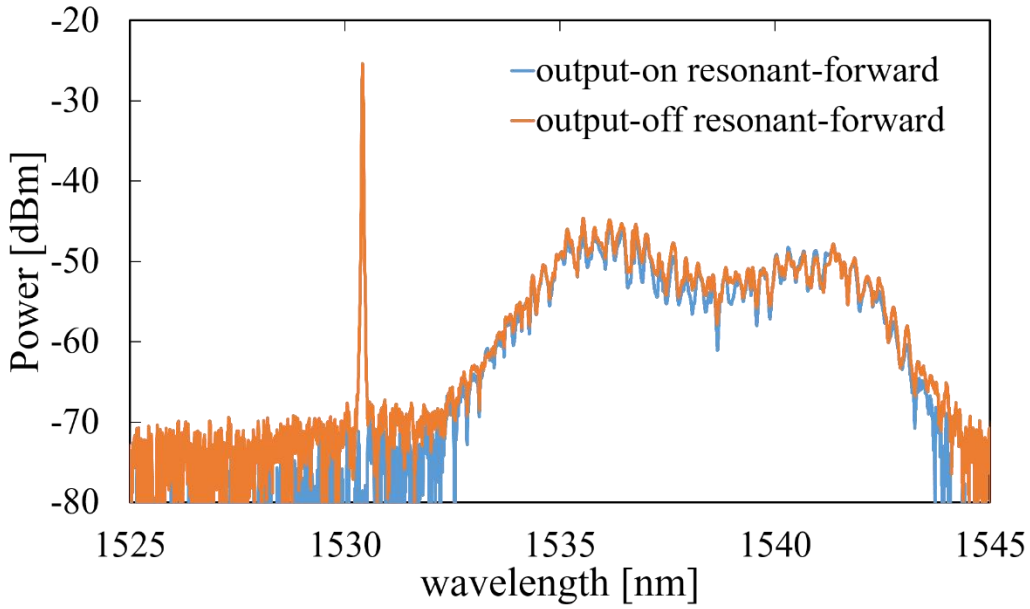

Fig. 5-2 Measured on and off resonant output power through the acetylene filled hollow core fibre at a wavelength range from 1520 nm to 1545 nm.

The output spectra at pumping wavelength through the acetylene filled fibre are shown in Fig. 5-2. The off resonant spectrum is same as the amplifier's output spectrum shown in Fig. 5-1. However, the on resonant spectrum has on peak at the

acetylene absorbing wavelength indicating that the power at this wavelength has already been absorbed. The two ASE spectra are same and don't change at all. By integrating calculation, the on resonant peak power is 50% of the total pump power. In this case, the maximum absorbed power is up to 4.8 W (half of 9.6 W). The ASE power occupies half of the total power but makes no contribution to acetylene absorbing. In this thesis, the slope efficiency is defined as the ratio of the output lasing power at 3.1 um to the absorbed pump power.

A dichroic mirror (94 % transmission at 1.53 μm and 99 % reflection at 3.1 μm) is used to combine the feedback power and the pump power before coupling into the gain fibre through a coated CaF2 lens (50 mm focus length, 98 % transmission at 1.53 μm) and a gas cell window (3mm thick uncoated sapphire, 88 % transmission at 1.53 μm). Two fibre ends are sealed in vacuum gas cells that can be filled with acetylene gas to require pressures (0.1 mbar-13 mbar). It takes a few hours to reach the gas equilibrium through the entire fibre.

With the ring cavity configuration, several mirrors are used to reflect light and make up a round trip route with the feedback fibre. Light passes through the gain medium in the ring cavity and is amplified each time. An output coupler with 70 % output coupling efficiency is used as the output.

2) Hollow core fibres for gain and feedback

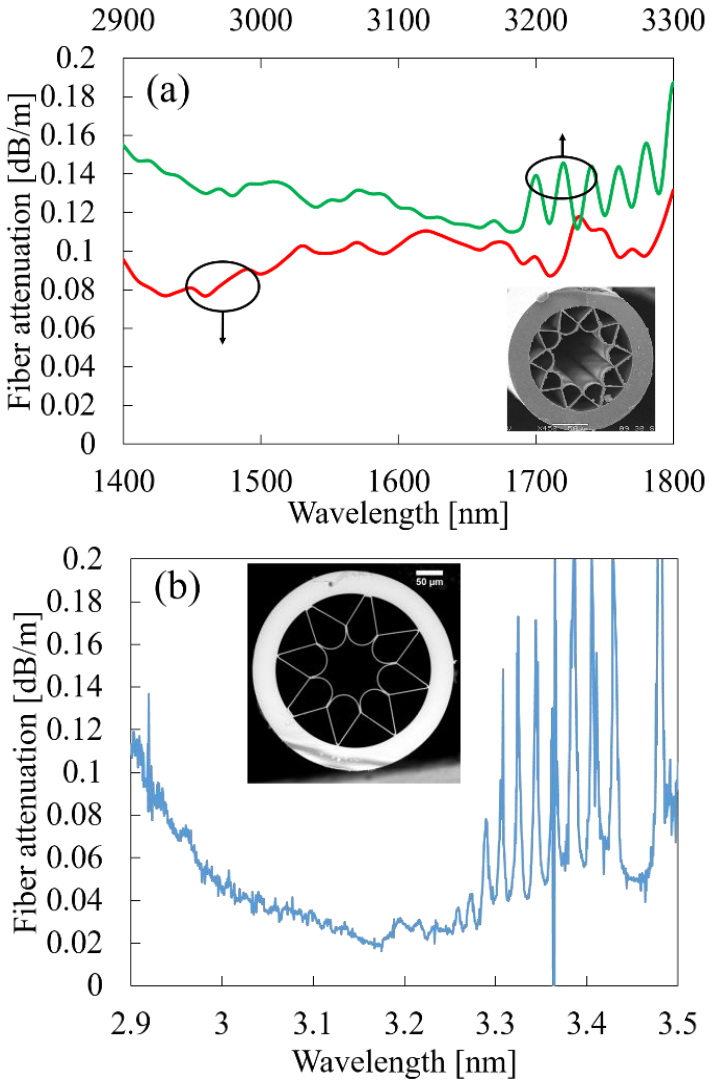

Fig. 5-3 (a) Attenuation curve for the gain fibre at both pumping and lasing wavelengths. Inset: SEM of the gain fibre cross section. (b) Attenuation curve for the feedback fibre. Inset: SEM of the feedback fibre cross section [59].

A 31m gain fibre is designed for both pump and laser wavelengths (shown in Fig. 5-3 (a)). This AR-HCF contains 10 capillaries in its cladding with a core diameter of 75 µm and an outer diameter of 202 µm. Cut-back measurement is used to measure the transmission loss by using an OSA and a monochrometer (Bentham TMc300). The attenuation of the empty gain fibre is 0.1 dB/m at the pump wavelength of 1.53 µm and 0.12 dB/m at the laser wavelength of 3.1 µm. The feedback fibre has 8 ice-cream shaped capillaries in the cladding. In Fig. 5-3 (b), the attenuation of ~0.025 dB/m is shown over the laser wavelength band. A short piece (3 m) of the feedback fibre can provide low loss in laser delivery.

3) Alignment

In this setup, initial alignment at each fibre end is assisted by a HeNe laser (Thorlabs H339P2, average power ~ 2 mW) at 3.39 μm as a reference laser [146]. Fig. 5-4 shows two directions of the alignment. The experimental setup shown in Fig. 5-4 (a) displays the coupling route from feedback fibre to gain fibre with a coupling efficiency of 20%. However, even though the feedback fibre and the gain fibre have similar parameters, the transmission properties are different due to different mode properties. The coupling efficiency from the gain fibre to the feedback fibre (in Fig. 5-4 (b)) is 80 %. The coupling efficiency at lasing wavelength is different from it at pumping wavelength. When adjusting the coupling from the amplifier to the gain fibre at pumping wavelength of 1.53 μm, the coupling efficiency is over 80 %.When the beam is coupled into each fibre end, improving and balancing coupling efficiencies at both pumping and lasing wavelengths is challenging. Thus, the aim to balance the coupling efficiency is to ensure the highest output power.

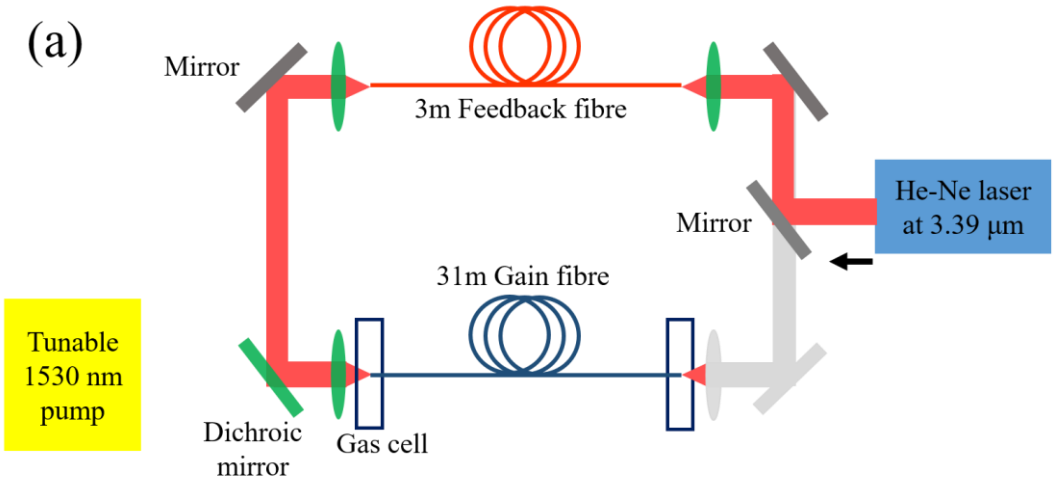

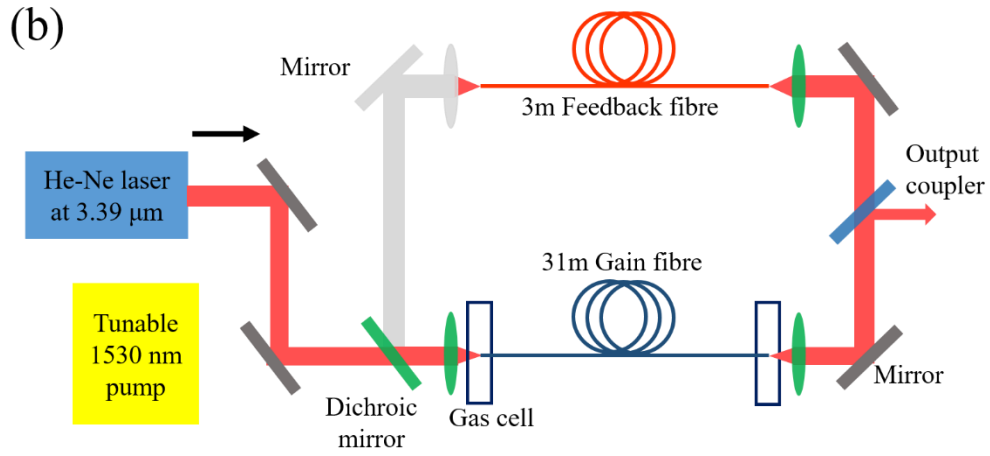

Fig. 5-4 alignment process with a He-Ne laser at 3.39 μm as a reference: (a) laser beam from feedback fibre to gain fibre; (b) laser beam from gain fibre to feedback fibre

4) Gas cell

Two gas cells are important components in the setup. It has four key functions including sealing the gain fibre ends, vacuuming the gain fibre, filling the gas into the gain fibre and monitoring the pressure of the gas cell. The gas cell is shown as Fig. 5-5. It was designed and built for the previous gas fibre laser research and it is still suitable for my research.

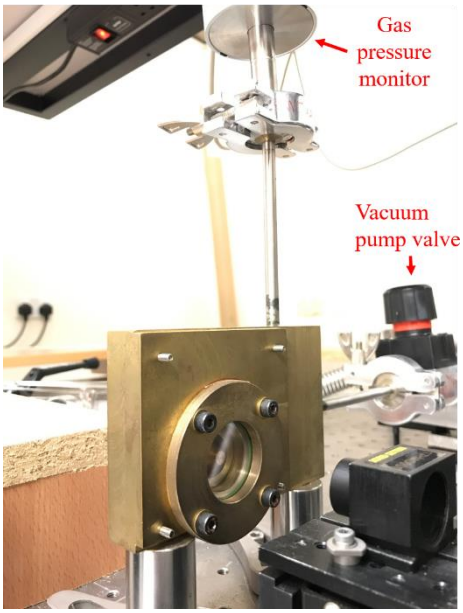

Fig. 5-5 A gas cell which is used to seal the fibre end.

Fig. 5-5 is the photo of one gas cell. This gas cell is employed to seal the output fibre end. It is connected to the vacuum pump via the tube and a controlling valve. It is convenient to remove the gas from the gas cell and the hollow core fibre. On the top of the gas cell there is a pressure monitor which shows the real-time pressure inside the gas cell. The range of the monitor is up to 13 mbar. The accuracy is 1e-4 mbar. A window (3mm thickness, 88% transmission at 1.53 μm) is tightly fixed on one side of the gas cell. On the other side, the fibre is first sealed in a metal tube with a rubber ring. Then this metal tube is fixed into the gas cell. The fibre input end is sealed into another gas cell which has a similar configuration with the previous one. The only difference is that this one has another tube connecting to the acetylene tube. These two gas cells are connected by the tube which is also joint to the vacuum pump. By adjusting the valves on the tube, it is easy to fill the acetylene gas into the fibre from one fibre end or both fibre ends.

The leakage rate of the gas cells have to be tested before they were put into use. Firstly the two gas cells are evacuated during the whole night to make sure the fibre is totally vacuumed. Then the valves have to be closed. Nothing else affects the pressure inside the gas cell except the leakage by the gas cell itself. The pressure values on the monitor are recorded by hours. The leakage rate presents velocity of the air going into the fibre. We finally find 8.7e-3 mbar is an acceptable value which is easy to reach. Since the needed acetylene pressure values are from 1e-1 mbar to several mbar, this leakage rate is negligible during a few hours for acetylene filling.

In the experiment, the gas cell is firstly vacuum the fibre and then fill the acetylene gas into it. The laser measurement is taken when the fibre is totally filled with the acetylene gas. The filling time is calculated according to the theory of gas diffusion [147]. The Knudsen number *Kn*, defined as the ratio of the molecular mean free path length to a representative physical length scale, decides the diffusion regime. When $K_n < 0.01$, it represents the Hydrodynamic Flow Regime. When $K_n > 1$, it is Free Molecular Flow Regime.

For acetylene gas,

$$K_n = \frac{\lambda}{a} = 4.4 \qquad \text{Equ. 5-1}$$

in which *a* is the core radius of the fibre (37 μm). λ is the mean free path.

$$\lambda = \frac{K_B T}{\sqrt{2}\pi P \delta^2} \qquad \text{Equ. 5-2}$$

The temperature *T* is 20 °C and the pressure *P* is 0.5 mbar. The δ diameter of the molecule is 3.34e-10 m. So the mean free path λ is 1.63e-4 m.

So for this pressure, it is in the molecular flow regime. For this regime, the filling time and the diffusion coefficient is as follows:

$$t = \frac{(\xi L)^2}{\pi^2 D} \ln\left(\frac{\pi^2}{8} \times \frac{P_0}{P_0 - P}\right) \qquad \text{Equ. 5-3}$$

$$D = \frac{2av}{3} \qquad \text{Equ. 5-4}$$

The mean molecular velocity $v = \sqrt{\frac{8K_B T}{\pi m}} = 486.098\ m/s$. The acetylene mass is 0.026037 kg/mol÷6.02 e23 = 4.33e-26 kg.

Thus, $v = 1.19 \times 10^{-2}\ m^2/s$.

ξ is a geometrical factor depending on the filling conditions. It equals to 2 for gas diffusing from one end and equals to unity for gas diffusing from two ends of the fibre. *L* is the fibre length.

The filling time is defined as the time required for the pressure *P* in the fibre to reach 85% of the equilibrium pressure P_0. So it takes 15 hours to fill the whole fibre (31 m) from one end and 3.75 hours from two ends.

Laser measurements are usually taken after 4 hours gas filling from both ends.

5) Measurement

Measurement results with this ring cavity configuration have been recorded at different pressures. To compare the output power in the ring cavity and single pass ASE configuration, the feedback fibre is blocked to obtain the output power in the single pass ASE configuration without changing anything else. The power meter is placed in front of the output coupler.

5.2.2 Output results

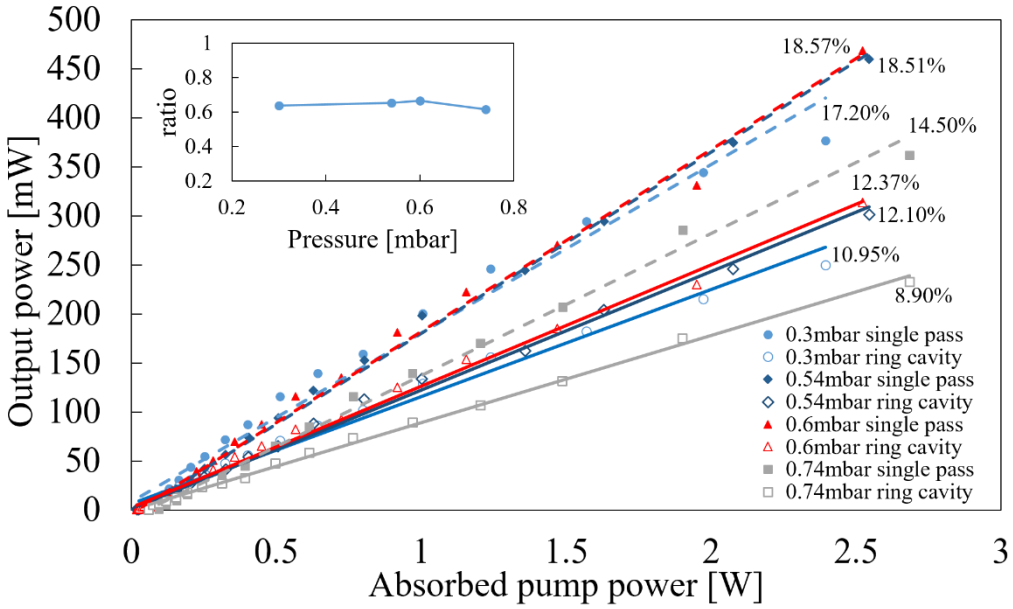

Fig. 5-6 Absorbed pump power- output 3 μm power curve with 31m gain fibre in the ring cavity configuration and single pass configuration at different pressures (0.3 mbar, 0.54 mbar, 0.6 mbar and 0.74 mbar). Inset: the slope efficiency ratio (slope efficiency in ring cavity/ single pass ASE) as a function of the pressure.

Fig. 5-6 compares the output power as a function of the absorbed incident pump power in ring cavity and single pass ASE configuration at different pressures. The output power of the mid-IR is as high as 0.468 W with a slope efficiency of 18.57 % in single pass ASE configuration while the slope efficiency of only 12.37 % is achieved in the ring cavity configuration at the same pressure of 0.6 mbar. It is because the coupling efficiency at each fibre end needs to be balanced for both pumping and lasing wavelengths. Some power is lost due to the low coupling efficiency from the feedback fibre to the gain fibre. In the ring cavity configuration, with 70 % output coupler, residual pump power in the fibre is 0.13 W. The sum of the residual power and the output power in ring cavity configuration is nearly the same as the results in single pass ASE configuration. The inset figure is the slope efficiency ratio of the ring cavity and single pass ASE configurations at a range of 0.3 mbar to 0.74 mbar. The ratio stays between 61 % and 66 % which is consistent with the 70 % reflectivity of output coupler at 3.1 μm. It indicates that the feedback fibre only add an additional source of loss. However, the threshold of the ring cavity

is as low as 18mW at 0.6mbar. Single pass configuration has a threshold of 37 mW in the same condition. Thus the feedback fibre leads to a lower output power but lower threshold in the ring cavity configuration.

In summary, this ring cavity configuration with high incident power is benefit for low threshold rather than achieving a higher output power. In this case, a single pass ASE configuration is in highly demand for high power applications.

5.3 Continuous-wave Laser in the Single Pass ASE Configuration

5.3.1 Experimental setup

A single pass ASE configuration is a priority for the laser system due to its simple setup and higher output power. Without the feedback fibre, it is unnecessary to consider the balance of coupling efficiency at each fibre end. Improving the coupling efficiency at the gain fibre incident end is vital.

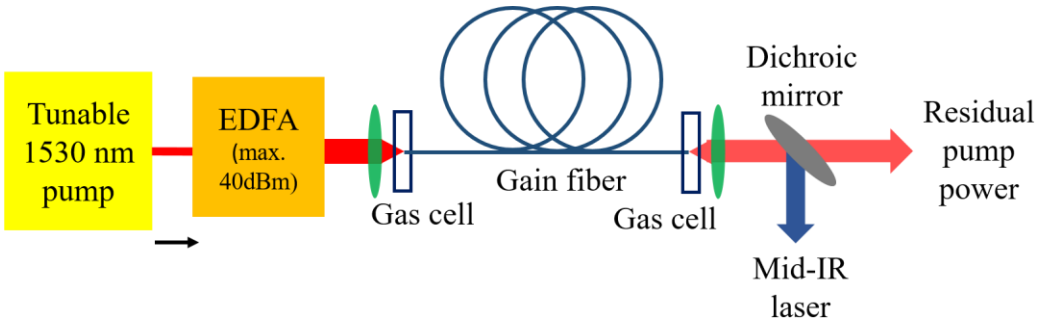

Fig. 5-7 Experiment setup with single pass ASE configuration [51].

A single pass ASE configuration is demonstrated with a high power pump source shown in Fig. 5-7. The tunable laser diode is followed by a CW Erbium-doped fibre amplifier as in section 5.2.1. Pump light is coupled into the AR-HCF through a coated CaF_2 lens and a gas cell window with a coupling efficiency of over 90 %. Both ends of the gain fibre were sealed in gas cells with optical access windows. At the fibre output end, the dichroic mirror is used to separate the residual pump power from the mid-IR laser beam. A thermal power meter (Ophir VEGA) with a range of 30 W is used to measure the output power.

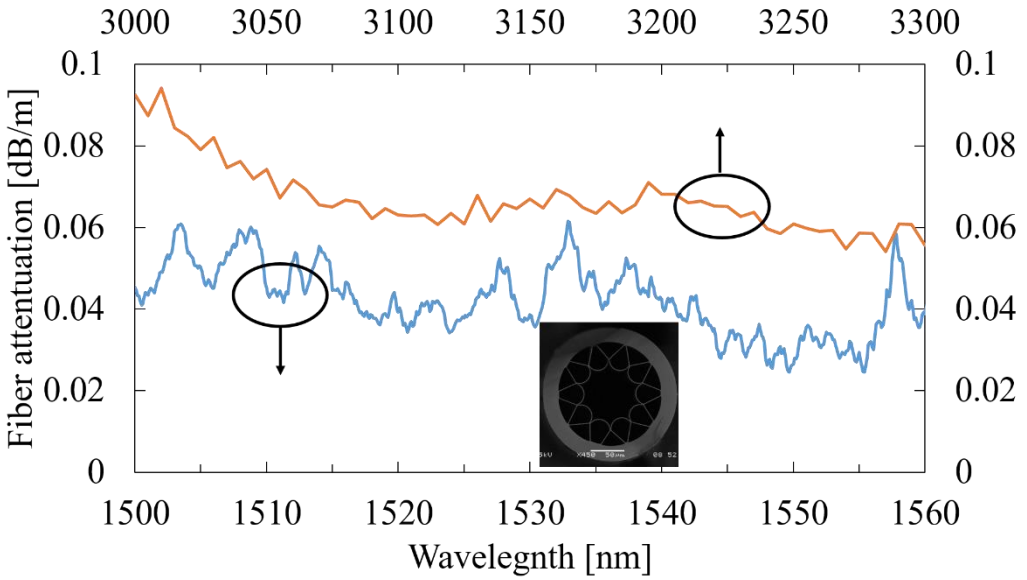

Fig. 5-8 Measured attenuation of the AR-HCF as a function of the wavelength at both pumping and lasing wavelengths. Inset: SEM of the AR-HCF.

The attenuation around the pumping and lasing wavelengths of the gain fibre is shown in Fig. 5-8. A 10-capillary fibre has a core diameter of 75 μm and an outer diameter of 199 μm. The attenuation is measured by the cutback measurement. Firstly, one end of the hollow core fibre is placed closely to a halogen light source directly. The other end is inserted into the slit of the monochrometer. A spectrum ranging from 2.9 μm to 4 μm is recorded. Then the fibre is cut from 148 m to 30 m with keeping the fibre end which is close to the white light source. The transmission spectrum of 30 m fibre is recorded by the monochrometer. The attenuations of 63 dB/km and 69 dB/km at 3.12 μm and 3.16 μm wavelengths are achieved. Another cutback measurement is taken with the rest 118 m fibre. A single mode fibre is employed to transmit the white light and butt couple to the hollow core fibre. The spectrum from 1200 nm to 1700 nm is collected and analysed by an optical spectral analyser. Then this fibre is cut to 30 m and the spectrum is recorded. Then the attenuation at 1.53 μm wavelength is calculated as 37 dB/km. These are the lowest attenuations yet reported for HCF for this application. In fact, the measured coupling efficiency is over 100% with the measured fibre attenuation which indicates the actual attenuation might be somehow lower than the measured values.

This fibre with 6 m, 15 m and 40 m in length is used at different pressures. Results are given in the following sections.

5.3.2 Output spectrum

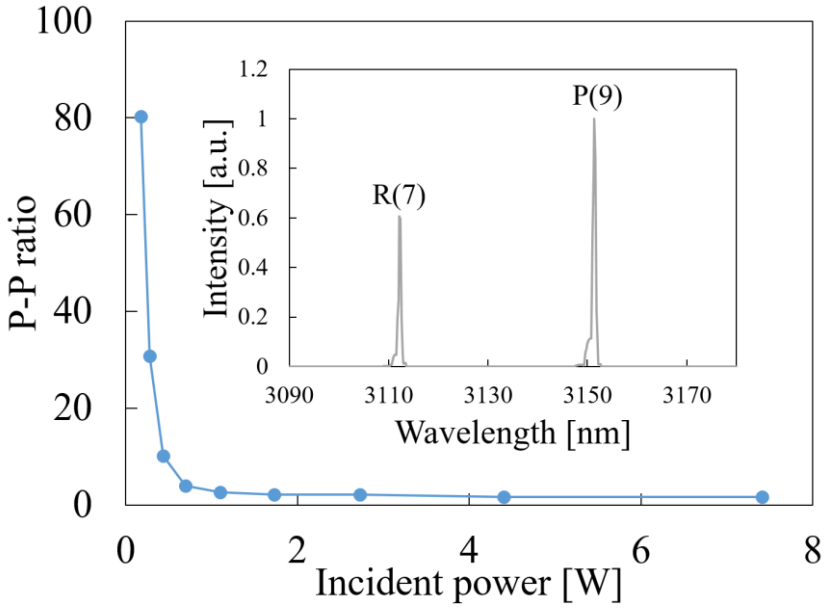

Fig. 5-9 The power ratio (P(9) /R(7)) as a function of the incident power. Inset: measured output optical spectrum at 0.6 mbar pressure, 15 m length with maximum incident power of 9.6 W.

The performance of the laser system was investigated by measuring the output power at various gas pressures with different fibre lengths. First, the output optical spectrum is shown in Fig. 5-9 inset. A short piece (~1 m) of same mid-IR hollow core fibre is used to collect and transmit the light at the output of the laser to a monochrometer (Bentham TMc300) with a resolution of 0.5 nm.

Two lasing emission lines are observed near 3.12 μm and 3.16 μm as the pump is tuned to acetylene on resonance P(9) absorption lines at 1.53 μm. These two lasing lines correspond to the R(7) and P(9) transitions from J = 8 rotational state of v1+v3 vibrational state to J = 7 and J = 9 rotational states of v1 vibrational state in acetylene molecule.

Fig. 5-9 shows that the power ratio of two lasing intensities (P(9) / R(7)) decreases dramatically from 80 to 1.6 at high incident power levels. Then even though the incident power increases, the ratio stays stable at around 1.6. At first, a strong competition of the two emission lines happens with low incident power. The

P(9) line dominates firstly as the stimulated emission cross-section of P(9) is larger. Then the population accumulation on the J = 9 rotational states of v_1 vibrational state rapidly increases and the gain decreases. A larger population inversion from vibrational state v_1+v_3 to J=7 rotational state of $v_1$vibrational state occurs. Finally the ratio becomes stable to 1.6. Same phenomenon happens in the ring cavity configuration laser system.

It is noted that no other emission lines of acetylene fibre laser are reported when the pump is at single ro-vibrational transition line at 1.53 μm wavelength. It means the energy transfer via inter-molecular collisions only occurs at the specific energy level. Not enough energy can be transferred to depopulate the excited ro-vibrational state of laser upper level to its neighbour states for a new wavelength.

5.4 Pump absorption characterization measurement

To characterize the pump absorption property along the fibre length, we use a fibre side-scattering measurement.

5.4.1 Experiment setup

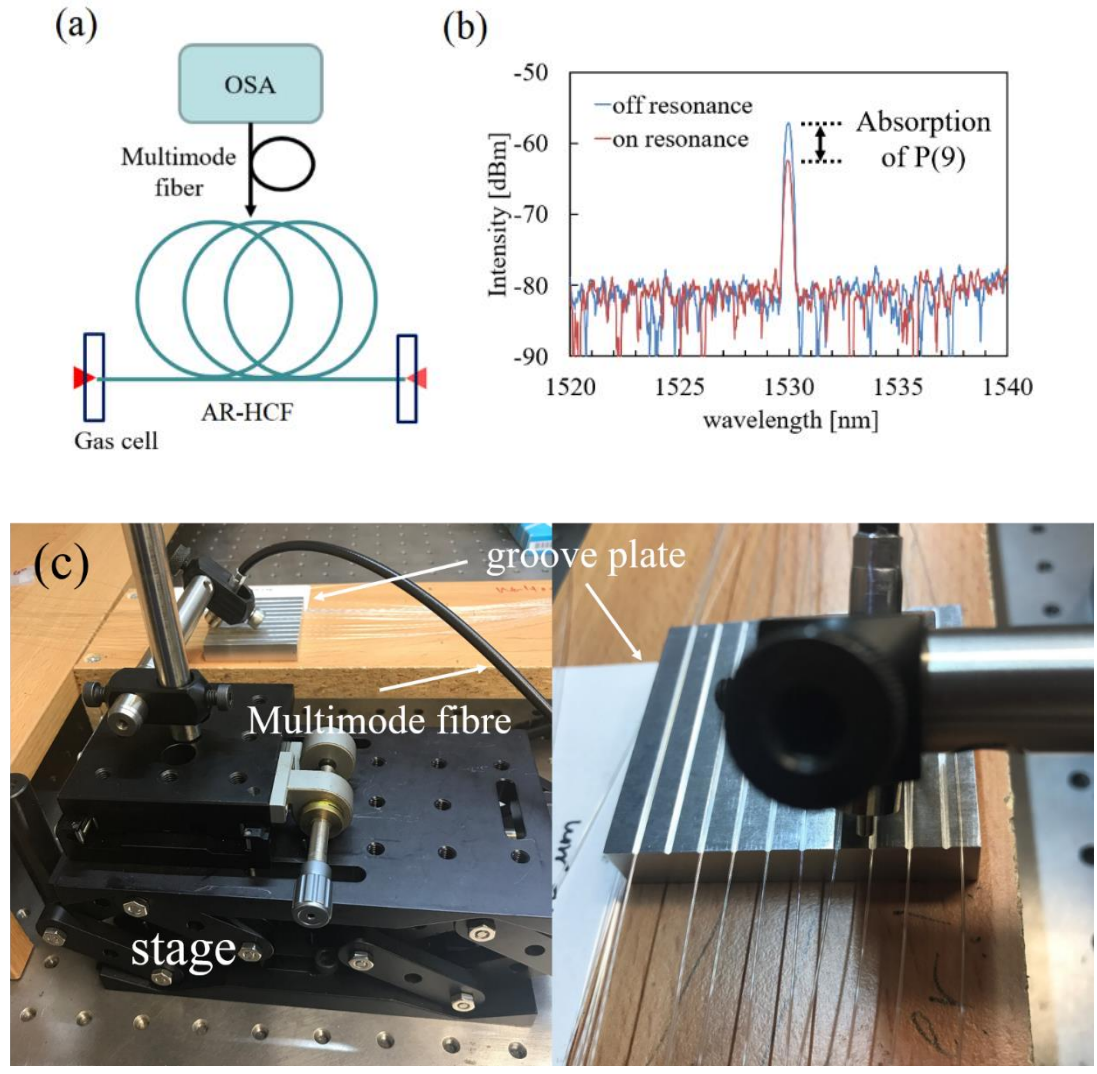

Fig. 5-10 Fibre side scattering measurement: (a) Experiment setup: a multimode fibre is used to collect and transmit the fibre side light into an optical spectrum analyser (YOKOGAWA AQ6370) [148]. (b) Typical measured spectra of the pump light at P(9) on/off resonant wavelength. The ratio of the peak intensities represents the relative absorbed pump power

[148]. (c) Experiment setup pictures: a metal groove plate is under the fibre. An adjustable xyz stage is built to hold the multimode fibre.

Fig. 5-10 (a) is the experimental diagram describing the fibre side measurement configuration. The gain fibre with 15 m in length is placed in circles. At one position, a multimode fibre is employed to collect and transmit the power to the OSA. In Fig. 5-10 (c), two pictures show the details of the fibre side measurement. The home-made metal with 10 grooves holds the fibre loops. An adjustable xyz stage is built to carry the multimode fibre. When the gain fibre on the metal is slightly bent, the pump light leaks out from the fibre side walls easily. The standard multimode fibre with 600 μm in core diameter is used to collect the fibre side pump light at same position of each fibre coiling circle in the same condition. At each collecting point, measurements are taken, via an optical spectrum analyser, at different levels of incident power (15 dBm, 30 dBm, and 40 dBm) with both on or off conditions of the P(9) resonant wavelengths. Fig. 5-10 (b) displays the typical measured side scattered spectra of pump light when the pump is tuned to on/off resonant P(9) acetylene absorption line. The off resonant wavelength is 0.05 nm away from the on resonant wavelength of 1530.385 nm. The EDFA amplification performance is the same at the off resonance wavelength as the on resonance one. The wavelength shift is not resolved by the OSA. The peak intensities on and off resonant are presented as P_{on} and P_{off}. The ratio of P_{on}/P_{off} is used to describe the pump absorption as a function of the position along the fibre.

5.4.2 Results with different incident powers

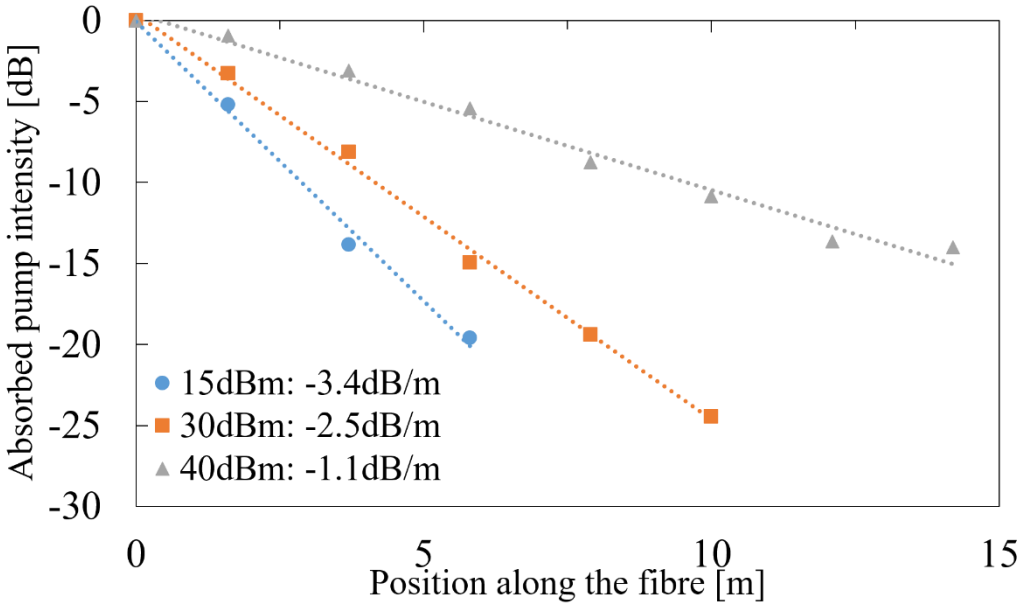

Fig. 5-11 Pump absorption as a function of the fibre length at 0.60 mbar pressure for different incident powers (15 dBm, 30 dBm and 40 dBm).

Fig. 5-11 describes the relative pump absorption along the fibre length for different incident power at 0.6 mbar. The absorption slope is found to be reduced as the incident power increases. The pump absorption is determined by the population distribution in the ground level and laser upper level. When the incident power is below the lasing threshold (e.g. 15 dBm, corresponding to 0.034 W), the absorption of acetylene gas is only related to the thermal equilibrium of the acetylene gas molecule. As the incident power increases, the absorption slope of acetylene gas increases. With higher incident power, more molecules participate in the stimulated emission processes, leading to a rapid reduction of the population in the ground level. The ground level cannot be fully re-populated immediately because the molecules are shelved in intermediate states. The fraction of the population on the intermediate states increases. Thus to make full use of the high incident power, a longer fibre length is required for higher power generation.

5.4.3 Results with different acetylene gas pressures

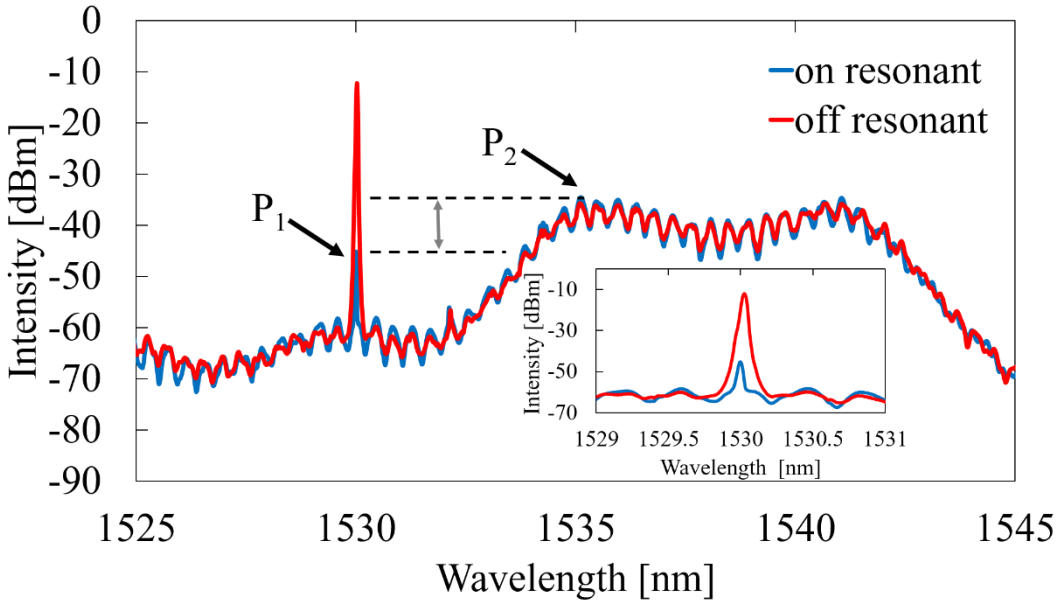

Fig. 5-12 Typical side-scattering pump light spectra when the seed laser is tuned on/off resonant P(9) wavelength. P_1 is the peak power at the on resonant pump wavelength. P_2 is the maximum power in the ASE region at the on resonant pump wavelength. Inset: zoom-in of measured spectral peaks at P(9) line. The OSA cannot resolve P(9) line.

The side-scattering measurements setup is similar as described in last section. The gain fibre of 31 m in length is described in section 5.2.1 and Fig. 5-3 (a). Instead of using peak intensities at P(9) line in on/off resonance conditions, we select P_2 (shown in Fig. 5-12), the maximum peak intensity on the ASE spectrum as a reference to normalize the residual pump power at P(9). P_1 is the peak intensity of the on resonance wavelength. The spectrum in the off resonance condition is shown as a reference. It confirms that the ASE spectrum does not change with a slight change of the wavelength (0.05 nm). Since the absorption only happens at the on resonant wavelength, the ASE region doesn't change along the fibre length. In addition, our repeated measurements confirmed the wavelength of P_2 barely changed in experiment. Thus the ratio of P_1/P_2 represents the acetylene absorption in a unit of dB. Fig. 5-12 shows typical measured spectra of pump light collected from the fibre side. The periodical fringes in the spectrum are the interferences caused by the uncoated gas cell window. The thickness of the window is 3 mm with two surfaces acting as a Fabry–Pérot resonator. The free spectral range is calculated as $\Delta\nu = c / 2L$

(c is the light speed in the material, L is the thickness), which means the period of the fringe is 0.4 nm.

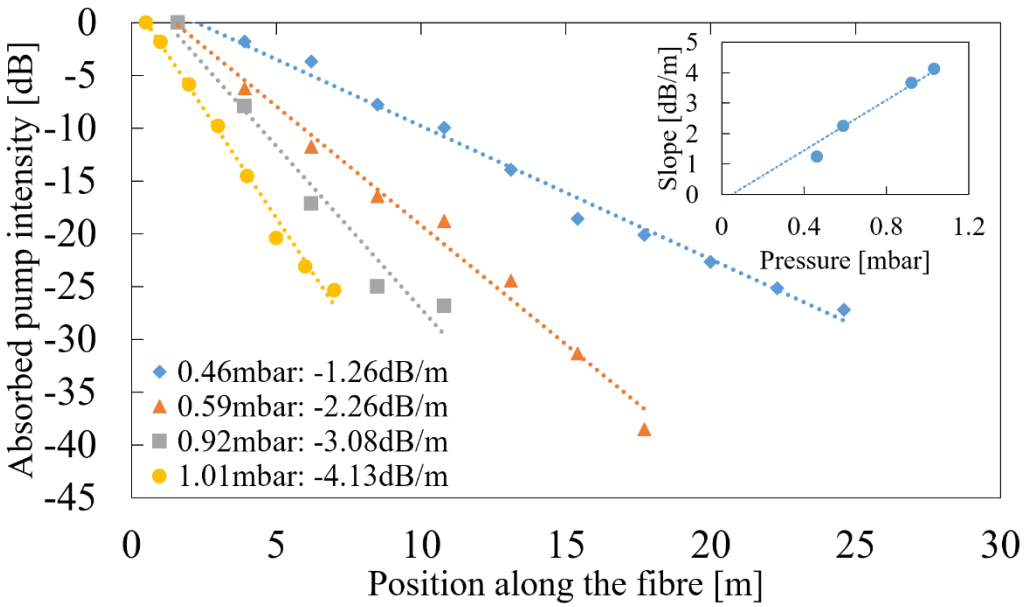

Fig. 5-13 Pump attenuation (P_1/P_2 ratio) along with the fibre length at different pressures. The dash lines are the linear fittings in the absorption lengths. Inset: the absorption slope as a function of the pressures. Approximate 4.12 dB/m/mbar is calculated by a linear fitting.

Fig. 5-13 shows the P_1/P_2 ratio (in unit of dB) as the function of fibre length under a maximum incident pump for a fixed fibre length. A maximum pump power is 40 dBm in specification and 9.6 W in practice. Finally 8.27 W pump power (including a strong ASE background) reaches the end of the gain fibre through a lens and uncoated CaF_2 gas cell window (same as before). Absorption length is defined as the fibre length in which acetylene gas absorbs the power intensity of 25 dB. For different pressures, the absorption lengths are found to be different. Beyond the absorption length, the absorption of residual effective pump power almost stops due to the strong laser power co-propagating along the length. Such effect is because of a relatively long lifetime of laser lower level. Within the absorption length, the rate of pump absorption clearly shows a monotonic increase with pressure. The pressure-induced collisions assist the populating of laser ground level which eventually increases the pump absorption. 4.12 dB/m/mbar is calculated by fitting the measured slopes.

It is noted under the same incident pump power (8.27 W), the absorption rate for 0.6 mbar in 15 m length in section 5.4.2 is 1.1 dB/m, smaller than 2.2 dB/m for 0.59 mbar in 31 m length in this section. The corresponding 3 μm laser output power are 1.12 W and 1.07 W respectively. We attribute the enhancement of pump light absorption in 31 m fibre to higher fibre losses at pump and lasing wavelengths. In fact, the maximum mid-IR output in 31 m fibre is measured when the optimized pressure is 0.46 mbar. The absorption rate for 0.46 mbar is 1.26 dB/m which is comparable to 1.1 dB/m in 15 m fibre for the optimized pressure.

In this case, optimized fibre length can be found by balancing the pump absorption rate and the fibre loss. Since the fibre attenuation is relatively small, it is possible to use a long piece of the fibre. However, another problem appears that the gas filling time for a long fibre is long. The leakage rate of the gas dominates after a few hours. Normally the leakage rate is 8.7 e-3 mbar/ hour. Longer the filling time leads to more air going into the gas cell. Before the fibre is completely filled from the beginning to the end, air goes into the fibre and affects the pressure. The filling time is usually 6-8 hours for 40 m fibre. Thus even through long piece of fibre is of interest, filling time for the long fibre should be considered.

To conclude, the reduced pump absorption under high power pump and the reduced laser output generation under higher pressure both suggest a long fibre length filled with low pressure acetylene. HCF with low loss is the key to efficient power scaling. Gas filling time is a limit for a long piece fibre.

5.5 Laser output results

Two different gain fibres are applied and the output powers are measured at different pressures. Output powers are compared as well as the thresholds and absorbed powers.

5.5.1 Output results with different fibre lengths

1) 31 m gain fibre

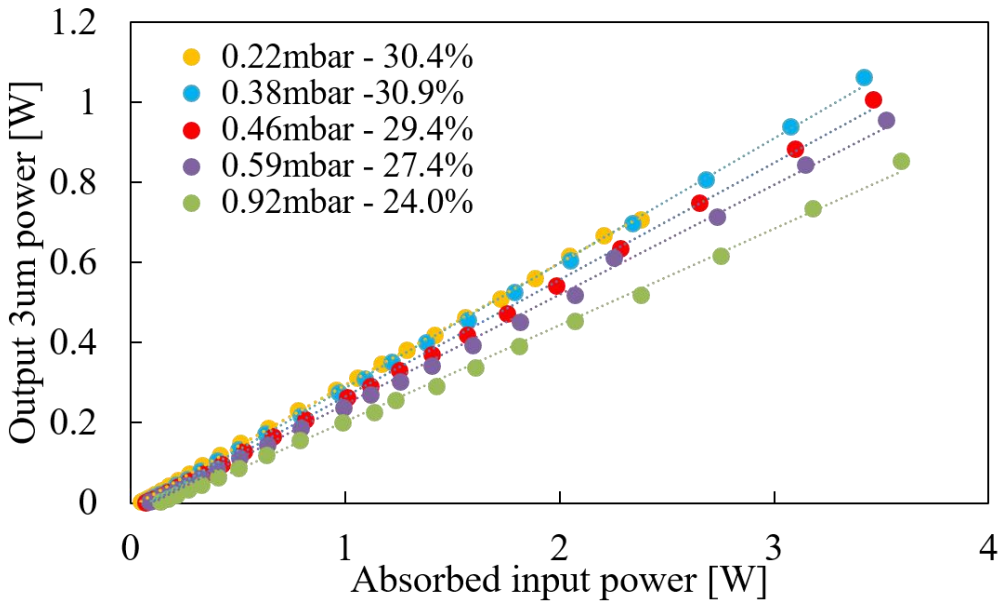

Fig. 5-14 Output mid-IR output power as a function of the absorbed incident power at different pressures in 31 m fibre length.

With 31 m gain fibre (described in section 5.2.1), the output power is shown in Fig. 5-14 as a function of the absorbed incident power. The absorbed incident power is defined as the incident power which is absorbed by the gain medium (acetylene gas). The incident power is measured before input fibre end. The output residual 1.53 μm power value is measured after a dichroic mirror at the output end. The absorbed incident power is the difference of the incident value and the residual value. The highest output power of 1.07 W is found at a pressure of 0.38 mbar with an absorbed incident power of 3.41 W, corresponding to a slope efficiency of 30.9 %. At lower pressure (e.g. 0.22 mbar), although the incident power is same as others, the

acetylene gas is not enough for absorbing the entire incident power so that the gain is saturated. So the highest output power at 0.22 mbar is lower than it at 0.38 mbar despite the similar slope efficiency. At higher pressures, both the output power and the slope efficiency decrease. It is because the inter-molecular collision rate increases, which increases the internal losses and decreases the gain.

2) 15 m gain fibre

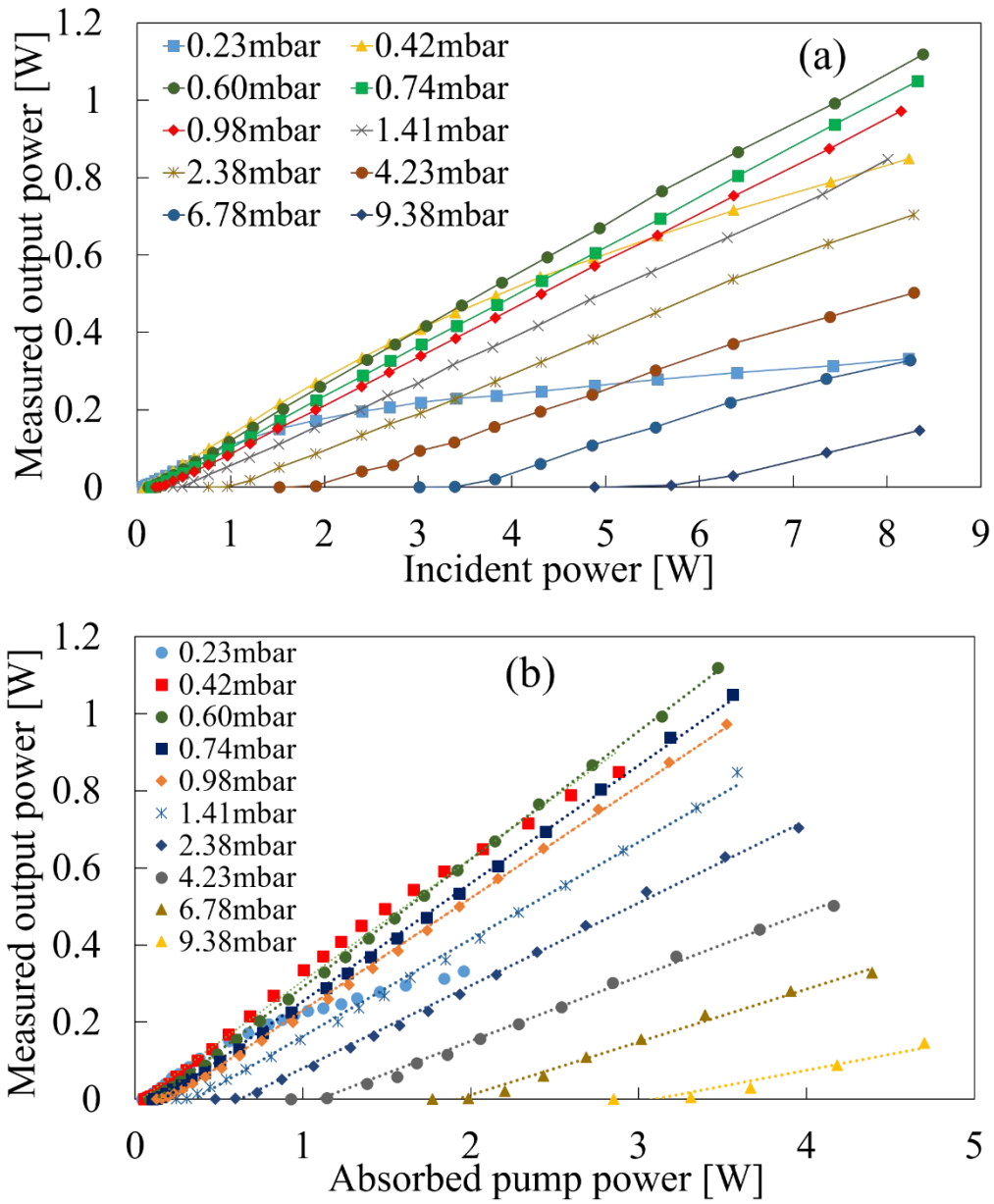

Fig. 5-15 For 15 m fibre length and various pressures [148] (a) Incident pump power – mid-IR laser output curves. (b) Absorbed pump power- mid-IR output power curves.

Another hollow core fibre (described in section 5.3.1 and Fig. 5-8) is used as gain fibre with different lengths of 6m, 15m and 40m. Typical performance is shown in Fig. 5-15 with 15 m fibre.

Fig. 5-15 (a) shows the 3 μm output power as a function of the incident pump power (including the broadband ASE). By measuring the incident power and the residual pump power, the power absorbed by the acetylene gas at P(9) line is calculated and used to re-plot the data as shown in Fig. 5-15 (b). The maximum output power is 1.12 W with a maximum slope efficiency relative to the absorbed pump of 33 % at 0.60 mbar. The trending details of the output along with the pressure has been explained in the last section. But the pressures with the highest output are different with different lengths of the fibre.

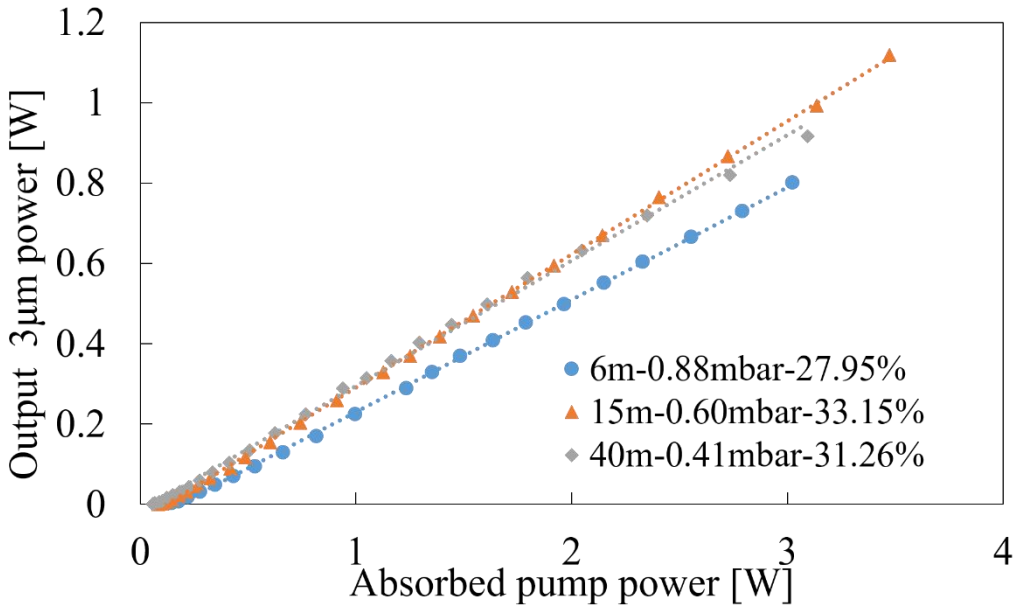

Fig. 5-16 With different fibre lengths of 6 m, 15 m and 40 m, highest output power is measured as a function of absorbed pump power at 0.88 mbar, 0.60 mbar and 0.41 mbar respectively.

Similar measurements were recorded using 6 m and 40 m fibres. Fig. 5-16 compares the highest output powers as a function of the absorbed pump power with 3 different fibre lengths (6 m, 15 m and 40 m) at their different pressures (0.88 mbar, 0.60 mbar and 0.41 mbar) respectively. For the shorter piece (6 m fibre), even though the pressure is higher, there are not enough gas molecules for absorbing the whole power. The pump power is not totally absorbed and the gain is saturated. With a

longer piece of the fibre (40 m), no saturation occurs at lower pressure (0.41 mbar) but the absorbed power loss is induced by the loss of the relative long piece of the fibre and less gas molecules.

Looking back to the fibre side-scattering spectrum measurement at different pressures (in Fig. 5-13), the pump power is almost absorbed in a shorter fibre length at a higher pressure. Then at lower pressures, the pump power is absorbed in a longer length along the fibre which is in agreement with the output results in Fig. 5-16. However, it is noted combining two results, a short piece of the fibre is not good enough for high power. Even though longer piece of fibre is better due to its more acetylene absorption, the transmission loss affects the output power. Thus the length of the fibre should be considered by balancing the absorption property and fibre transmission attenuation.

5.5.2 Results on thresholds, output power and maximum absorbed power

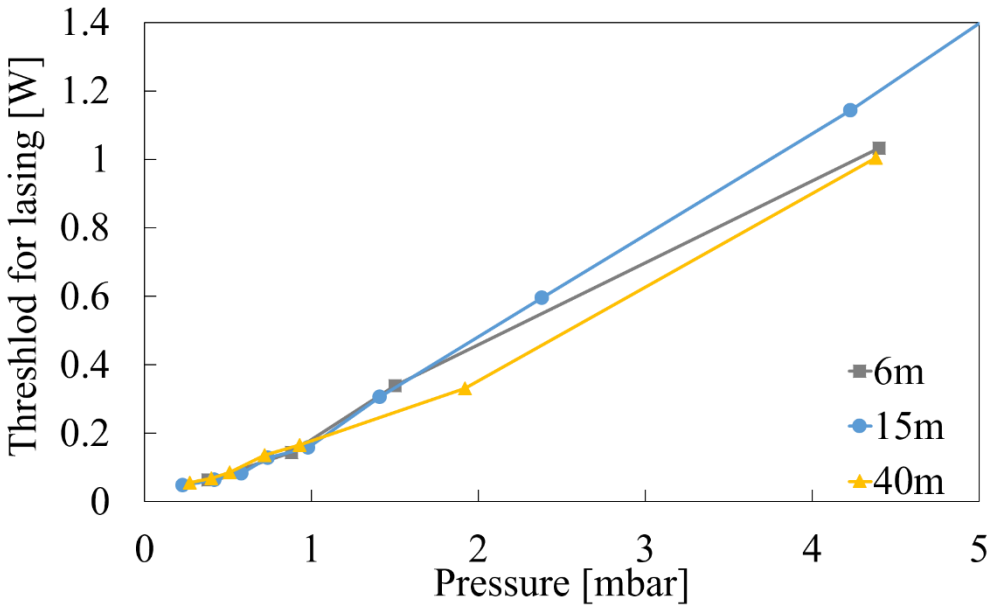

Fig. 5-17 Pressure - pump threshold for selected 3 different fibre lengths (6 m, 15 m and 40 m).

In fact, besides the difference of the output power at different pressures with different lengths of fibres, the thresholds and maximum absorbed pump power depend on the gas pressure as well.

In these experiments, a threshold occurs when amplified spontaneous emission into the low-loss fibre mode becomes the dominant route for de-excitation of the upper lasing level, reducing fluorescence and non-radiative transition processes and increasing the efficiency of converting pump photons into coherent fibre output. Fig. 5-17 summarizes the measured pump threshold for two fibre lengths and different pressures. In Fig. 5-17, the measured pump threshold is found to be almost independent of gain fibre length but dependent on the gas pressure. The minimum pump threshold is measured to be 48 mW when the pressure is 0.23 mbar for 15 m fibre length, larger than the 18 mW in a ring cavity with 31 m fibre at 0.6 mbar (in section 5.2.2). It confirms that ring cavity provides lower threshold but wastes more pump power in the cavity.

In terms of the output power and absorbed pump power, they are essentially related to transition time caused by the pressure-induced acetylene collision rate. As pressure is increased, collisions increasingly shorten the lifetime of the upper laser level. The J=8 rotational state of v_1+v_3 vibrational state has been reported to be depopulated at a total removal rate of 12.3×10^{-10} cm^3 s^{-1} (measured when pressure lower than 0.4 mbar) in [149], by the vibrational and rotational energy transfer processes via intermolecular collisions. However, when the gas is confined in the hollow core, the mean-free-path between intermolecular collisions is greater than the core radius for pressures lower than about 2.1 mbar. In this case, the inelastic relaxation via collisions of acetylene molecules with the silica core wall dominates the collision rate at low pressures and may have a major impact on the laser operation. Inelastic relaxation affects both the upper and lower laser levels as well as the ground state. On one hand, it assists repopulation of the ground level and plays a valuable role in maintaining CW laser operation. On the other hand, it reduces the population of both the upper and lower laser levels.

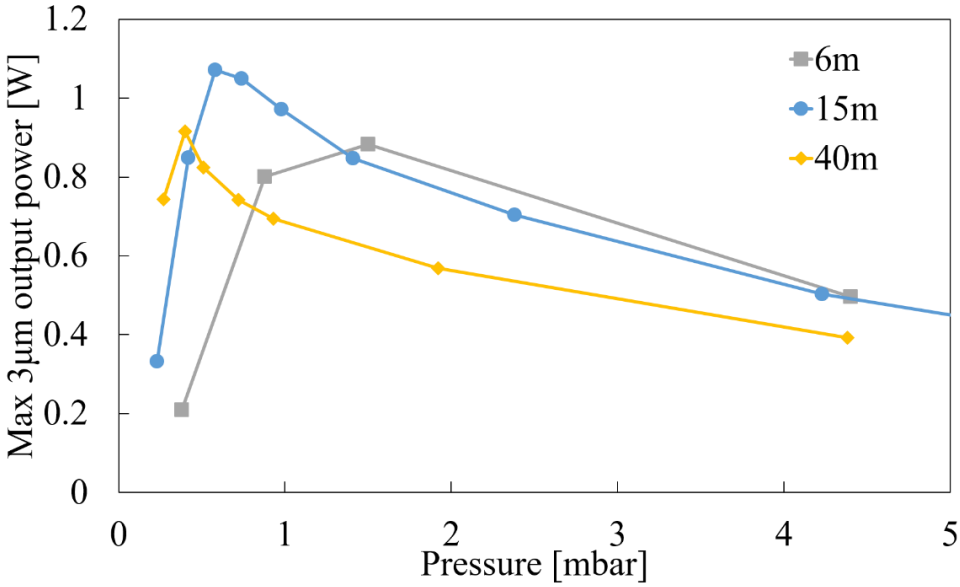

Fig. 5-18 Summary of maximum output power as a function of the pressure with 6 m, 15 m and 40 m fibre.

Fig. 5-18 shows the maximum mid-IR laser output power versus pressure for different fibre length. For different fibre lengths, the highest powers achieved depend on the pressure. (e.g. for 6m and 40 m fibre, the maximum laser outputs are measured as 0.80 W and 0.92 W at 0.88 mbar and 0.42 mbar, with the slope efficiency of 28% and 31.2% respectively). The longer the fibre length, the lower pressure is needed to be the highest output power is as we explained in Fig. 5-16. Below the pressure for the highest power, the output power drops rapidly. As the pressure increases, the pump absorption increases to the peak (e.g. 0.60 mbar for 15 m fibre) before it decreases. When the gas molecular density becomes higher, the gain decreases. So does the output power. The maximum laser power conversion efficiency is achieved at the extreme value of gain as a function of pressure which is dependent on the gain fibre length.

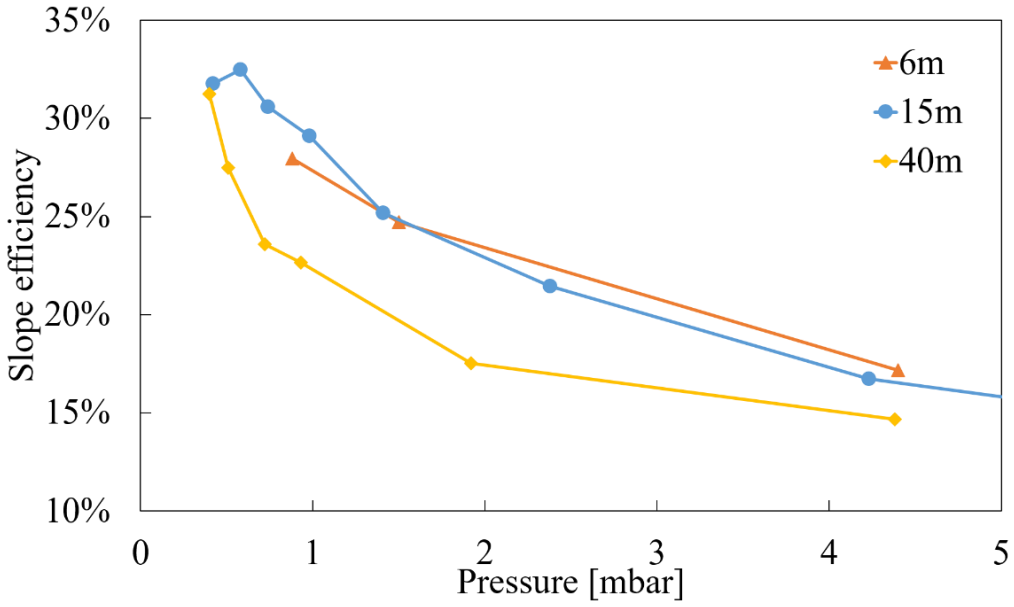

Fig. 5-19 Summary of measured slope efficiencies for three different fibre lengths as function of acetylene pressure. Slope efficiencies in the saturation situation are not included.

Fig. 5-19 summarizes the measured slope efficiencies as functions of the pressure with 6 m, 15 m and 40 m fibre. It corresponds to the output power-pressure results in Fig. 5-18. Using 15 m fibre for example, in the low pressure region below 0.6 mbar, the slope efficiency increases with pressure, staying above 30 %. In this regime, increasing pressure means more molecules contributing to the gain as well as the pump absorption. 33 % slope efficiency is reached at 0.6 mbar. As the gas pressure is further increased, despite a stronger pump absorption as a consequence of the higher molecular density, the fibre gain decreases. The pressure-induced gain reduction dominates and completely overwhelms the advantage of high molecular density at higher pressure. In this case, the slope efficiency drops gradually along with the increasing pressure.

Compared these three fibre lengths of 6 m, 15 m and 40 m, the slope efficiencies have similar dependence on pressures, but the absolute slope efficiency at low pressures are different. The reduction of conversion efficiency due to a shorter gain fibre length has also been confirmed in the pulse-pumped single-pass configuration.

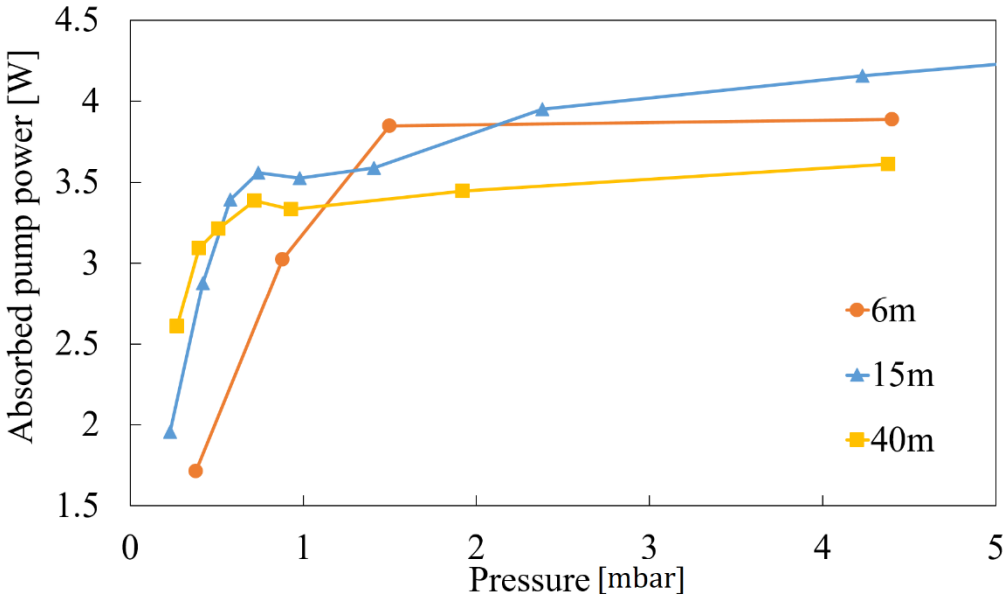

Fig. 5-20 Summary of measured maximum absorbed pump power for three different fibre lengths as function of acetylene pressure.

Fig. 5-20 shows the measured absorbed pump power with a maximum incident power as a function of the pressure for three different lengths of the fibre. The tendency can be explained as same as in previous paragraphs and in section 5.5.1. At low pressures below 1 mbar, the increasing gain induced by more and more acetylene molecules leads to an increasing absorbed pump power. With a higher pressure of over 1 mbar, high acetylene molecule density causes a reduction of the gain as well as the absorbed pump power, resulting a slow increase of the absorbed pump power. Since there are only 4 data points in 6 m results, some variation uncertainty may happen which makes the 4.5 mbar point stay between the other two lines. For difference of the fibre lengths, slight differences of the absorbed pump power are achieved. Longer fibre (e.g. 40 m fibre) is easier to reach the gain inflection points because more molecules is provided at low pressures.

These are all the results of the power scaled CW acetylene filled fibre laser with single pass configuration. The output results depend on the pressure and fibre length. By comparing the pulsed laser in [66, 150], the importance of acetylene pressure on the laser power-scaling performance has been also confirmed. For pulse widths approximately 1 ns, a constant 20 % slope efficiency was reported for pressures in a range from 1.6 mbar to 18.7 mbar [88]. As the pulse length becomes

shorter and enters the transient region, the pump duration becomes shorter than the collisional kinetic process. We can then assume that no collision-induced changes take place (over a certain pressure range) during the pulse duration. In that case, only a small fraction of molecules can participate in the lasing process, determined by the thermal equilibrium. In this case, higher pressure may be preferable for more efficiently utilizing the pump power.

5.6 Conclusion

In chapter 5, we demonstrate an acetylene filled hollow core fibre laser with both ring cavity and single pass ASE configurations. The ring cavity configuration provides a lower threshold but a lower output power. The mid-IR laser is lost in the cavity rather than emitted from the laser as output beam. The single pass ASE configuration is a better way to achieve high power output.

A method to measure the acetylene absorption along the fibre length is demonstrated as fibre side-scattering spectrum measurement. Different incident powers and pressures are measured to present the characteristics of the absorption.

Then in terms of the single pass ASE configuration, a systematic study of the high power depended on gas pressure, fibre length, pump intensity and pump absorption reveals a reduction of the pump absorption (and therefore fibre gain) with increasing pump flux and the degradation of gain performance at high gas pressure. Taken together these necessitate the use of increasingly long length fibre for efficient laser operation at increased powers. We have demonstrated 1.12 W output power at 3 μm wavelength with 33 % slope efficiency in a 15 m low-loss AR-HCF filled with acetylene gas at 0.6 mbar. It is the best ever result for mid-infrared acetylene filled fibre laser in CW regime comparing to other reported [67].

CHAPTER 6 CONCLUSION AND FUTURE WORK

6.1 Conclusion

In this thesis, I have demonstrated my study of hollow core fibres, especially the mode property of this fibre. One of the applications is also investigated as optically pumped acetylene gas filled hollow core fibre lasers with high output power. The work and results can be concluded as follows:

1. S^2 imaging measurement is a method to detect and analyse the mode contents in the fibre. It has been realized to analyse the mode contents in hollow core fibre for the first time. Different hollow core fibre was tested and this measurement has been optimized in aspects of the fibre length, the wavelength range and the number of the spectrum measurement to achieve accurate mode contents and different modes group velocities. The fibre length should be neither too long (more than 19 m) nor too short (less than 2 m) because of the limitation of the OSA resolution. The wavelength range and the number of the spectrum measurement affects the time of the whole measurement. 400 times spectrum measurement cost 1.5 hours with the light source stable. In this case, a fundamental mode and three high order modes were resolved accurately with their group delay differences in a 19 m HCF at 1 micron.
2. A new type of hollow core fibre was fabricated with 7 ice-cream-shaped capillaries in the cladding. The single mode guidance performance was well presented by S^2 imaging measurement and near-field image pattern. Only single mode pattern was detected when the fibre is 10 m in length. However, in traditional 8 capillaries HCF with similar length, the high order modes were found easily. Comparing to traditional 8-capillary HCF, this new fibre of 7 capillaries offers advantages for a wide range for applications. This can be explained by the mode coupling from the core to the cladding. As the capillary diameter is close to the core diameter, the modes refractive indices are close

and easily coupled from the core to the capillary in the cladding. In this case, the high order modes in the 7-capillary fibre are removed from the core.

3. A continuous wave acetylene gas filled hollow core fibre laser was pumped by an Erbium-doped fibre amplified tunable laser diode. This pump source provides a high output power of 40 dBm at a wavelength of 1530 nm (meets the acetylene P (9) line). The laser system built in both cavity-based configuration and single pass ASE configuration is capable to lasing at wavelength range of 3.1~3.2 μm. With the same condition, the ring cavity configuration laser always has an output power of around 60% of the single pass configuration laser. Despite the ring cavity configuration laser has a lower lasing threshold, it cannot provide higher output power. The single pass ASE configuration performs more robust and reliable results in aspects of high power output and high slope efficiency.

4. To achieve the highest output power, we have demonstrated the optimized laser system with proper fibre length and gas pressure. Fibre side scattering measurement was first to adopt to analyse the gas attenuation along the fibre length. From the fibre side scattering measurement, it is can be concluded: the longer fibre and lower pressure could be the best for the high output power. However, when the fibre gets longer, there is enough light gas interaction length but higher transmission loss and extra gas filling time. When the pressure gets lower, there are not sufficient gas molecules for interacting and the pressure cannot be detected properly. 4.12 dB/m/mbar is found to summarize the relationship between the fibre attenuation and the gas pressure. This fibre side scattering measurement is useful in many other fibre detection applications.

5. From the results of the fibre side scattering measurement, the long fibre length and the low gas pressure are the best choice. However, the optimized fibre length and gas pressure depend on the filling time and the fibre attenuation. With the single pass configuration, by comparing different lengths (6 m, 15 m, 30 m and 40 m) of the fibre and different gas pressures (from 0.2 mbar to 9 mbar) in aspects of output powers, lasing thresholds and slope efficiencies, 15

m fibre with a pressure of 0.6 mbar achieved the highest power of 1.12 W with a slope efficiency of 33%, which is 400 times larger than the previous results in other publications [67]. The laser system is the first high power 3 μm gas fibre laser in the CW regime.

6.2 Future work

The development of this gas filled hollow fibre lasers is an attractive field which still remains fertile.

1. As for the hollow core fibre, the fabrication of hollow core fibre with low attenuations needs to be explored especially in very short wavelengths such as ultra-violet spectral range. In this wavelength region, silica fibre cannot transmit light as well. Hollow core fibres will have a wide range of applications in this region. However, the fibre and its strut in the cladding will be very thin. The main limitation of this fabrication technique is to avoiding breaking the thin structure during drawing. Many parameters should be optimized in this process including the speed of the fibre feed into and out of the furnace and the temperature of the furnace.
2. Different designs have been emerged for dramatically decreasing the attenuation level but need to be realized in fabrication processes. Some new designs have already been simulated such as HCF with ellipse capillaries in the cladding. They are difficult to draw in practice with our current technique. Some new methods may be invented to fix the drawing problems.
3. In terms of the gas fibre laser, acetylene is not the only molecule for mid-infrared emission. Other gas molecules are worth investigating for mid-infrared and far-infrared regions such as HBr, HCN and CO_2.
4. Although the current setup is fine for demonstrating, the bulky gas cells and gas tube are barriers in simplifying for the commercial usage. To seal the gas in the fibre and make all gas fibre laser is the ultimate goal for applications for improved performance.
5. Pump light source is another component to be improved. If the pump source can be integrated, the whole laser setup would be useful for a wide range of applications.

References:

[1] K. C. Kao and G. A. Hockham. (1966, Dielectric-fibre surface waveguides for optical frequencies. *Proceedings of the Institution of Electrical Engineers 113(7),* 1151-1158. Available: http://digital-library.theiet.org/content/journals/10.1049/piee.1966.0189

[2] K. C. Kao and T. W. Davies, "Spectrophotometric studies of ultra low loss optical glasses I: single beam method," *Journal of Physics E: Scientific Instruments,* vol. 1, p. 1063, 1968.

[3] T. Miya, Y. Terunuma, T. Hosaka, and T. Miyashita, "Ultimate low-loss single-mode fibre at 1.55 μm," *Electronics Letters,* vol. 15, p. 106, 1979.

[4] J. Tyndall, "Notes of a Course of Nine Lectures on Light: Delivered at the Royal Institution of Great Britain, April 8-June 3, 1869. ," *Longmans, Green, and Company,* 1872.

[5] J. A. Buck, *Fundamentals of optical fibers*. John Wiley & Sons, 2004.

[6] K. T. Grattan and B. T. Meggitt, *Optical fiber sensor technology* vol. 1. Springer, 1995.

[7] E. Udd and W. B. Spillman Jr, *Fiber optic sensors: an introduction for engineers and scientists*. John Wiley & Sons, 2011.

[8] J. C. Palais, *Fiber optic communications*. Prentice Hall Englewood Cliffs, 1988.

[9] O. G. Okhotnikov, *Fiber lasers*. John Wiley & Sons, 2012.

[10] J. R. Carson, S. P. Mead, and S. A. Schelkunoff, "Hyper-frequency wave guides: Mathematical theory," *The Bell System Technical Journal,* vol. 15, pp. 310-333, 1936.

[11] D. A. Alsberg, J. C. Bankert, and P. T. Hutchison, "WT4 millimeter waveguide system: The WT4/WT4a millimeter-wave transmission system," *The Bell System Technical Journal,* vol. 56, pp. 1829-1848, 1977.

[12] E. A. Marcatili and R. Schmeltzer, "Hollow metallic and dielectric waveguides for long distance optical transmission and lasers," *Bell Labs Technical Journal,* vol. 43, pp. 1783-1809, 1964.

[13] P. Kaiser and H. Astle, "Low-loss single-material fibers made from pure fused silica," *The Bell System Technical Journal,* vol. 53, pp. 1021-1039, 1974.

[14] E. Garmire, T. McMahon, and M. Bass, "Flexible infrared waveguides for high-power transmission," *IEEE Journal of Quantum Electronics,* vol. 16, pp. 23-32, 1980.

[15] J. A. Harrington, "A review of IR transmitting, hollow waveguides," *Fiber & Integrated Optics,* vol. 19, pp. 211-227, 2000.

[16] J. A. Harrington and C. C. Gregory, "Hollow sapphire fibers for the delivery of CO_2 laser energy," *Optics Letters,* vol. 15, pp. 541-543, 1990.

[17] A. Hongo, K. i. Morosawa, K. Matsumoto, T. Shiota, and T. Hashimoto, "Transmission of kilowatt-class CO_2 laser light through dielectric-coated metallic hollow waveguides for material processing," *Applied Optics,* vol. 31, pp. 5114-5120, 1992.

[18] E. Yablonovitch, "Inhibited spontaneous emission in solid-state physics and electronics," *Physical Review Letters,* vol. 58, p. 2059, 1987.

[19] S. John, "Strong localization of photons in certain disordered dielectric superlattices," *Physical Review Letters,* vol. 58, p. 2486, 1987.

[20] J. Knight, T. Birks, P. S. J. Russell, and D. Atkin, "All-silica single-mode optical fiber with photonic crystal cladding," *Optics Letters,* vol. 21, pp. 1547-1549, 1996.

[21] R. Cregan, B. Mangan, J. Knight, T. Birks, P. S. J. Russell, P. Roberts, *et al.*, "Single-mode photonic band gap guidance of light in air," *Science,* vol. 285, pp. 1537-1539, 1999.

[22] F. Benabid, J. C. Knight, G. Antonopoulos, and P. S. J. Russell, "Stimulated Raman scattering in hydrogen-filled hollow-core photonic crystal fiber," *Science,* vol. 298, pp. 399-402, 2002.

[23] P. Roberts, F. Couny, H. Sabert, B. Mangan, D. Williams, L. Farr, *et al.*, "Ultimate low loss of hollow-core photonic crystal fibres," *Optics Express,* vol. 13, pp. 236-244, 2005.

[24] F. Couny, F. Benabid, and P. Light, "Large-pitch kagome-structured hollow-core photonic crystal fiber," *Optics Letters,* vol. 31, pp. 3574-3576, 2006.

[25] F. Couny, P. J. Roberts, T. Birks, and F. Benabid, "Square-lattice large-pitch hollow-core photonic crystal fiber," *Optics Express,* vol. 16, pp. 20626-20636, 2008.

[26] Y. Y. Wang, F. Couny, P. J. Roberts, and F. Benabid, "Low loss broadband transmission in optimized core-shape Kagome hollow-core PCF," in *CLEO/QELS: 2010 Laser Science to Photonic Applications,* pp. 1-2, 2010.

[27] Y. Y. Wang, N. V. Wheeler, F. Couny, P. J. Roberts, and F. Benabid, "Low loss broadband transmission in hypocycloid-core Kagome hollow-core photonic crystal fiber," *Optics Letters,* vol. 36, pp. 669-671, 2011.

[28] L. Vincetti and V. Setti, "Waveguiding mechanism in tube lattice fibers," *Optics Express,* vol. 18, pp. 23133-23146, 2010.

[29] F. Gérôme, R. Jamier, J.-L. Auguste, G. Humbert, and J.-M. Blondy, "Simplified hollow-core photonic crystal fiber," *Optics Letters,* vol. 35, pp. 1157-1159, 2010.

[30] C. Wei, R. Joseph Weiblen, C. R. Menyuk, and J. Hu, "Negative curvature fibers," *Advances in Optics and Photonics,* vol. 9, pp. 504-561, 2017.

[31] A. D. Pryamikov, A. S. Biriukov, A. F. Kosolapov, V. G. Plotnichenko, S. L. Semjonov, and E. M. Dianov, "Demonstration of a waveguide regime for a silica hollow - core microstructured optical fiber with a negative curvature of the core boundary in the spectral region > 3.5 μm," *Optics Express,* vol. 19, pp. 1441-1448, 2011.

[32] A. F. Kosolapov, A. D. Pryamikov, A. S. Biriukov, V. S. Shiryaev, M. S. Astapovich, G. E. Snopatin, *et al.*, "Demonstration of CO_2-laser power delivery through chalcogenide-glass fiber with negative-curvature hollow core," *Optics Express,* vol. 19, pp. 25723-25728, 2011.

[33] F. Yu and J. C. Knight, "Spectral attenuation limits of silica hollow core negative curvature fiber," *Optics Express,* vol. 21, pp. 21466-21471, 2013.

[34] P. Jaworski, F. Yu, R. R. J. Maier, W. J. Wadsworth, J. C. Knight, J. D. Shephard, *et al.*, "Picosecond and nanosecond pulse delivery through a hollow-core Negative Curvature Fiber for micro-machining applications," *Optics Express,* vol. 21, pp. 22742-22753, 2013.

[35] C. Harvey, F. Yu, J. C. Knight, W. Wadsworth, and P. Almeida, "Reducing Nonlinear Limitations of Ytterbium Mode-Locked Fibre Lasers with Hollow-Core Negative Curvature Fibre," in *CLEO: 2015*, San Jose, California, p. STh1L.5, 2015.

[36] F. Yu, W. J. Wadsworth, and J. C. Knight, "Low loss silica hollow core fibers for 3–4 μm spectral region," *Optics Express,* vol. 20, pp. 11153-11158, 2012.

[37] A. N. Kolyadin, A. F. Kosolapov, A. D. Pryamikov, A. S. Biriukov, V. G. Plotnichenko, and E. M. Dianov, "Light transmission in negative curvature hollow core fiber in extremely high material loss region," *Optics Express,* vol. 21, pp. 9514-9519, 2013.

[38] W. Belardi and J. C. Knight, "Hollow antiresonant fibers with low bending loss," *Optics express,* vol. 22, pp. 10091-10096, 2014.

[39] W. Belardi and J. C. Knight, "Hollow antiresonant fibers with reduced attenuation," *Optics Letters,* vol. 39, pp. 1853-1856, 2014.

[40] F. Poletti, "Nested antiresonant nodeless hollow core fiber," *Optics Express,* vol. 22, pp. 23807-23828, 2014.

[41] W. Belardi, "Design and Properties of Hollow Antiresonant Fibers for the Visible and Near Infrared Spectral Range," *Journal of Lightwave Technology,* vol. 33, pp. 4497-4503, 2015.

[42] M. I. Hasan, N. Akhmediev, and W. Chang, "Positive and negative curvatures nested in an antiresonant hollow-core fiber," *Optics Letters,* vol. 42, pp. 703-706, 2017.

[43] M. S. Habib, O. Bang, and M. Bache, "Low-loss single-mode hollow-core fiber with anisotropic anti-resonant elements," *Optics Express,* vol. 24, pp. 8429-8436, 2016.

[44] K. Saitoh, N. John Florous, T. Murao, and M. Koshiba, "Design of photonic band gap fibers with suppressed higher-order modes: Towards the development of effectively single mode large hollow-core fiber platforms," *Optics Express,* vol. 14, pp. 7342-7352, 2006.

[45] J. M. Fini, J. W. Nicholson, R. S. Windeler, E. M. Monberg, L. Meng, B. Mangan, *et al.*, "Low-loss hollow-core fibers with improved single-modedness," *Optics Express,* vol. 21, pp. 6233-6242, 2013.

[46] C. Wei, R. A. Kuis, F. Chenard, C. R. Menyuk, and J. Hu, "Higher-order mode suppression in chalcogenide negative curvature fibers," *Optics Express,* vol. 23, pp. 15824-15832, 2015.

[47] P. Uebel, M. C. Günendi, M. H. Frosz, G. Ahmed, N. N. Edavalath, J.-M. Ménard, *et al.*, "Broadband robustly single-mode hollow-core PCF by resonant filtering of higher-order modes," *Optics Letters,* vol. 41, pp. 1961-1964, 2016.

[48] A. Hartung, J. Kobelke, A. Schwuchow, J. Bierlich, J. Popp, M. A. Schmidt, *et al.*, "Low-loss single-mode guidance in large-core antiresonant hollow-core fibers," *Optics Letters,* vol. 40, pp. 3432-3435, 2015.

[49] M. Michieletto, J. K. Lyngsø, C. Jakobsen, J. Lægsgaard, O. Bang, and T. T. Alkeskjold, "Hollow-core fibers for high power pulse delivery," *Optics Express,* vol. 24, pp. 7103-7119, 2016.

[50] F. Yu, M. Xu, and J. C. Knight, "Experimental study of low-loss single-mode performance in anti-resonant hollow-core fibers," *Optics Express,* vol. 24, pp. 12969-12975, 2016.

[51] M. Xu, F. Yu, and J. Knight, "Low-Loss Anti-Resonant Hollow-Core Fibers with Single-Mode Performance," in *Advanced Photonics 2016 (IPR, NOMA, Sensors, Networks, SPPCom, SOF)*, Vancouver, p. SoM3F.5, 2016.

[52] J. Nicholson, A. D. Yablon, S. Ramachandran, and S. Ghalmi, "Spatially and spectrally resolved imaging of modal content in large-mode-area fibers," *Optics Express,* vol. 16, pp. 7233-7243, 2008.

[53] D. J. Richardson, N. V. Wheeler, Y. Chen, J. R. Hayes, S. R. Sandoghchi, G. T. Jasion, *et al.*, "Hollow core fibres and their applications," in *2017 Optical Fiber Communications Conference and Exhibition (OFC)*, pp. 1-80, 2017.

[54] J. D. Shephard, A. Urich, R. M. Carter, P. Jaworski, R. R. J. Maier, W. Belardi, *et al.*, "Silica hollow core microstructured fibers for beam delivery in industrial and medical applications," *Frontiers in Physics,* vol. 3, 2015.

[55] D. S. Bykov, O. A. Schmidt, T. G. Euser, and P. S. J. Russell, "Flying particle sensors in hollow-core photonic crystal fibre," *Nature Photonics,* vol. 9, pp. 461-465, 2015.

[56] F. Yu and J. C. Knight, "Negative Curvature Hollow-Core Optical Fiber," *IEEE Journal of Selected Topics in Quantum Electronics,* vol. 22, pp. 146-155, 2016.

[57] R. Kitamura, L. Pilon, and M. Jonasz, "Optical constants of silica glass from extreme ultraviolet to far infrared at near room temperature," *Applied Optics,* vol. 46, pp. 8118-8133, 2007.

[58] A. Urich, R. R. J. Maier, F. Yu, J. C. Knight, D. P. Hand, and J. D. Shephard, "Flexible delivery of Er:YAG radiation at 2.94 μm with negative curvature silica glass fibers: a new solution for minimally invasive surgical procedures," *Biomedical Optics Express,* vol. 4, pp. 193-205, 2013.

[59] M. Xu, F. Yu, M. R. Hassan, and J. Knight, "Continuous-Wave 3.1 μm Gas Fiber Laser with 0.47 W Output Power," in *Conference on Lasers and Electro-Optics*, San Jose, California, p. SF2K.4, 2017.

[60] Z. Wang, F. Yu, W. J. Wadsworth, and J. C. Knight, "Efficient 1.9 μm emission in H_2-filled hollow core fiber by pure stimulated vibrational Raman scattering," *Laser Physics Letters,* vol. 11, p. 105807, 2014.

[61] Y. Chen, Z. Wang, B. Gu, F. Yu, and Q. Lu, "Achieving a 1.5 μm fiber gas Raman laser source with about 400 kW of peak power and a 6.3 GHz linewidth," *Optics Letters,* vol. 41, pp. 5118-5121, 2016.

[62] A. M. Jones, A. V. Nampoothiri, A. Ratanavis, T. Fiedler, N. V. Wheeler, F. Couny, *et al.*, "Mid-infrared gas filled photonic crystal fiber laser based on population inversion," *Optics express,* vol. 19, pp. 2309-2316, 2011.

[63] A. V. V. Nampoothiri, A. M. Jones, C. Fourcade-Dutin, C. Mao, N. Dadashzadeh, B. Baumgart, *et al.*, "Hollow-core Optical Fiber Gas Lasers (HOFGLAS): a review [Invited]," *Optical Materials Express,* vol. 2, pp. 948-961, 2012.

[64] C. F.-D. A. M. Jones, C. Mao, B. Baumgart, A. V. V. Nampoothiri, N. Campbell, Y. Wang, F. Benabid, W. Rudolph, B. R. Washburn, K. L. Corwin, "Characterization of mid-infrared emissions from C_2H_2, CO, CO_2, and HCN-filled hollow fiber lasers," in *SPIE LASE*, p. 82373Y, 2012.

[65] A. V. V. Nampoothiri, A. Ratanavis, N. Campbell, and W. Rudolph, "Molecular C_2H_2 and HCN lasers pumped by an optical parametric oscillator in the 1.5-μm band," *Optics Express*, vol. 18, pp. 1946-1951, 2010.

[66] Z. Wang, W. Belardi, F. Yu, W. J. Wadsworth, and J. C. Knight, "Efficient diode-pumped mid-infrared emission from acetylene-filled hollow-core fiber," *Optics Express*, vol. 22, pp. 21872-21878, 2014.

[67] M. R. Abu Hassan, F. Yu, W. J. Wadsworth, and J. C. Knight, "Cavity-based mid-IR fiber gas laser pumped by a diode laser," *Optica*, vol. 3, pp. 218-221, 2016.

[68] P. S. J. Russell, P. Holzer, W. Chang, A. Abdolvand, and J. C. Travers, "Hollow-core photonic crystal fibres for gas-based nonlinear optics," *Nat Photon*, vol. 8, pp. 278-286, 2014.

[69] M. G. Welch, K. Cook, R. A. Correa, F. Gérôme, W. J. Wadsworth, A. V. Gorbach, *et al.*, "Solitons in hollow core photonic crystal fiber: engineering nonlinearity and compressing pulses," *Journal of Lightwave Technology*, vol. 27, pp. 1644-1652, 2009.

[70] A. Ermolov, K. F. Mak, M. H. Frosz, J. C. Travers, and P. S. J. Russell, "Supercontinuum generation in the vacuum ultraviolet through dispersive-wave and soliton-plasma interaction in a noble-gas-filled hollow-core photonic crystal fiber," *Physical Review A*, vol. 92, p. 033821, 2015.

[71] M. Habib, C. Markos, O. Bang, and M. Bache, "Multiple soliton compression stages from competing plasma nonlinearities in mid-IR gas-filled hollow-core fibers," *arXiv preprint arXiv:1702.00267*, 2017.

[72] A. Abdolvand, A. Walser, M. Ziemienczuk, T. Nguyen, and P. S. J. Russell, "Generation of a phase-locked Raman frequency comb in gas-filled hollow-core photonic crystal fiber," *Optics Letters*, vol. 37, pp. 4362-4364, 2012.

[73] G. R. Gordon, "The LASER, Light Amplification by Stimulated Emission of Radiation," *The Ann Arbor Conference on Optical Pumping*, p. 128, 1959.

[74] T. H. Maiman, "Stimulated optical radiation in ruby," *Nature*, vol. 187, pp. 493-494, 1960.

[75] O. Svelto, *Principles of Lasers*. Springer Science & Business Media, 2010.

[76] J. A. Piper and C. E. Webb, "A hollow cathode device for CW helium-metal vapour laser systems," *Journal of Physics D: Applied Physics*, vol. 6, p. 400, 1973.

[77] E. T. Gerry and D. A. Leonard, " Measurement of 10.6 μm CO_2 laser transition probability and optical broadening cross sections " *Applied Physics Letters,* vol. 8, pp. 227-229, 1966.

[78] X. Zhu and N. Peyghambarian, "High-power ZBLAN glass fiber lasers: review and prospect," *Advances in OptoElectronics,* vol. 2010, 2010.

[79] S. D. Jackson, "Towards high-power mid-infrared emission from a fibre laser," *Nature Photonics,* vol. 6, pp. 423-431, 2012.

[80] M. C. Falconi, D. Laneve, and F. Prudenzano, "Advances in Mid-IR Fiber Lasers: Tellurite, Fluoride and Chalcogenide," *Fibers,* vol. 5, p. 23, 2017.

[81] G. Tao, H. Ebendorff-Heidepriem, A. M. Stolyarov, S. Danto, J. V. Badding, Y. Fink, *et al.*, "Infrared fibers," *Advances in Optics and Photonics,* vol. 7, pp. 379-458, 2015.

[82] X. Zhu, G. Zhu, C. Wei, L. V. Kotov, J. Wang, M. Tong, *et al.*, "Pulsed fluoride fiber lasers at 3 um [Invited]," *Journal of the Optical Society of America B,* vol. 34, pp. A15-A28, 2017.

[83] V. Fortin, F. Maes, M. Bernier, S. T. Bah, M. D'Auteuil, and R. Vallée, "Watt-level erbium-doped all-fiber laser at 3.44 μm," *Optics Letters,* vol. 41, pp. 559-562, 2016.

[84] O. Henderson-Sapir, S. D. Jackson, and D. J. Ottaway, "Versatile and widely tunable mid-infrared erbium doped ZBLAN fiber laser," *Optics Letters,* vol. 41, pp. 1676-1679, 2016.

[85] O. Henderson-Sapir, A. Malouf, N. Bawden, J. Munch, S. D. Jackson, and D. J. Ottaway, "Recent Advances in 3.5 um Erbium-Doped Mid-Infrared Fiber Lasers," *IEEE Journal of Selected Topics in Quantum Electronics,* vol. 23, pp. 6-14, 2017.

[86] Y. O. Aydın, V. Fortin, F. Maes, F. Jobin, S. D. Jackson, R. Vallée, *et al.*, "Diode-pumped mid-infrared fiber laser with 50% slope efficiency," *Optica,* vol. 4, pp. 235-238, 2017.

[87] F. Maes, V. Fortin, M. Bernier, and R. Vallée, "5.6 W monolithic fiber laser at 3.55 μm," *Optics Letters,* vol. 42, pp. 2054-2057, 2017.

[88] N. Dadashzadeh, M. P. Thirugnanasambandam, H. W. K. Weerasinghe, B. Debord, M. Chafer, F. Gerome, *et al.*, "Near diffraction-limited performance of an OPA pumped acetylene-filled hollow-core fiber laser in the mid-IR," *Optics Express,* vol. 25, pp. 13351-13358, 2017.

[89] P. Gupta and S. Mehendale, "Mid-infrared optically pumped molecular lasers," *Hyperfine Interactions,* vol. 37, pp. 243-273, 1987.

[90] A. Javan, W. R. Bennett, and D. R. Herriott, "Population Inversion and Continuous Optical Maser Oscillation in a Gas Discharge Containing a He-Ne Mixture," *Physical Review Letters,* vol. 6, pp. 106-110, 1961.

[91] T. Y. Chang and T. J. Bridges, "Laser action at 452, 496, and 541 μm in optically pumped CH_3F," *Optics Communications,* vol. 1, pp. 423-426, 1970.

[92] T. Y. Chang and O. R. Wood, "Optically pumped atmospheric - pressure CO_2 laser," *Applied Physics Letters,* vol. 21, pp. 19-21, 1972.

[93] H. R. Schlossberg and H. R. Fetterman, "Optically pumped vibrational transition laser in OCS," *Applied Physics Letters,* vol. 26, pp. 316-318, 1975.

[94] J. E. McCord, H. C. Miller, G. Hager, A. I. Lampson, and P. G. Crowell, "Experimental investigation of an optically pumped mid-infrared carbon monoxide laser," *IEEE Journal of Quantum Electronics,* vol. 35, pp. 1602-1612, 1999.

[95] J. E. McCord, A. A. Ionin, S. P. Phipps, P. G. Crowell, A. I. Lampson, J. K. McIver, *et al.*, "Frequency-tunable optically pumped carbon monoxide laser," *IEEE Journal of Quantum Electronics,* vol. 36, pp. 1041-1052, 2000.

[96] H. C. Miller, D. T. Radzykewycz, and G. Hager, "An optically pumped mid-infrared HBr laser," *IEEE Journal of Quantum Electronics,* vol. 30, pp. 2395-2400, 1994.

[97] R. Amarin, "Theoretical and experimental studies of optically pumped molecular gas lasers," Doctoral Dissertation, Optical Science and Engineering, 2010.

[98] R. C. Jones, "Review of laser-pumped molecular lasers," in *Gas Flow and Chemical Lasers: Tenth International Symposium,* pp. 460-468, 1995.

[99] D. C. Brown, "Diode-pumped gas lasers," ed: Google Patents, 2001.

[100] C. Kletecka, N. Campbell, C. Jones, J. Nicholson, and W. Rudolph, "Cascade lasing of molecular HBr in the four micron region pumped by a Nd: YAG laser," *IEEE Journal of Quantum Electronics,* vol. 40, pp. 1471-1477, 2004.

[101] W. Koen, C. Jacobs, C. Bollig, H. J. Strauss, M. J. Daniel Esser, and L. R. Botha, "Optically pumped tunable HBr laser in the mid-infrared region," *Optics Letters,* vol. 39, pp. 3563-3566, 2014.

[102] R. J. Beach, W. F. Krupke, V. K. Kanz, S. A. Payne, M. A. Dubinskii, and L. D. Merkle, "End-pumped continuous-wave alkali vapor lasers: experiment, model, and power scaling," *Journal of the Optical Society of America B,* vol. 21, pp. 2151-2163, 2004.

[103] W. F. Krupke, R. J. Beach, V. K. Kanz, and S. A. Payne, "DPAL: A new class of CW, near-infrared high-power diodepumped alkali (vapor) lasers," in *Proc. of SPIE*, pp. 157-167, 2004.

[104] R. Knize and B. Zhdanov, "Alkali Vapor Lasers," in *Laser Science*, p. LTuA1, 2008.

[105] W. F. Krupke, R. J. Beach, V. K. Kanz, and S. A. Payne, "Resonance transition 795-nm rubidium laser," *Optics Letters,* vol. 28, pp. 2336-2338, 2003.

[106] B. Zhdanov, T. Ehrenreich, and R. Knize, "Highly efficient optically pumped cesium vapor laser," *Optics Communications,* vol. 260, pp. 696-698, 2006.

[107] B. Zhdanov, J. Sell, and R. Knize, "Multiple laser diode array pumped Cs laser with 48W output power," *Electronics Letters,* vol. 44, pp. 582-583, 2008.

[108] W. T. Silfvast, *Laser fundamentals*. Cambridge university press, 2004.

[109] R. L. Brooks, *The fundamentals of atomic and molecular physics*. Springer, 2013.

[110] W. Demtröder, *Atoms, Molecules, and Photons*. Springer, 2006.

[111] W. C. Swann and S. L. Gilbert, "Pressure-induced shift and broadening of 1510–1540-nm acetylene wavelength calibration lines," *JOSA B,* vol. 17, pp. 1263-1270, 2000.

[112] H. Sasada and K. Yamada, "Calibration lines of HCN in the 1.5-μm region," *Applied Optics,* vol. 29, pp. 3535-3547, 1990.

[113] J. A. Stregack, B. L. Wexler, and G. A. Hart, "cw CO - CS_2, CO - C_2H_2, and CO - N_2O energy - transfer lasers," *Applied Physics Letters,* vol. 28, pp. 137-139, 1976.

[114] H. Kildal and T. F. Deutsch, "Optically pumped infrared V - V transfer lasers," *Applied Physics Letters,* vol. 27, pp. 500-502, 1975.

[115] A. M. Jones, A. V. Nampoothiri, A. Ratanavis, R. Kadel, N. V. Wheeler, F. Couny, *et al.*, "C_2H_2 gas laser inside hollow-core photonic crystal fiber based on population inversion," in *Conference on Lasers and Electro-Optics*, p. CTuU1, 2010.

[116] K. Nakagawa, M. de Labachelerie, Y. Awaji, and M. Kourogi, "Accurate optical frequency atlas of the 1.5-μm bands of acetylene," *Journal of the Optical Society of America B,* vol. 13, pp. 2708-2714, 1996.

[117] L. S. Rothman, I. E. Gordon, Y. Babikov, A. Barbe, D. Chris Benner, P. F. Bernath, *et al.*, "The HITRAN2012 molecular spectroscopic database," *Journal of Quantitative Spectroscopy and Radiative Transfer,* vol. 130, pp. 4-50, 2013.

[118] J. D. Tobiason, M. D. Fritz, and F. F. Crim, "State‐to‐state relaxation of highly vibrationally excited acetylene by argon," *The Journal of Chemical Physics,* vol. 101, pp. 9642-9647, 1994.

[119] I. W. M. Smith and J. F. Warr, "Vibrational relaxation of $C_2H_2(v_3,v_2+v_4+v_5)$ in self-collisions and in collisions with the noble gases," *Chemical Physics Letters,* vol. 173, pp. 70-75, 1990.

[120] N. M. Litchinitser, A. K. Abeeluck, C. Headley, and B. J. Eggleton, "Antiresonant reflecting photonic crystal optical waveguides," *Optics Letters,* vol. 27, pp. 1592-1594, 2002.

[121] M. Duguay, Y. Kokubun, T. L. Koch, and L. Pfeiffer, "Antiresonant reflecting optical waveguides in SiO_2‐Si multilayer structures," *Applied Physics Letters,* vol. 49, pp. 13-15, 1986.

[122] N. M. Litchinitser, S. C. Dunn, B. Usner, B. J. Eggleton, T. P. White, R. C. McPhedran, *et al.*, "Resonances in microstructured optical waveguides," *Optics Express,* vol. 11, pp. 1243-1251, 2003.

[123] K. Saitoh, N. Mortensen, and M. Koshiba, "Air-core photonic band-gap fibers: the impact of surface modes," *Optics Express,* vol. 12, pp. 394-400, 2004.

[124] J. Hu and C. R. Menyuk, "Understanding leaky modes: slab waveguide revisited," *Advances in Optics and Photonics,* vol. 1, pp. 58-106, 2009.

[125] B. Debord, M. Alharbi, T. Bradley, C. Fourcade-Dutin, Y. Wang, L. Vincetti, *et al.*, "Hypocycloid-shaped hollow-core photonic crystal fiber Part I: Arc curvature effect on confinement loss," *Optics Express,* vol. 21, pp. 28597-28608, 2013.

[126] S. Poole, D. N. Payne, and M. E. Fermann, "Fabrication of low-loss optical fibres containing rare-earth ions," *Electronics Letters,* vol. 21, pp. 737-738, 1985.

[127] O. Humbach, H. Fabian, U. Grzesik, U. Haken, and W. Heitmann, "Analysis of OH absorption bands in synthetic silica," *Journal of Non-crystalline Solids,* vol. 203, pp. 19-26, 1996.

[128] L. S. Rothman, I. E. Gordon, A. Barbe, D. C. Benner, P. F. Bernath, M. Birk, *et al.*, "The HITRAN 2008 molecular spectroscopic database," *Journal of Quantitative Spectroscopy and Radiative Transfer,* vol. 110, pp. 533-572, 2009.

[129] L. Rothman, R. Hawkins, R. Wattson, and R. Gamache, "Energy levels, intensities, and linewidths of atmospheric carbon dioxide bands," *Journal of Quantitative Spectroscopy and Radiative Transfer,* vol. 48, pp. 537-566, 1992.

[130] R. Brüning, P. Gelszinnis, C. Schulze, D. Flamm, and M. Duparré, "Comparative analysis of numerical methods for the mode analysis of laser beams," *Applied Optics,* vol. 52, pp. 7769-7777, 2013.

[131] T. Kaiser, D. Flamm, S. Schröter, and M. Duparré, "Complete modal decomposition for optical fibers using CGH-based correlation filters," *Optics Express,* vol. 17, pp. 9347-9356, 2009.

[132] D. Flamm, D. Naidoo, C. Schulze, A. Forbes, and M. Duparré, "Mode analysis with a spatial light modulator as a correlation filter," *Optics Letters,* vol. 37, pp. 2478-2480, 2012.

[133] J. R. Fienup, "Phase retrieval algorithms: a comparison," *Applied Optics,* vol. 21, pp. 2758-2769, 1982.

[134] R. W. Gerchberg, "A practical algorithm for the determination of the phase from image and diffraction plane pictures," *Optik,* vol. 35, pp. 237-246, 1972.

[135] O. Shapira, A. F. Abouraddy, J. D. Joannopoulos, and Y. Fink, "Complete Modal Decomposition for Optical Waveguides," *Physical Review Letters,* vol. 94, p. 143902, 2005.

[136] H. Lü, P. Zhou, X. Wang, and Z. Jiang, "Fast and accurate modal decomposition of multimode fiber based on stochastic parallel gradient descent algorithm," *Applied Optics,* vol. 52, pp. 2905-2908, 2013.

[137] L. Huang, S. Guo, J. Leng, H. Lü, and P. Zhou, "Real-time mode decomposition for few-mode fiber based on numerical method," *Optics Express,* vol. 23, pp. 4620-4629, 2015.

[138] N. Andermahr, T. Theeg, and C. Fallnich, "Novel approach for polarization-sensitive measurements of transverse modes in few-mode optical fibers," *Applied Physics B: Lasers and Optics,* vol. 91, pp. 353-357, 2008.

[139] D. Schimpf, R. Barankov, and S. Ramachandran, "Cross-correlated (C^2) imaging of fiber and waveguide modes," *Optics Express,* vol. 19, pp. 13008-13019, 2011.

[140] J. W. Nicholson, A. D. Yablon, J. M. Fini, and M. D. Mermelstein, "Measuring the modal content of large-mode-area fibers," *IEEE Journal of Selected Topics in Quantum Electronics,* vol. 15, pp. 61-70, 2009.

[141] D. Gray, S. Sandoghchi, N. Wheeler, N. Baddela, G. Jasion, M. Petrovich, *et al.*, "Accurate calibration of S^2 and interferometry based multimode fiber characterization techniques," *Optics Express,* vol. 23, pp. 10540-10552, 2015.

[142] J. M. Fini, "Aircore microstructure fibers with suppressed higher-order modes," *Optics Express,* vol. 14, pp. 11354-11361, 2006.

[143] J. R. Hayes, S. R. Sandoghchi, T. D. Bradley, Z. Liu, R. Slavík, M. A. Gouveia, *et al.*, "Antiresonant hollow core fiber with an octave spanning bandwidth for short haul data communications," *Journal of Lightwave Technology*, vol. 35, pp. 437-442, 2017.

[144] V. Nampoothiri, A. M. Jones, A. Ratanavis, R. Kadel, N. Wheeler, F. Couny, *et al.*, "Mid-IR laser emission from a C2H2 gas filled hollow core photonic crystal fiber," in *Proceedings of SPIE - The International Society for Optical Engineering*, pp. xxxiii-xxxiv, 2010.

[145] A. M. Jones, A. V. V. Nampoothiri, A. Ratanavis, T. Fiedler, N. V. Wheeler, F. Couny, *et al.*, "Mid-infrared gas filled photonic crystal fiber laser based on population inversion," *Optics Express*, vol. 19, pp. 2309-2316, 2011.

[146] M. R. A. Hassan, "Synchronously Pumped and Continuous Wave Mid-IR Hollow Core Fibre Gas Lasers," degree of Doctor of Philosophy, Department of Physics, University of Bath, 2016.

[147] I. Dicaire, J.-C. Beugnot, and L. Thévenaz, "Analytical modeling of the gas-filling dynamics in photonic crystal fibers," *Applied Optics*, vol. 49, pp. 4604-4609, 2010.

[148] M. Xu, F. Yu, and J. Knight, "Mid-infrared 1 W hollow-core fiber gas laser source," *Optics Letters*, vol. 42, pp. 4055-4058, 2017.

[149] J. Han, K. Freel, and M. C. Heaven, "Rotational and vibrational energy transfer in vibrationally excited acetylene at energies near 6560 cm−1," *The Journal of Chemical Physics*, vol. 135, p. 244304, 2011.

[150] Z. Wang, Z. Zhou, Z. Li, N. Zhang, and Y. Chen, "Tunable mid-infrared emission from acetylene-filled hollow-core fiber," in *SPIE/COS Photonics Asia*, p. 8, 2016.

Table of tables and figures: